



Friedrich-Schiller-Universität Jena

Physikalisch-Astronomische Fakultät

# **Roughness, wetting, and optical properties of functional surfaces**

Dissertation

zur Erlangung des akademischen Grades  
doctor rerum naturalium (Dr. rer. nat.)



vorgelegt dem Rat der Physikalisch-Astronomischen Fakultät  
der Friedrich-Schiller-Universität Jena

von Dipl.-Ing. Luisa Coriand  
geboren am 22.09.1984 in Jena

## Gutachter

1. Prof. Dr. rer. nat. Andreas Tünnermann (FSU Jena)
2. Prof. Dr. rer. nat. Markus Rettenmayr (FSU Jena)
3. Prof. Flávio Horowitz PhD (UFRGS Porto Alegre)

Tag der Disputation: 13.06.2013

# Contents

1	Introduction .....	1
2	Basics .....	4
	2.1 Roughness.....	4
	2.2 Wetting.....	6
	2.3 Light scattering .....	9
	2.4 Porosity .....	11
3	Characterization techniques .....	14
	3.1 AFM, WLI, LSM, and their combination .....	14
	3.2 Contact angle measurement and contour analysis.....	19
	3.3 Light scattering technique .....	21
	3.4 Spectrophotometry and data analysis .....	22
4	Relationships between the structural and wetting properties.....	25
	4.1 Roughness and hydrophobicity .....	25
	4.1.1 Classical concepts .....	25
	4.1.2 The $\kappa$ B approach.....	27
	4.2 Roughness / porosity and hydrophilicity .....	31
5	Samples .....	33
	5.1 Nanorough optical coatings .....	33
	5.2 Microrough engineering surfaces .....	36
	5.3 Hydrophobic functionalization .....	37
	5.4 List of samples .....	38
6	Advanced wetting analysis.....	40
	6.1 Hydrophobic surfaces .....	40
	6.1.1 Superhydrophobicity: Common definitions .....	40
	6.1.2 Comprehensive wetting analysis methods .....	41
	6.1.3 Novel criteria for superhydrophobicity .....	45
	6.2 Hydrophilic surfaces .....	47
	6.2.1 Anti-fog: Common definitions.....	48
	6.2.2 Comprehensive wetting analysis methods .....	48
	6.2.3 Novel criteria for anti-fog surfaces .....	52
	6.3 Summary .....	52

7	Results and discussion .....	54
7.1	Validation of the methodology for superhydrophobicity .....	55
7.2	Hydrophobic and superhydrophobic nanorough optical coatings .....	59
7.2.1	Roughness and wetting properties .....	59
7.2.2	Effect of hydrophobic functionalization on wettability .....	69
7.2.3	Optical properties and stability .....	73
7.2.4	Summary .....	77
7.3	Hydrophilic nanorough optical coatings .....	78
7.3.1	Structural properties and hydrophilicity .....	79
7.3.2	Optical properties .....	89
7.3.3	Summary .....	90
7.4	Hydrophobic and superhydrophobic microstructured surfaces .....	91
8	Conclusions and outlook .....	96
	Bibliography .....	99

# Nomenclature

## *General*

AFM	Atomic Force Microscope
EMA	Effective Medium Approximation (Bruggeman)
IOF	Institute for Applied Optic and Precision Engineering
LSM	Laser Scanning Microscope
SEM	Scanning Electron Microscope
WLI	White Light Interferometer

## *Roughness*

f	spatial frequency
PSD	power spectral density function
rms, $\sigma$	root mean square roughness
$\sigma_{ABC}$	ABC-model parameter (root mean square roughness)
$\tau_{ABC}$	ABC-model parameter (correlation length)

## *Wetting*

$\alpha$	tilt base angle
$\alpha_{bo}$	bounce-off angle
CA	contact angle
$\gamma_s, \gamma_l, \gamma_{sl}$	solid and liquid surface tension, solid-liquid interfacial tension
$\theta_{ac}, \theta_{ap}$	actual and apparent contact angle
$\theta_{aca}, \theta_{rca}$	advancing and receding contact angle
$\theta_{CB}$	Cassie-Baxter contact angle
$\theta_W$	Wenzel contact angle
$\theta_Y$	Young contact angle
$\theta_0$	$\theta_{ap}$ at a wetting time of 0 s
$\theta_{mean}$	averaged $\theta_{ap}$ between a wetting time of 10 s and 20 s
$\kappa_B$	wetting parameter
$K, m$	fit parameters of the Tanner law
$N_{drops}$	number of visible fogging droplets in the field of view of 1.7x1.4 mm <sup>2</sup> after 10 s
$r$	roughness ratio
$r_f, f_s$	roughness ratio of wetted area, fraction of projected surface area
$R_W$	Wenzel roughness function
SH	superhydrophobic according to strict theoretical criteria
SH <sub>pr</sub>	superhydrophobic according to practical aspects

$t_{\text{fog}}$	fogging time at which the fog has been completely dissolved in the field of view of $1.7 \times 1.4 \text{ mm}^2$
$t_w$	wetting time

### *Optical*

ARS	angle resolved scattering
d	layer thickness
$\varepsilon$	dielectric function
F	porosity
$\theta_s$	scattering angle
$\lambda$	wavelength
n	real refractive index
TS	total scattering
T, R, A, S	transmittance, reflectance, absorbance, scattering

### *Sample preparation*

$c_{\text{particle}}$	particle concentration
$d_{\text{particle}}$	particle diameter
$N_{\text{dip}}$	number of dipping iteration
PVD	physical vapor deposition
PolyF1	hydrophobic top layer (fluoroalkylsilane)
$v_{\text{draw}}$	withdrawal velocity
WR4 <sup>®</sup>	hydrophobic top layer (fluoroalkylsilane)

# 1 Introduction

Functional surfaces with specific wetting properties play a key role in simplifying various processes in daily life and using resources efficiently. For instance, windows, mirrors, and optical components made of surfaces with adjustable hydrophobic wetting behavior all the way to superhydrophobicity and self-cleaning can minimize the utilization of chemicals and thus reduce the environmental pollution. The anti-fog effect basing on hydrophilic wettability can considerably improve the quality of different optical surfaces, e.g. lenses, helmet visors, and bathroom mirrors. At the beginning, the technical fabrication of such functional properties is often inspired by nature, as for the realization of the self-cleaning effect of the lotus leaf. However, to achieve such excellent wetting, thorough enlightenment of the structural, wetting, and optical properties is required. This thesis is therefore focused on the development of a complex methodology for a comprehensive characterization of hydrophobic and hydrophilic wetting systems.

Wetting properties have been studied for a long time. The correlation between contact angles and surface and interfacial tensions was already reported in 1805 [1]. The fact that the wettability is influenced not only by the intrinsic chemical properties but also by the surface roughness is also well-known [2-4]. These fundamental relationships are still the basis of current theoretical studies which deal with the thermodynamic wetting aspects or simulate the influence of deterministic surface roughness, e.g. [5-7]. Besides these considerations, the majority of the recently published investigations of wetting are concerned with rather empirical approaches to fabricate superhydrophobic surfaces utilizing different manufacturing processes, structural, and intrinsic material properties [8-10]. For hydrophilic wettability aiming at anti-fogging, the number of publications is considerably smaller and most of these works report on photocatalytic coatings (e.g. titanium oxide) [11-13], which are not suitable for indoor applications, and on complex multilayer systems [14-16].

In spite of the tremendous interest and extensive research activities regarding wettability of functional surfaces, no uniform and coherent theoretical descriptions are given. Rather, considerable disagreements, unsolved problems, and even wrong conclusions exist. For both superhydrophobicity and anti-fog, no generally accepted terms nor definitions can yet be found in the literature as discussed in detail in [17]. Especially for superhydrophobicity, the statements are often contradictory and, in most cases, only the simplest definition (contact angle  $> 150^\circ$ ) is being used (e.g. [9, 18]). This problem is increased through the fact that there are no uniform measurement and analysis methods for roughness and wetting characterization. Roughness analysis is usually performed by means of qualitative assessments or simple roughness parameters. For the wetting analysis, various kinds of contact



angle measurement methods with different measurement parameters or contour analysis procedures are applied. Consequently, there is a lack in systematical studies and understanding of the functional properties and their relationships as well as a gap between theoretical studies and practical approaches: Papers address either pure theoretical examinations or technological aspects of surface structuring and chemistry. Experimental trial-and-error approaches are normally employed to achieve the desired wettability. For example, investigations of the superhydrophobic lotus leaf often led to the unjustified conclusion that hierarchical roughness structures are necessary for superhydrophobicity [10, 19-21]. Thus, besides specific deterministic roughness structures, hierarchical surface characteristics were fabricated to create excellent wettability [18, 22-24]. Furthermore, optical properties are quite often neglected, even though unacceptable levels of light scattering as a result of surface roughness and porosity required for optimal wettability can cause a failure for envisaged the optical application.

Within the framework of this thesis, the specified limits of the current research activities are taken up as problems: A thorough characterization of the structural, wetting, and optical properties as well as systematic investigations of their corresponding relationships enable the effective realization of superhydrophobic or anti-fog surfaces linked with low light scattering using simple fabrication processes. Consequently, the development of a measurement and analysis methodology consisting of robust methods which are focused on the particular application constitutes the main task of this thesis. With the help of such a methodology, a consistent research, assessment, and definition of hydrophobic and hydrophilic wettability up to superhydrophobicity or anti-fogging of various wetting systems (different structural and intrinsic properties) shall become possible.

The basis for developing this methodology is existing measurement and analysis methods. For the roughness analysis, different measurement systems (Atomic Force Microscope, White Light Interferometer, Laser Scanning Microscope) as well as analysis tools are available. The most important quantities are the power spectral density function [25] and a roughness based structural parameter (wetting parameter  $\kappa_B$ ). The latter was developed in previous works and is directly connected to the contact angle of the wetting system [26, 27]. For the characterization of wettability, advancing and receding contact angle measurements in combination with tilt base angle measurements are the starting point. Initially, to be examined is to what extent all these methods can be transferred and improved with respect to specific or new wetting situations. The necessity to develop novel methods has to be taken into consideration as well. In particular, the investigation of the following main aspects will be pursued: The possibility to extend the  $\kappa_B$  approach to hydrophobic microrough and hydrophilic nanorough surfaces as well as the range of validity of the threshold,

which so far has been set to 0.3 [28], have to be studied. It is necessary to examine the applicability of the existing contact angle measurement and analysis methods established for hydrophobicity to hydrophilic surfaces. Simultaneously, the introduction of novel wetting experiments with respect to practical applications has to be investigated. For instance, the achievement of a first method to quantify the anti-fog behavior is required. After the development of the wetting analysis methods, a definition of robust criteria for superhydrophobicity and anti-fog effect is indispensable. The suitability of the acquired methodology has to be proven using different nano- and microrough surfaces. Therefore, the specific roughness characteristics of sol-gel coatings, sputtered coatings, and machined surfaces shall be defined. The methodology applied to these samples can then be utilized to investigate the relationships between structural, wetting, and optical properties and finally to achieve superhydrophobic or anti-fog surfaces.

The thesis is structured as follows:

The basics and working principles of the measurement techniques needed for this work are introduced in chapters 2 and 3. These comprise the roughness analysis using Atomic Force Microscopy, White Light Interferometry, and Laser Scanning Microscopy. Also included is the wetting analysis using a contact angle measurement and contour analysis instrument, determination of scatter losses by the angle resolved light scattering technique, and spectrophotometry for determining the porosity and layer thickness.

In chapter 4, classical relationships between structural properties and wetting are presented. However, this chapter primarily covers the introduction and discussion of the  $\kappa_B$  approach.

The fabrication processes and descriptions of the investigated sample surfaces are summarized in chapter 5.

In chapter 6, common definitions of extreme wetting behavior are initially introduced. The development of the wetting analysis methods for a comprehensive characterization of hydrophobic or hydrophilic wettability is then described in detail. On the basis of these methods, novel wetting criteria for superhydrophobicity and anti-fogging are acquired.

In chapter 7, the entire measurement and analysis methodology is applied to wetting systems with different structural and chemical properties in order to validate the analysis methods as well as to investigate the correlation between the process parameters, structural, wetting, and optical properties.

## 2 Basics

In this chapter, the most important fundamentals of surface and thin film characterization required for the present work are summarized. They are comprised of the utilized roughness and porosity analysis methods as well as theoretical principles to describe the wetting and light scattering behavior. These definitions provide the basis for investigating the correlations between the roughness, wetting, and optical properties.

### 2.1 Roughness

For the analysis of stochastically rough surfaces, several parameters and functions are available. In this work, root mean square (rms) roughness and power spectral density (PSD) function were used to characterize the two-dimensional surface topography data of the investigated nano- and microstructured surfaces. Throughout this work, the roughness structures are assumed to be isotropic, i.e. independent of the direction on the surface. Detailed definitions for the quantities are described in [25, 29-31].

The PSD function provides the relative strength of the individual roughness components as a function of the spatial frequencies  $f_x$  and  $f_y$  in x and y directions, respectively. The PSD is defined as the squared absolute value of the Fourier transform of the surface topography  $h(x, y)$ :

$$\text{PSD}(f_x, f_y) = \lim_{L \rightarrow \infty} \frac{1}{L^2} \left| \int_{-\frac{L}{2}}^{\frac{L}{2}} \int_{-\frac{L}{2}}^{\frac{L}{2}} h(x, y) e^{-2\pi i(f_x x + f_y y)} dx dy \right|^2, \quad (2.1)$$

with the scan range  $L$ .

For surfaces with isotropic roughness characteristics, the  $\text{PSD}(f_x, f_y)$  can be simplified to a 2D-isotropic PSD by transformation into polar coordinates and averaging over all polar angles  $\theta$ . However, in the resulting PSD, the phase information of the roughness structures is no longer considered:

$$\text{PSD}(f) = \frac{1}{2\pi} \int_0^{2\pi} \text{PSD}(f, \theta) d\theta. \quad (2.2)$$

The roughness analysis based on PSD functions includes the vertical as well as the lateral distribution of surface heights. In addition, the PSD enables direct links between the roughness, wetting, and optical properties of a sample. For these and further advantages explained in chapter 4, the PSD function has become indispensable for roughness characterization, not only for this work.

Comprehensive interpretation and discussion of different roughness characteristics based on PSD functions requires more than just a profound theoretical and practical knowledge. For instance, model-PSD functions are needed to approximate the experimentally determined PSDs. By means of the synergy of both the real and the modeled roughness functions measurement artifacts can be identified. Furthermore, model-PSDs are used to simulate a specific design of roughness structures realized by thin films aiming at optimal wetting properties. This type of simulation is utilized in section 7.2.

PSD functions of coated substrates can be modeled by superposition (see Fig. 2.1 on the next page) of a fractal model-PSD representing the pure substrate roughness and an ABC model-PSD illustrating the intrinsic thin film roughness [28, 31, 32]:

$$\text{PSD}_{\text{coating}}(f) = \text{PSD}_{\text{fractal}}(f) + \text{PSD}_{\text{ABC}}(f) , \quad (2.3)$$

where the fractal model-PSD and the ABC model-PSD are defined as [28, 32]:

$$\text{PSD}_{\text{fractal}}(f) = \frac{K}{f^{l+1}} \quad , \quad \text{PSD}_{\text{ABC}}(f) = \frac{A}{(1 + B^2 f^2)^{\frac{C+1}{2}}} . \quad (2.4)$$

$K$ ,  $l$ ,  $A$ ,  $B$ , and  $C$  are parameters of the corresponding model-PSDs (see Fig. 2.1). From the parameters of the ABC-model, vertical ( $\sigma_{\text{ABC}}$ : rms roughness) and lateral ( $\tau_{\text{ABC}}$ : correlation length) information about the roughness structure can be obtained [28, 32]:

$$\sigma_{\text{ABC}} = \sqrt{\frac{2\pi \cdot A}{B^2 \cdot (C - 1)}} \quad , \quad \tau_{\text{ABC}} = \sqrt{\frac{(C - 1)^2 \cdot B^2}{2\pi^2 \cdot C}} . \quad (2.5)$$

Beside the description of the substrate roughness with a fractal model-PSD, the roughness properties can be directly measured. The evaluation of the model-PSDs in combination with the fractal PSD enables an estimation of the intrinsic thin film roughness [33].

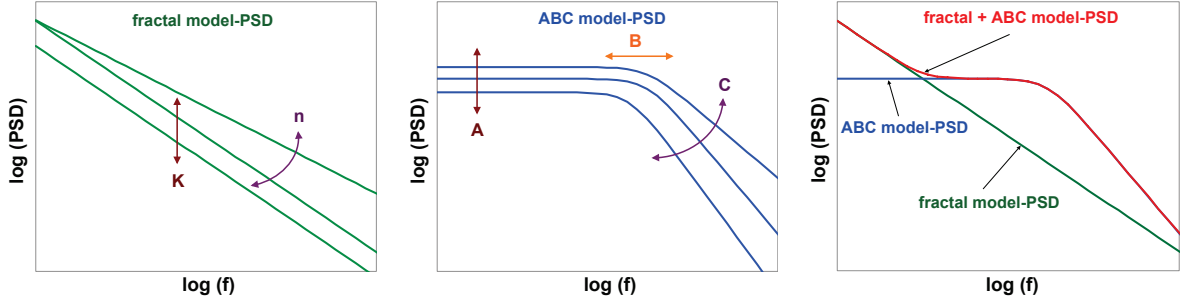


Fig. 2.1: Schematic diagrams of the model-PSDs and their parameters (According to [28]). Left: Fractal model. Center: ABC model. Right: Combination of fractal and ABC model.

Compared to the PSD function, the rms roughness is a simple and common parameter, which only considers the vertical, but not the lateral distribution of roughness structures. The rms roughness  $\sigma$  is the standard deviation of the surface topography data  $h(x, y)$  from the mean value  $\bar{h}$ :

$$\sigma = \left[ \lim_{L \rightarrow \infty} \frac{1}{L^2} \int_{-\frac{L}{2}}^{\frac{L}{2}} \int_{-\frac{L}{2}}^{\frac{L}{2}} (h(x, y) - \bar{h})^2 dx dy \right]^{\frac{1}{2}}. \quad (2.6)$$

The rms roughness can also be calculated by integrating the 2D-isotropic PSD function:

$$\sigma_{2D \text{ PSD}} = \left[ 2\pi \int_{f_{\min}}^{f_{\max}} f \cdot \text{PSD}(f) \cdot df \right]^{\frac{1}{2}}. \quad (2.7)$$

Theoretically, the rms values calculated using Eqs. (2.6) and (2.7) are equal ( $\sigma_{2D \text{ PSD}} \rightarrow \sigma$ ) if the integration limits cover all spatial frequencies ( $f_{\min} \rightarrow 0$  and  $f_{\max} \rightarrow \infty$ ). Practically, every roughness measurement technique is bandwidth-limited, so that the rms roughness and the PSD function depend on the spatial frequency limits. These limits are generally determined by the size of the scan area (lower bandwidth limit) and by the distance between the data points (upper bandwidth limit) of the corresponding measurement system [34].

## 2.2 Wetting

In a system consisting of liquid, solid, and fluid phases, the wetting phenomenon is denoted as the process of a liquid drop spreading on a solid surface surrounded by a fluid (e.g. air) [31]. The main parameter for describing the wetting behavior of

functional surfaces is the contact angle (CA). The CA variation dependent on the ambient conditions is introduced in this section.

For an ideal solid surface (smooth, rigid, chemically homogeneous, insoluble, and nonreactive), the wettability only depends on the surface and interfacial tensions  $\gamma$ . The relationship between the CA and the corresponding tensions is established by the Young theory [1]:

$$\cos \theta_Y = \frac{\gamma_s - \gamma_{sl}}{\gamma_l}, \quad (2.8)$$

with the solid surface tension  $\gamma_s$ , the liquid surface tension  $\gamma_l$ , and the solid-liquid interfacial tension  $\gamma_{sl}$ . The Young CA  $\theta_Y$  is formed between the tangent to the liquid-fluid interface and the surface itself at the contact points between the three phases (see Fig. 2.2 left on the next page).  $\theta_Y$  can also be denoted as ideal CA or intrinsic CA if the drop size is sufficiently large and the effect of line tension is to be negligible [35].

Based on Eq. (2.8), the wettability of ideal solid surfaces by water drops can be classified into two states (see also Fig. 2.2 left and center) with  $\theta_Y = 90^\circ$  as theoretical threshold:

- If  $\gamma_s < \gamma_{sl}$  then  $90^\circ < \theta_Y < 180^\circ$ : intrinsic hydrophobic (water-repelling),
- if  $\gamma_s > \gamma_{sl}$  then  $0^\circ < \theta_Y < 90^\circ$ : intrinsic hydrophilic (water-attracting).

The extreme wetting cases  $\theta_Y = 0^\circ$  and  $\theta_Y = 180^\circ$  will be discussed in chapter 6. For a wetting system with oil or fat as the liquid phase, the prefix of the introduced terms will be “oleo” or “lipo” [36].

Real surfaces are usually chemically heterogeneous and rough. Caused by surface roughness, there are two kinds of CA (Fig. 2.2 right): The actual contact angle  $\theta_{ac}$  is the angle between the tangent to the liquid-fluid interface and the local inclination of the solid surface. In contrast, the apparent contact angle  $\theta_{ap}$  can be directly measured and is defined as the angle between the tangent to the liquid-fluid interface and the line that represents the nominal solid surface as seen macroscopically. In case of an ideal smooth solid surface,  $\theta_{ac} = \theta_{ap}$  is valid [37].

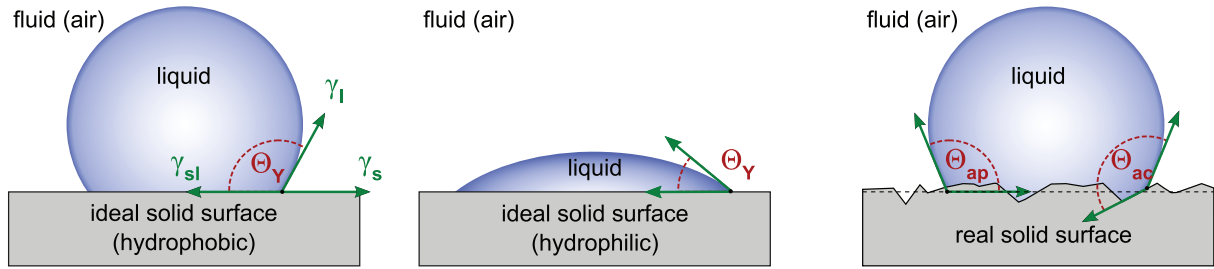


Fig. 2.2: Left: Water drop onto hydrophobic ideal solid surface and corresponding surface/interfacial tensions. Center: Water drop onto hydrophilic ideal solid surface. Right: Actual CA  $\theta_{ac}$  and apparent CA  $\theta_{ap}$  of water drop onto real solid surface.

From a thermodynamic point of view, the Gibbs free energy curve (Fig. 2.3) of a real wetting system as a function of  $\theta_{ap}$  exhibits multiple local energy minima because of roughness and chemical heterogeneities of the solid phase. Therefore, wetting on real solid surfaces is characterized by a wide range of metastable states  $\theta_{ap}$ . This range is called the CA hysteresis with the highest and lowest observed  $\theta_{ap}$  referred to as (theoretical) advancing and receding contact angle,  $\theta_{aca}$  and  $\theta_{rca}$ , respectively [6]:

$$\text{CA hysteresis} = \theta_{aca} - \theta_{rca} . \quad (2.9)$$

The global minimum of the Gibbs free energy curve represents the most stable state of the wetting system. To reach this state corresponding to the most stable CA, the liquid drops have to overcome energy barriers through e.g. external energy [6].

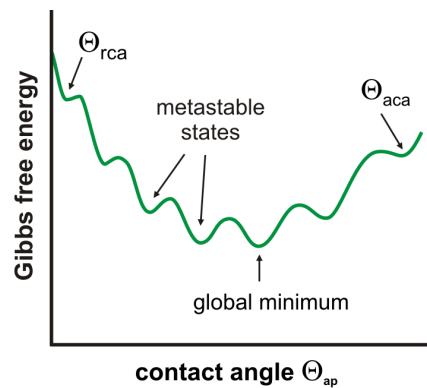


Fig. 2.3: Schematic diagram of Gibbs free energy function of a real solid surface according to [6].

Depending on the liquid drop behavior on a rough solid surface, two classical and well-established wetting regimes can be distinguished. When the liquid completely cover the surface features, the situation is called homogeneous wetting and can be described by the Wenzel equation [2, 38]:

$$\cos\theta_W = r \cdot \cos\theta_Y , \quad (2.10)$$

where the Wenzel CA  $\theta_W$  is equal to  $\theta_{ap}$  and  $r$  is the roughness ratio. The roughness ratio is defined as the real solid surface area related to its projected area. A detailed consideration of Eq. (2.10) leads to the following conclusions concerning the theoretical relationship between the CA and the roughness:

- Ideal smooth surfaces ( $r = 1$ ):  $\theta_W = \theta_Y$ .
- Hydrophobicity ( $\theta_Y > 90^\circ$ ): Increase of  $r$  results in weaker wetting ( $\theta_W > \theta_Y$ ).
- Hydrophilicity ( $\theta_Y < 90^\circ$ ): Increase of  $r$  results in stronger wetting ( $\theta_W < \theta_Y$ ).

Thus, increasing roughness enhances the intrinsic wetting properties in both directions.

In case of the heterogeneous wetting state, air cavities are situated in the roughness structures below the liquid phase. For this situation, the equation developed by Cassie and Baxter becomes valid [3, 38]:

$$\cos\theta_{CB} = f_s \cdot r_f \cdot \cos\theta_Y - (1 - f_s) , \quad (2.11)$$

where  $\theta_{ap}$  is the Cassie-Baxter CA  $\theta_{CB}$ ,  $f_s$  denotes the fraction of the projected surface area that contacts the liquid phase, and  $r_f$  is the roughness ratio of the wetted area. The Cassie-Baxter approximation (2.11) is derived from the Wenzel equation in combination with the Cassie equation, which is used for smooth, but chemically heterogeneous solid surface.

In terms of the validity of the presented equations, it is important to realize wetting systems with a liquid drop size two or three orders of magnitude larger than the lateral dimension of roughness and chemical heterogeneities [39].

## 2.3 Light scattering

A specific surface roughness is required to enhance the intrinsic wetting properties, as described in the previous section. At the same time, increased roughness has a negative effect on the optical properties. Specifically, increased roughness gives rise to light scattering. Thus, a discrepancy between the roughness necessary for optimal wettability and the roughness for acceptable light scattering arises. Therefore, light scattering investigations are required for optical surfaces aiming at special wetting behavior. Otherwise, unacceptable scatter losses caused by the roughness of the functional surfaces can result in an implementation failure for general usage.

In the current section, scattering quantities that are used in this thesis to evaluate the optical brilliance (high transmission and low light scattering) of the investigated



nanorough coatings are introduced. For the sake of simplicity, stochastically rough structures and two-dimensional isotropic surfaces are assumed.

When illuminating a surface, certain parts of the incident light are partially reflected, transmitted, absorbed, and scattered, depending on the material properties. For example, as a result of surface irregularities such as nanoroughness or defects, part of the light is removed from the specular direction and redistributed into diffuse scattering [30, 40]. The underlying geometry and parameters for describing surface and interface scattering are shown in Fig. 2.4.

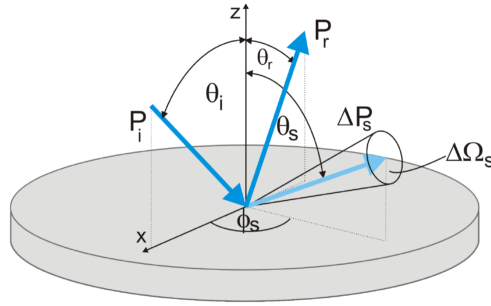


Fig. 2.4: Schematic illustration of reflective scattering geometry and nomenclature:  $z$  ... surface normal,  $P_i$  ... incident power,  $\theta_i$  ... incident angle,  $P_r$  ... specular reflected power,  $\theta_r$  ... reflection angle,  $\Delta P_s$  ... scattered power,  $\Delta \Omega_s$  ... solid angle,  $\theta_s$  ... polar scatter angle, and  $\varphi_s$  ... azimuthal scatter angle [41].

Angle resolved scattering (ARS) is defined as the power  $\Delta P_s$  scattered into a small solid angle  $\Delta \Omega_s$  normalized to that solid angle and the incident power  $P_i$ .  $\theta_s$  is the scattering polar angle with respect to the surface normal. For optical surfaces with an interface roughness much smaller than the wavelength  $\lambda$  of light, vector scattering theory predicts the ARS to be proportional to the surface PSD [42-46]:

$$\text{ARS}(\theta_s) = \frac{1}{P_i} \cdot \frac{\Delta P_s}{\Delta \Omega_s} = Q \cdot \text{PSD}(f). \quad (2.12)$$

$Q$  is the optical factor depending on scattering geometry and optical properties of perfectly smooth surface. The second part of Eq. (2.12) indicates a proportional relationship between roughness (i.e. PSD) and light scattering (i.e. ARS). This illustrates the discrepancy mentioned above: In this thesis, the desired wettability of optical surfaces is created by nanorough coatings, however their thin film roughness leads to increased light scattering.

The scattering of thin film coatings is much more complicated than the relationship in Eq. (2.12) because the scattering of each interface. The total scattered light is not only the amount of scattering intensity resulting from single interfaces. Also the cross-correlation properties between individual interfaces have to be taken into account. The scattering of multilayer coatings is discussed in detail in [42, 43, 47].

The scatter loss of optical components can be described by the total scattering (TS) which is the power  $P_s$  scattered into the forward or backward hemispheres divided by the incident power  $P_i$ . TS can thus be calculated by integration of Eq. (2.12) over the desired hemisphere [44, 46]:

$$TS = \frac{P_s}{P_i} = 2\pi \int_{2^\circ}^{85^\circ} ARS(\theta_s) \cdot \sin\theta_s \cdot d\theta_s , \quad (2.13)$$

The range of acceptance angles is defined by the ISO standard 13696 [48]. This means, for incident light normal to the surface  $\theta_i = 0^\circ$ , an angular range of  $0^\circ \leq \varphi_s \leq 360^\circ$  and  $2^\circ \leq \theta_s \leq 85^\circ$  has to be acquired.

## 2.4 Porosity

The wettability of a surface is influenced by both its intrinsic chemical and its structural properties. In case of hydrophilic wetting, structural properties not only comprise of surface roughness but also porosity [14, 15, 49, 50]. The method presented in [51] was used to determine the porosity and the layer thickness of nanorough and porous coatings in this thesis. The method is based on spectrophotometric measurements combined with subsequent analysis including a simulation of model spectra (see section 3.4). The required fundamentals are summarized in this section.

The power of light illuminating a solid surface can be divided into four parts after interacting with the interface [52, 53]:

- Transmitted part, which passes through the sample,
- part reflected from the surface according to Fresnel law,
- part absorbed by the sample,
- part scattered from the sample into the backward and forward directions.

The ratios of the respective powers to the power of the incident light are denoted as transmittance (T), reflectance (R), absorbance (A), and scattering (S). The energy budget is:

$$1 = T + R + A + S . \quad (2.14)$$

In case of negligible absorption and scattering, Eq. (2.14) can be simplified to  $1 = T + R$ . For normal incidence of light, the transmittance and reflectance of a substrate can be calculated using the Fresnel equations [53]:

$$R_{12}=R_{21} = \left(\frac{n_2 - n_1}{n_2 + n_1}\right)^2, \quad T_{12} = T_{21} = \frac{4n_1n_2}{(n_2 + n_1)^2}, \quad (2.15)$$

with  $n$  representing the real part of the refractive index and the indices indicating medium 1 (e.g. air) and 2 (e.g. glass substrate) (Fig. 2.5). The deviation of  $n_2$  from the index of the corresponding pure bulk material contains information about porosity.

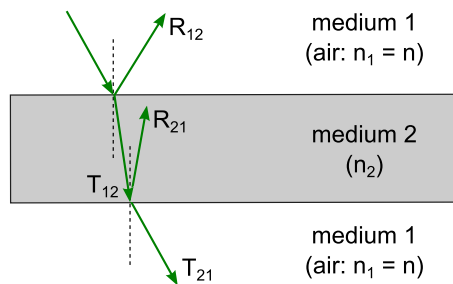


Fig. 2.5: Schematic illustration of reflectance and transmittance.

For spectrophotometric measurements (i.e. transmittance and reflectance spectra) and the modeling presented in section 3.4, the absorbance can be neglected because the investigated samples are highly transparent. The deliberate surface roughness which is essential for optimal hydrophilicity influences the optical properties of the nanorough coatings. Therefore, the thin film roughness has to be taken into consideration for the determination of the porosity. On the one hand, roughness leads to layer thickness variations within the observed scan area which can be described by a Gaussian-shaped distribution. On the other hand, light scattering at the interfaces leads to a reduction of transmittance and reflectance according to the energy budget in Eq. (2.14). An exponential correction factor considering the interface roughness, respectively the scatter losses of the interface, can compensate for this energy loss [51, 54]. For the simulation of the transmittance and reflectance model spectra in section 3.4, the effect of both the film thickness variation as well as the scatter losses was considered for the estimation of porosity.

Furthermore, a model to simplify the samples was needed to determine the porosity of the investigated silicon oxide ( $\text{SiO}_2$ ) coatings from their optical properties. A medium consisting of two components was used for this purpose: Amorphous  $\text{SiO}_2$ , assumed as the host medium, and vacuum filled pores with a specific volume fraction. The optical properties of the whole medium can be assumed to be homogeneous as long as the structural dimensions were much smaller than the wavelength of light. Consequently, the host medium with pores could be considered

as dense and homogeneous with an effective dielectric function  $\epsilon_{\text{eff}}$  which is a function of the dielectric function of both single components (i.e. host and particle) and the volume fraction of the particle. This is called Effective Medium Approximation (EMA). Different theories are available to model the effective dielectric function (of two-component systems) depending on particle diameter and particle distributions. Lorentz-Lorenz, Maxwell Garnett, and Bruggeman's effective medium expressions [53, 55, 56] are the most common theories. As previously reported in [51], the range of validity of the Bruggeman expression was best suited for the characterization of the porous SiO<sub>2</sub> thin film layers investigated in this thesis [55, 57, 58]:

$$0 = F \cdot \frac{\epsilon_p - \epsilon_{\text{eff}}}{\epsilon_p + 2\epsilon_{\text{eff}}} + (1 - F) \cdot \frac{\epsilon_h - \epsilon_{\text{eff}}}{\epsilon_h + 2\epsilon_{\text{eff}}} \quad \text{with } n = \sqrt{\epsilon} \quad . \quad (2.16)$$

$F$  represents the volume fraction of the pores, and the indices h and p indicate host and pores.

It was possible to estimate the porosity of nanorough SiO<sub>2</sub> coatings by means of the EMA used for the simulated model spectra and the spectrophotometric measurement results. This method is presented in section 3.4.

### 3 Characterization techniques

The following sections introduce the measurement and analysis principles of the characterization techniques used in this thesis. First, different profilometers are described for the characterization of surface structures in the spatial frequency range relevant for the wetting properties. With regard to the wetting behavior, the functional principles of the contact angle measurement and contour analysis are presented. The advanced wetting analysis methods adapted to the specific wetting situation will be explained in chapter 6. Furthermore, a typical light scattering measurement system is presented which can be used to determine the scatter loss of optical samples. Finally, porosity and film thickness of thin films were analyzed using a spectrophotometer and a suitable analysis method.

#### 3.1 AFM, WLI, LSM, and their combination

The analysis of the roughness components within a wide spatial frequency range was one of the key aspects for the correlation investigation of this thesis. Three different roughness measurement techniques (Fig. 3.1) were combined to realize the analysis over a wide spatial frequency range from  $0.001 \mu\text{m}^{-1}$  to  $1000 \mu\text{m}^{-1}$ . All systems will be briefly introduced. The algorithm for the combination of the single measurement results is presented as well.

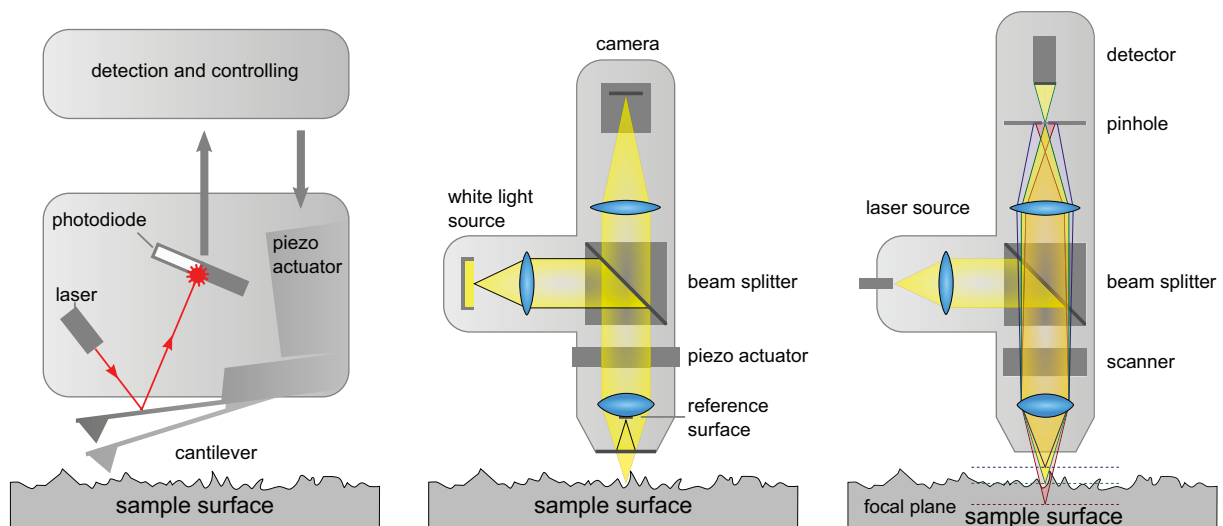


Fig. 3.1: Schematic illustration of Atomic Force Microscope (left), White Light Interferometer (center), and confocal Laser Scanning Microscope (right).

#### *Atomic Force Microscope*

The Atomic Force Microscope (AFM) belongs to the family of Scanning Probe Microscopy. A sharp probe scans the sample surface line-by-line and the probe-sample interaction leads to a deflection of the cantilever. A laser beam which is

reflected from the backside of the cantilever is detected by a split photodiode to determine the deflection. This deflection signal can then be converted to a two-dimensional topography image [31, 59-61].

A Dimension 3100 AFM (manufacturer: Digital Instruments Veeco Metrology Group) was used to analyze the high spatial frequency roughness ranging between  $f = 1 \mu\text{m}^{-1}$  and  $f = 1000 \mu\text{m}^{-1}$  (corresponding scan areas:  $10 \times 10 \mu\text{m}^2$ ,  $1 \times 1 \mu\text{m}^2$ ,  $0.5 \times 0.5 \mu\text{m}^2$ , and  $0.2 \times 0.2 \mu\text{m}^2$ ). The AFM measurements were performed with single crystalline silicon probes (nominal tip radius: 10 nm).

The TappingMode™ was always used for the roughness characterization of nano- and microrough surfaces, because of its high resolution (see following remarks), minor contact forces and absence of shear forces [62]. In this mode, the cantilever mechanically oscillates at or near its resonance frequency. The piezo actuator based scanner records the vertical position in order to maintain a constant oscillation amplitude [61, 62].

Measurement artifacts and noise influence the measurement results. The modification (distortion) of the surface profile by the non-vanishing size of the probe tip can be significant at high spatial frequencies ( $10 \mu\text{m}^{-1} \leq f \leq 1000 \mu\text{m}^{-1}$ ). Thus, the lateral resolution is especially important for the analysis of the wetting-relevant nanorough structures. The limits of reliable roughness information in this critical range were studied in previous works [63, 64]. Based on these results, the influence of the tip for investigations of nanorough optical surfaces was minimized to an optimum. In addition, the measurement parameters, e.g. the free amplitude of the tip oscillation, were adapted to resolve the specific roughness characteristics. Thus, an improved topography resolution could be observed especially in a spatial frequency range higher than  $10 \mu\text{m}^{-1}$ . The vertical resolution is limited by instrumental noise to  $\sigma \approx 0.04 \text{ nm}$ . The maximal vertical measurements range ( $< 5 \mu\text{m}$ ) restricts the analysis of microrough engineering surfaces, which will be discussed in section 7.4.

Drift, vibrations, or static charge can effect the interaction between sample surface and probe as much as the main influencing factors (tip shape and instrumental noise) of AFM measurements. These influencing factors need to be minimized to achieve most authentic roughness information. Furthermore, topography data has to be corrected for offset and tilt by removing a polynomial equation of a certain order. The order depends on the influence of the scanner bow and on the scan area: It is sufficient to remove an equation of first order for scan areas  $\leq 1 \times 1 \mu\text{m}^{-1}$ . Third order polynomials have to be chosen for scan areas  $> 1 \times 1 \mu\text{m}^{-1}$  because of the distinct influence of the scanner bow.

All influencing factors lead to the circumstance that it is not possible to give a general statement for the measurement uncertainty. Within the frame of this work, an upper limit for the uncertainty of the rms roughness should be smaller than approximately 10%.

#### *White Light Interferometer*

The optical profilometer NewView 7300 (manufacturer: Zygo LOT) was used to confirm and extend the roughness analysis performed by AFM measurements in the lower spatial frequency range ( $0.001 \mu\text{m}^{-1} \leq f \leq 1 \mu\text{m}^{-1}$ ). The NewView 7300 is a non-contact, three-dimensional scanning White Light Interferometer (WLI) which is equipped with Michelson and Mirau objectives with magnifications of 5x, 10x, 50x, and 100x.

WLI use broadband light with a short coherence length. Thus, interference only becomes apparent when the optical paths of the reference and the measuring beam are equal. This method requires light to be split inside the objective: one part illuminates the sample surface and the other part the internal high quality reference surface. The objective is driven by a piezoelectrical transducer. During the motion, there are interferograms for all pixels in the field of view. The array of interferograms is recorded by a CCD camera, digitized by a frame grabber and saved by a computer. The acquired data is then processed by frequency-domain analysis which is patented by Zygo Corporation [65, 66]. Finally, the individual height information can be combined to a complete 3D image by MetroPro software [31, 67, 68].

The vertical resolution is smaller than 0.1 nm. The lateral resolution varies between 0.36  $\mu\text{m}$  and 9.5  $\mu\text{m}$  depending on the objective [69]. In general, the topography measurements are influenced by drift, instrumental noise, and vibration. For optical surfaces with  $\sigma < 1$  nm, the quality of the reference surface influences the result significantly. Though, the WLI was only used for the roughness analysis of microrough engineering surfaces with  $\sigma \gg 1$  nm during this work. However, steep edges can lead to measurement errors and missing data points. Therefore, particular care has to be taken when analyzing the results. The NewView 7300 allows to minimize the number of missing data points by adapting the so-called "MinMod" parameter, which sets the minimum intensity for valid data points. This parameter has to be used carefully because choosing the value too small might cause ambient light to be observed as measurement signal. In addition, missing data points can be replaced by interpolation up to a maximum pixel area. Black areas in the topography images illustrate the remaining missing data points after correction. Examples are presented in section 7.4. For the roughness analysis, the tilt between the sample and the x-y-measuring plane is compensated for by a least square fit of the data which removes a plane tilted surface.

The uncertainty of rms roughnesses in this thesis is approximately 20% for the investigated engineering surfaces.

#### *Laser Scanning Microscope*

Another optical measurement system used in this thesis is the confocal Laser Scanning Microscope (LSM) LSM 510 (manufacturer: Carl Zeiss Jena GmbH). Compared to the WLI, the advantage of the LSM is the ability to measure roughness structures with steep slopes. For this reason the LSM was utilized for the characterization of technical rough surfaces with such steep edges. Usually, the WLI fails for such measurement scenarios. For the available objectives (5x, 10x, 50x, 100x) a theoretical spatial frequency range from  $0.0005 \mu\text{m}^{-1}$  to  $4 \mu\text{m}^{-1}$  can be covered. This is similar to the spatial frequency range of the WLI (see Fig. 3.2 on the next page). The aperture of the confocal pinhole and the vertical as well as the lateral resolution is determined by the utilized objectives.

The LSM consists of a scanning unit which scans a focused laser beam line-by-line and layer-by-layer over the sample surface. The reflected light from the surface is detected by a photomultiplier tube. The essential part of the LSM is a pinhole, which is situated in front of the detector. It causes a depth-discrimination of the optical system. The diameter of the pinhole defines the amount of light to be detected from object points outside the focal plane, i.e. the quantity of light which can pass through the pinhole. The reflected light from all other points is prevented from reaching the detector. A defined motion of the sample along the optical axis causes a shift of the focal plane in appropriate steps. Hence, three-dimensional images can be determined with the corresponding analysis software [31, 70, 71].

The influencing factors and the utilized manipulation steps are the same as for the WLI. In addition, a median filter was used to correct the high frequency noise. The estimation of the measurement uncertainty is similar to the WLI: rms roughness < 20%.

#### *Combination of different characterization techniques*

It is essential to know that every roughness measurement technique is bandwidth limited for a correct interpretation and discussion of rms roughnesses and PSD functions determined from topography data (section 2.1). The spatial frequency limits of the systems (see Fig. 3.2) depend on the scan area and the sampling point distance [34]. Nevertheless, the spatial frequency range of interest is defined by the application. Especially, the determination of the wetting-relevant spatial frequency requires to capture a sufficiently large spatial frequency range of the roughness structures. This can be achieved by combining different measurement results (i.e. scan areas or measurement systems).



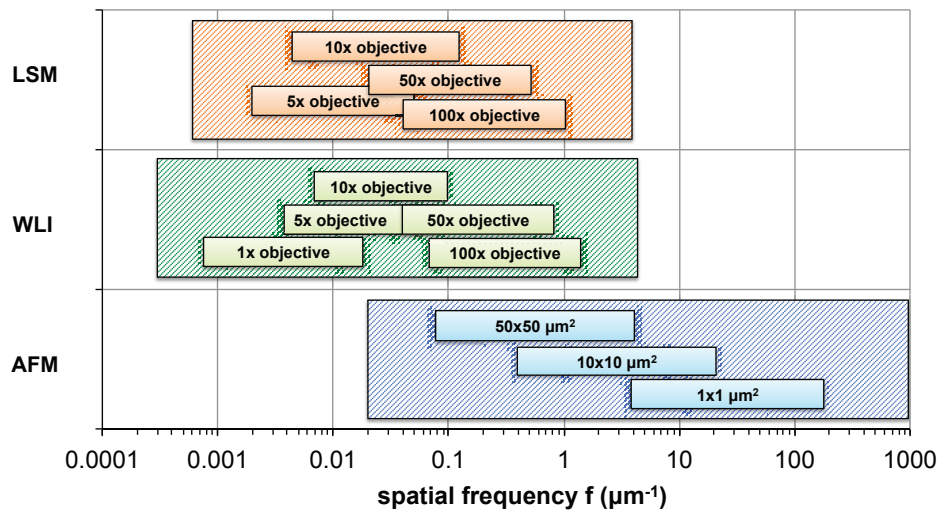


Fig. 3.2: Spatial frequency ranges of different roughness measurement techniques: Atomic Force Microscope (AFM), scanning White Light Interferometer (WLI), and confocal Laser Scanning Microscope (LSM).

The nanorough optical surfaces were examined by AFM in a spatial frequency range between  $1 \mu\text{m}^{-1} \leq f \leq 1000 \mu\text{m}^{-1}$ . Investigations during the “Diplomarbeit thesis” [31] showed that for such nanorough surfaces the wettability is mainly influenced by the high spatial frequency roughness. Thus, a roughness characterization using the WLI or LSM is not sufficient. The characterization of the engineering surfaces and the biological samples was performed with AFM, WLI, and LSM.

The combination of different bandwidth limited PSD functions is crucial for the determination of a characteristic Master-PSD. The Master-PSD is required to calculate the wetting parameter which is introduced in chapter 4. If there is an overlap of the spatial frequency ranges of different measurements and if the PSD values vary just slightly, the individual PSDs can be combined to a Master-PSD by a geometrically averaging. A distortion of the Master-PSD which can be caused by measurement artifacts and surface inhomogeneities can be compensated for by a weighting function or manual manipulation of the single PSDs [25, 72]. An example for single PSD functions which are combined to a unique Master-PSD and typical measurement artifacts are illustrated in Fig. 3.3: The diagram shows that single PSDs can be acceptably combined. Just the high and low spatial frequency range of the single PSDs vary from the Master-PSD because of measurement artifacts.

From now on, Master-PSD will be called simply PSD. All following discussion will be related only to Master-PSDs.

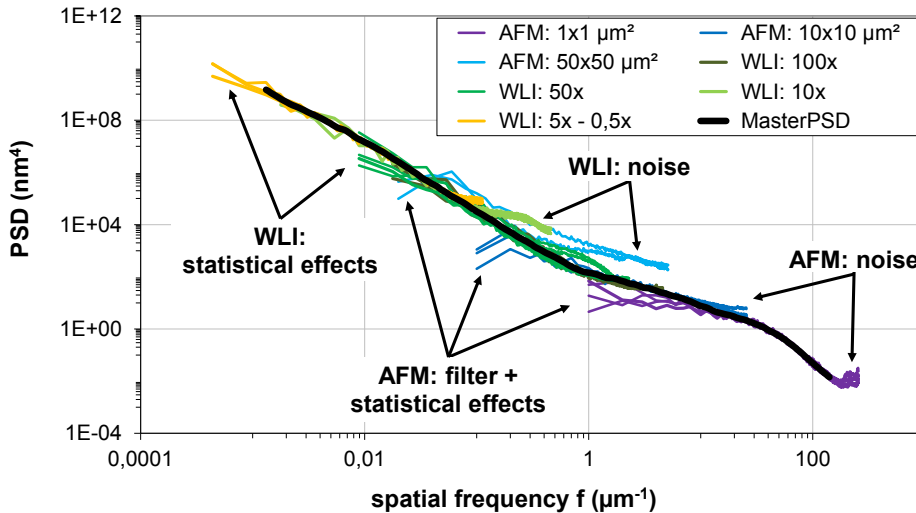


Fig. 3.3: PSD analysis of silicon carbide substrate: Single PSD functions from AFM and WLI topography data, Master-PSD function and typical measurement artifacts.

### 3.2 Contact angle measurement and contour analysis

The applied methods for the characterization of the wettability significantly depend on the wetting system and on the specific application. In addition to this, the wetting theory, summarized in section 2.2, has to be carefully taken into consideration during the entire wetting analysis, i.e. a specification of the wetting behavior through a simple  $\theta_{ap}$  is not sufficient, because of the existence of metastable CA. As published work of Johnson [4] and Marmur [6, 73] suggest, a real rough surface exhibits a wide range of metastable CA (Fig. 2.3). For this reason, a determination of the advancing and receding CA is required to obtain the CA hysteresis, which theoretically covers the whole range of metastable CA.

Within this thesis, methods for a comprehensive wetting analysis were acquired considering all possible wetting configurations, feasible applications, and the theoretical background. The so-called “advanced wetting analysis” will be presented in chapter 6.

In this section, the functional principle of the “contact angle measuring and contour analysis instrument OCA 20” (manufacturer: DataPhysics) (Fig. 3.4), which was used for the investigations, will be presented. Furthermore, some remarks about the performance will be given.



Fig. 3.4: Photograph of the contact angle measurement instrument OCA 20.

The instrument OCA 20 is equipped with an electronic dosing system, a motorized tilting base unit, and a video recording unit.

The standard procedure for determining the CA of liquid drops on solids is the sessile drop method. A drop is deposited onto a solid surface through a needle, which is positioned over the surface. The drop itself is illuminated by diffuse light and a video system face to face with the light source captures the side view of the drop. The contour of the drop is determined by the difference in brightness compared to the background. The analysis software SCA20 (manufacturer: DataPhysics) offers four different methods to calculate the CA [74]: Circle fitting, ellipse fitting, Laplace-Young fitting, and tangent leaning. Further information about the applied calculation methods for sessile drops will be given in chapter 6.

The following aspects turned out to be especially important and were considered during the measurements:

- The drop should be axisymmetric and sufficiently large compared to the roughness scale [38].
- The surface under the liquid drop needs to be dry (no previous wetting with the test liquid) and contamination and defect free.
- Vibrations during the measurement have to be avoided as much as possible.
- The influence of the dosage needle on the drop shape can be minimized by a special hydrophobic coating.
- The most critical factor is the contrast between the drop, sample surface, and background [75]. The illumination conditions have to be adapted according to the wetting system to achieve an optimal contrast. The contrast is mainly affected by the nature of the sample and can result in an under- or overestimation of the determined CA. For example, the automated detection of the CA of a drop on a slightly curved plant surface can be lead to a CA approximately  $10^\circ$  smaller (Fig. 3.5 center) compared to manual drop shape analysis (Fig. 3.5 right).

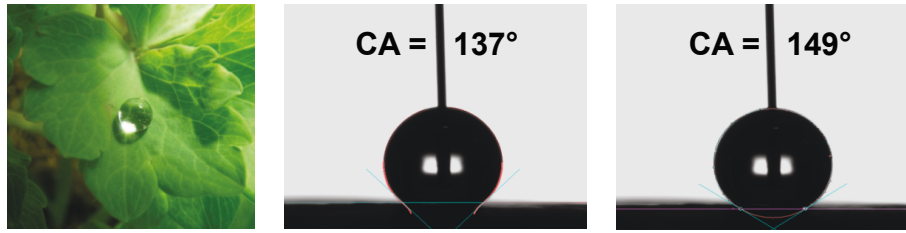


Fig. 3.5: Wetting of a superhydrophobic aquilegia leaf: Photograph with a water drop (left). Automated drop shape analysis based on tangent leaning (center). Manual drop shape analysis (right).

The measurement accuracy of the contact angle measurements system amounts to  $\pm 0.1^\circ$  according to the manufacturer's specifications [74].

### 3.3 Light scattering technique

In addition to the roughness and wetting analysis, the characterization of the light scattering behavior of the optical coatings on glass was necessary. The surface roughness which is needed for special wettability directly influences the scattering properties as introduced in section 2.3.

The light scattering was measured using an angle resolved scattering system to identify possible disturbing factors in a large angular range and to compare the observed scatter losses with a threshold acquired in a previous work [72]. The light scattering measurements within this thesis were performed at a wavelength of 532 nm [76]. This wavelength is located near the maximum sensitivity of the human eye and near the wavelength for which the threshold of scatter losses was determined [72]. For the investigation the measurement system ALBATROSS-TT (3D-Arrangement for Laser Based Transmittance, Reflectance and Optical Scatter measurement - Table Top, Fig. 3.6) was used, which was developed at the Fraunhofer IOF and is described in detail in [77].

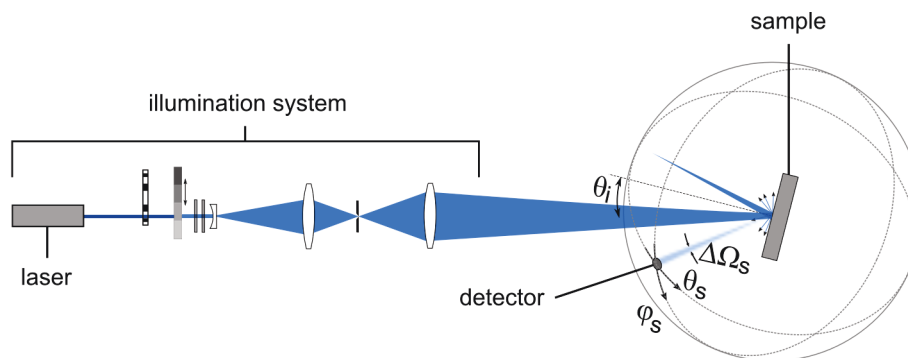


Fig. 3.6: Schematic illustration of the measurement system ALBATROSS-TT [77].

The sample is positioned in the center of the system and the angle of incidence is adjusted. The laser beam then illuminates the sample. A homogeneous laser beam is

achieved by an illumination system. By means of a three-dimensional positioning system, the ARS can be measured in the entire three-dimensional sphere [77, 78]. Subsequent, the TS value can be determined from ARS according to ISO standard (cf. Eq. (2.13) in section 2.3).

The instrument performance [77] is characterized by the low noise level of the ARS ( $2 \cdot 10^{-8} \text{ sr}^{-1}$ ) and a wide dynamic range of about 13 order of magnitude.

For the investigation of the nanorough optical surfaces the following parameters were used:

- wavelength:  $\lambda = 532 \text{ nm}$  (Nd:YAG laser)
- angle of incidence:  $\theta_i = 0^\circ$
- scatter angle:  $\theta_s$   $-85^\circ \dots -2^\circ, 2^\circ \dots 85^\circ, 95^\circ \dots 178^\circ$  and  $182^\circ \dots 265^\circ$

The light scattering measurements on the optical coatings which were performed during this work aimed at the assessment of the scatter loss with respect to the competitive interaction between specific surface roughness for optimal wettability and light scattering. Therefore, the calculated TS values can be compared to the light scattering threshold related to optical esthetic requirements, which are described in [63, 72]. Thereby, Flemming et al. established a reliable link between the visual inspection under different observation conditions and the measured TS levels. The study of samples with graduated scattering levels yield a TS threshold for the transmission hemisphere of  $0.22\% \pm 0.03\%$ . This definition of a visual acceptable threshold was determined for architectural glass and can be used for the investigation within this work.

#### 3.4 Spectrophotometry and data analysis

For the porosity and layer thickness estimation of the optical coatings with hydrophilic properties, a method consisting of spectrophotometric measurements as well as a subsequent analysis was used [53, 79-82]. This method was developed for comparable coatings in the framework of [51] based on the theoretical background of [83] and is summarized in the following.

For the spectrophotometric measurements to determine transmittance and reflectance, the UV/VIS/NIR spectrophotometer Lambda 900 and 950 from PerkinElmer was available at the Fraunhofer IOF. The absolute transmittance and reflectance measurements of the samples were performed at an angle of incidence almost normal to the surface ( $\approx 6^\circ$ ) and in a wavelength range from 300 nm to 1700 nm.

The first step to determine the porosity and layer thickness of an optical coating on glass is to measure the transmittance and reflectance spectra of an uncoated reference glass to obtain the optical constants of the glass substrate. Afterwards, the transmittance and reflectance spectra of the sample of interest have to be determined experimentally.

For the third step, a simulated model optimized for the specific thin film layer on glass is required. For the investigated samples in this thesis, the layer model developed by Schoeler [51] can be applied. The model for the porous SiO<sub>2</sub> layers on glass consists of a medium with two components (SiO<sub>2</sub> as host medium with vacuum filled pores) onto a glass substrate and surrounded by air. The medium with its structural properties is described by the Effective Medium Approximation according to Eq. (2.16). Thereby, the amorphous layer with the volume fraction of  $1 - F$  represents the host material and air with the volume fraction  $F$  represents the pore material air. It should be noticed that air as the pore material is an approximation for real coatings. In addition to the structural properties, the model considers the roughness induced light scattering behavior as well as an gaussian layer thickness variation to compensate inhomogeneities (cf. section 2.4).

Finally, the model spectra have to be approximated to the experimental transmittance and reflectance curves of the investigated samples through a variation of the model parameters: Layer thickness, porosity, and scatter loss of the interface. These parameters were systematically adjusted until a best fit is achieved (Fig. 3.7) and hence the resulting values of the model parameters are the estimated layer thickness and porosity of the investigated SiO<sub>2</sub> layers.

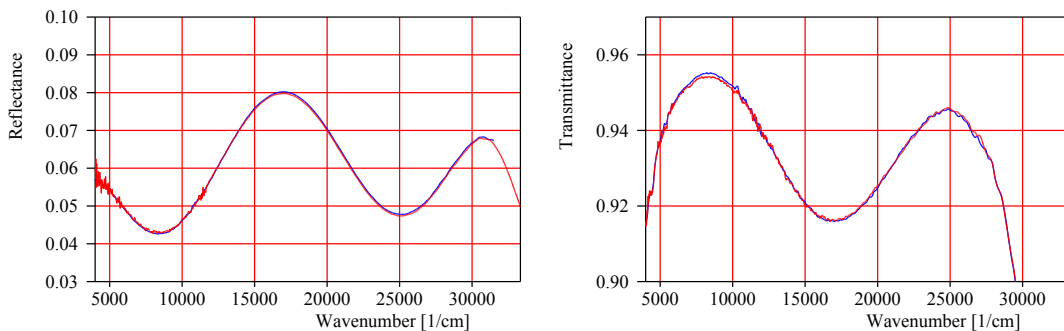


Fig. 3.7: Reflectance (left) and transmittance (right) curves of a one-sided coated sample (SiO<sub>2</sub> coating with SiO<sub>2</sub> nanoparticles). Red: measured curves. Blue: model spectra.

The analysis of low refractive coatings ( $n_{\text{air}} < n_{\text{coating}} < n_{\text{substrate}}$ ) leads to an ambiguity in the refractive index. To compensate this, part of the analysis was supplemented by measuring the transmittance and reflectance with s-polarized light and an angle of incident of 45°. This results in a shift of the reflectance and transmittance extremes and the ambiguity can be solved.

During the work of [51], selected samples were prepared with fine ditches and subsequently analyzed for layer thickness using AFM and scanning electron microscopy (SEM) to verify the determined values of the layer thickness using the presented method. The results showed that this method is suitable to determine the layer thickness of thin films in certain measurement uncertainty range.

Concerning the measurement uncertainty of the presented spectrophotometrical analysis, the uncertainty depends on specific coating condition and can amount up to 30%. Therefore, it has to be taken into account that the uncertainty for the porosity and layer thickness determination increases with decreasing layer thickness. Furthermore, an estimation of the porosity and layer thickness fails for samples with a high surface roughness or porosity and thus high scatter losses. In this case, it is not possible to compensate the scatter losses through the model parameters and thus the simulated spectra cannot adapt to the measured spectra. An example is given in section 7.3.

## **4 Relationships between the structural and wetting properties**

As early as 1964, Johnson and Dettre [4] wrote that the interpretation and discussion of experimentally determined wettability requires the understanding of the roughness effect. Hence, connecting the structural and the wetting properties is essential for designing and fabricating hydrophobic or hydrophilic surfaces as well as for a subsequent assessment of the resulting wetting behavior.

The classical relationship between roughness and wettability was introduced in section 2.2 through the Wenzel and Cassie-Baxter equations, which are only valid for mono-harmonic surfaces. These classical concepts can be used for the development of an approach based on the PSD analysis. This approach connects the roughness characteristic and hydrophobicity for stochastic rough surfaces.

The following considerations focus on the introduction of the approach and its extension capability to different kind of wetting systems. Furthermore, a first demonstration and validation of the approach using a natural example for superhydrophobicity will be presented.

The term “superhydrophobicity”, which is needed for the discussion in this chapter, will be introduced and discussed in detail in chapter 6.

### **4.1 Roughness and hydrophobicity**

Many practical approaches for realizing optimal hydrophobic wettability are published. However, concerning the relationship between surface roughness and wetting properties, it becomes apparent that most of the publications only investigate the wetting behavior without considering the structural properties (e.g. [10, 23, 84, 85]). On the other hand studies based on qualitative roughness assessment by means of SEM (e.g. [24, 58, 86-89]) or only used simple roughness parameters such as  $R_a$  and  $R_q$  values to characterize the surface morphology (e.g. [90-94]).

#### **4.1.1 Classical concepts**

For mono-harmonic surfaces, the classical relationships between the roughness properties and the hydrophobicity are given by the Wenzel equation (2.10) and the Cassie-Baxter equation (2.11). Johnson and Dettre used these relationships to simulate the roughness effect on the CA behavior for an idealized, mono-harmonic, and hydrophobic surface with an intrinsic CA of  $\theta_Y = 120^\circ$  [4], which is depicted in Fig. 4.1.



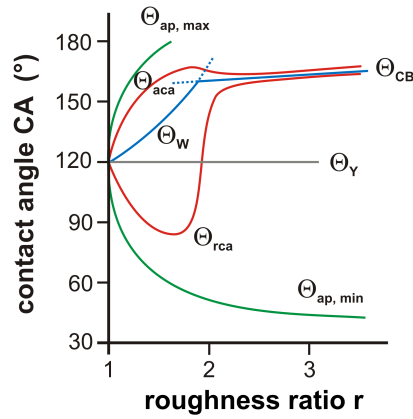


Fig. 4.1: Roughness effect on the CA for an idealized, mono-harmonic surface with an intrinsic CA  $\theta_Y = 120^\circ$  according to [4].

Fig. 4.1 shows the maximum and minimum possible apparent CA  $\theta_{ap}$  (green curve) and hence the wide range of metastable CA resulting from surface roughness and heterogeneities. Therefore, a sample with  $\theta_Y = 120^\circ$  can exhibit a  $\theta_{ap}$  clearly below  $90^\circ$  (cf. section 2.2). Furthermore, the most probable CA (blue curve) was calculated with the help of the Wenzel equation for “smooth” surfaces and the Cassie-Baxter equation for “rough” surfaces. The intersection point between both curves yields a hint, where the transition from homogeneous to heterogeneous wetting situation might occur. This transition can also be observed by the typical  $\theta_{aca}$  and  $\theta_{rca}$  behavior (red curves) depending on the surface roughness: During the homogeneous wetting state,  $\theta_{aca}$  and the CA hysteresis increase with rising roughness. At a certain roughness value,  $\theta_{aca}$  achieves saturation,  $\theta_{rca}$  abruptly increases and thus the CA hysteresis strongly decreases. At this point the heterogeneous wetting state is reached.

Almost all current publications which deal with the relationship between surface roughness (stochastic and deterministic) and wetting are based on the Wenzel and Cassie-Baxter equations. Since these concepts are valid only for mono-harmonic surfaces, they cannot be used to assess the roughness characteristics of real surfaces which are relevant for wettability. The Wenzel equation fails because an exact determination of the roughness ratio  $r$  is not possible over the entire dimension of the surface structure within a single scan area (cf. sections 2.1 and 3.1). In case of the Cassie-Baxter equation, the parameters roughness ratio  $r_f$  and fraction of projected surface area  $f_s$  cannot be determined theoretically or experimentally for stochastic rough surfaces. Until now, both parameters were simulated only for simple deterministic roughness structures [31, 72].

#### 4.1.2 The $\kappa_B$ approach

Even though the classical concepts derived by Johnson and Dettre are not applicable to real surfaces, these basic relationships can be advantageously used to transfer the findings for mono-harmonic surfaces to the roughness spectrum of stochastic structures. This resulted in a half-empirical relation of the roughness characteristic to the wetting behavior: The so-called wetting parameter  $\kappa_B$  is derived from the surface PSD and enables a separation of the influence of the roughness properties and the chemical material properties to the wettability. An overview of the algorithm to calculate the  $\kappa_B$  value from the PSD developed at the Fraunhofer IOF is given in [17, 26, 72] and summarized as follows:

- Transformation of the  $PSD(f')$  into an amplitude spectrum  $A(f)$  through:

$$A(f) = 2 \cdot \sqrt{\pi \cdot \int_{f/\sqrt{1.5}}^{f \cdot \sqrt{1.5}} PSD(f') \cdot f' \cdot df'} \quad . \quad (4.1)$$

- Calculation of the reduced amplitude spectrum  $A(f) \cdot f$ , and
- integration of  $A(f) \cdot f$  spectrum over the logarithmic spatial frequency range.

$\kappa_B$  hence represents a scale invariant parameter corresponding to the independence of the wetting properties of sinusoidal surface structures of their absolute magnitudes in the case of mono-harmonic surface roughness. Significantly different roughness structures can exhibit similar wetting properties. It should be emphasized again that the liquid drop size has to be sufficiently large compared to the roughness structure (cf. sections 2.2 and 3.2). This is also required for the  $\kappa_B$  approach.

Earlier experimental investigations of a sample series with varying surface roughness and equal hydrophobicity revealed  $\kappa_B$  as empirically related to the water CA and hence to the wetting behavior.  $\kappa_B$  of at least 0.3 was determined to be necessary for potential superhydrophobicity [28]. This criterion constitutes an essential condition, not a sufficient one.

In this thesis, the  $\kappa_B$  method will be extended and modified with regard to the novel wetting analysis methods including the novel criteria for superhydrophobicity (chapter 6) and with respect to different wetting systems (chapter 7). This addresses in particular the following questions:

- The validity range of the  $\kappa_B$  threshold has to be investigated. The earlier threshold of  $\kappa_B = 0.3$  was based on specific nanorough surfaces and on the definition of superhydrophobicity according to [72]. This means, during the

earlier investigations, hydrophobic zirconium oxide coatings with  $\kappa_B > 0.3$  and  $\theta_{aca} \geq 140^\circ$  were called superhydrophobic.

- The method has to be proven for microrough hydrophobic samples. In previous studies the  $\kappa_B$  approach was mainly utilized for nanorough optical surfaces [17, 26, 27].
- The possibility to extend the  $\kappa_B$  approach to hydrophilic wetting systems has to be examined.

Aside from the  $\kappa_B$  method, the only known work which is based on a PSD analysis for the roughness characterization can be found in [95]. In this publication, the roughness ratio of the Wenzel equation (2.10) is derived from the third moment of the PSD function in a first-order approximation using a Taylor series and assuming small slopes. This calculation results in a so-called Wenzel roughness function  $R_W(\xi)$  with  $\xi$  being the reciprocal wavelength. Afterwards, a threshold for superhydrophobicity (appropriate to the most common definition  $\theta_{ap} > 150^\circ$ , see section 6.1.1) was calculated from Eq. (2.10) for a certain intrinsic wetting property. This implies that a surface structure with, for instance,  $\theta_Y = 120^\circ$  (perfluoroalkanes) requires a critical roughness ratio  $r_W^*$  of 1.5 to theoretically achieve  $\theta_{ap} > 150^\circ$ . For the correlation research, isotropic, homogeneous, and randomly rough surfaces were characterized using a PSD analysis. For each sample the Wenzel roughness functions  $R_W$  were then determined and compared to the observed hydrophobicity. The results lead to the conclusion that superhydrophobic surfaces are surfaces with a  $R_W$  function exceeding the critical value of  $r_W^* - 1$  below a spatial frequency of  $10 \mu\text{m}^{-1}$ .

As the  $\kappa_B$  method, the concept in [95] is based on a complex roughness characterization by means of PSD analysis. Furthermore, the term “superhydrophobic” was defined not only by a high CA, but also by a small CA hysteresis and small roll-off angle (cf. section 6.1.1). Nevertheless, this concept reveals three major disadvantages compared to the  $\kappa_B$  approach:

- The concept is not scale invariant: The spatial frequency bandwidth, in which  $R_W$  has to reach the critical value  $r_W^* - 1$ , was restricted to a range of  $0.1 \mu\text{m}^{-1} \leq f \leq 10 \mu\text{m}^{-1}$ . In contrast,  $\kappa_B$  represents a scale invariant parameter. As will be shown in chapter 7, the wetting-relevant spatial frequency range depends on the type of the roughness structure (micro-scale or nano-scale or combination of both).
- The concept uses a critical roughness ratio  $r_W^*$  for superhydrophobicity, which strongly depends on the respective chemical surface properties. In contrast, the  $\kappa_B$  method provides the possibility to assess the roughness characteristic

concerning superhydrophobic wettability separated from the chemical conditions of the surface under study.

- The concept is based on the determination of the Wenzel roughness ratio  $r$  using a Taylor series. Accordingly, the approach is mathematically restricted to roughness structures with small slopes. This is contradictory to the fact that superhydrophobicity requires a certain surface roughness with “high” slopes of the roughness components.

Furthermore, the  $\kappa_B$  method allows determining the wetting-relevant spatial frequency range of a stochastic rough surface and hence the type of roughness structure (micro-scale or nano-scale or combination of both) which mostly influences the wettability.

After the introduction of the  $\kappa_B$  approach as well as its advantages and challenges, the typical natural example for superhydrophobicity - the lotus leaf - is used to demonstrate and validate this method. In Fig. 4.2 a photograph and REM images of a lotus leaf are shown. Similar qualitative presentations of the leaf morphology can be found in a large number of publications [10, 23, 87, 96] in which the hierarchical or two-scale structure consisting of papillae (microstructure) and hydrophobic wax crystals (nanostructure) is described. Based on these qualitative descriptions, many papers conclude that hierarchical roughness structures are required to realize superhydrophobic wetting properties (e.g. [10, 19, 24, 93, 97-99]). However, the following roughness analysis including the  $\kappa_B$  method of a dried lotus leaf will show that these conclusions are invalid.

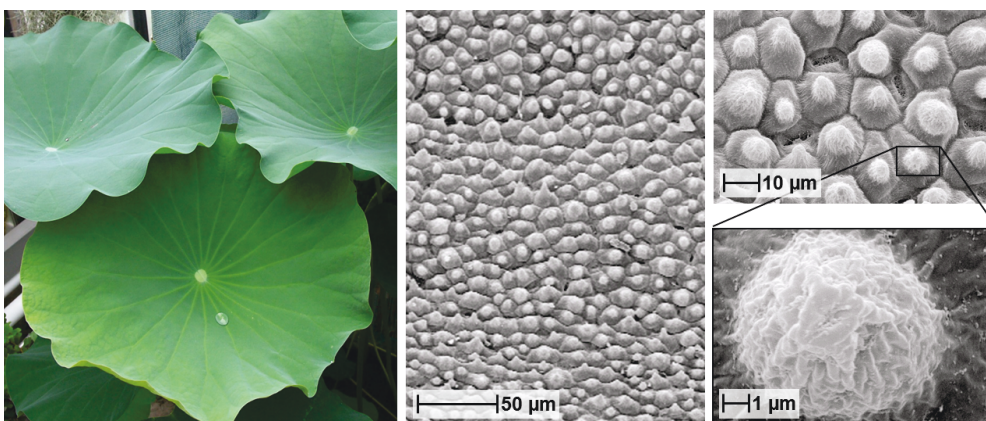


Fig. 4.2: Photograph of lotus leaf with a water drop (left) and REM images of dried lotus leaf (right) [27].

The roughness characteristics and PSD function of lotus leaves (Fig. 4.3) were calculated from the WLI topography data between a spatial frequency of  $0.01 \mu\text{m}^{-1}$  and  $10 \mu\text{m}^{-1}$  for the first time. In a former work [27] the roughness components could

only be measured up to a frequency of  $1 \mu\text{m}^{-1}$  and the PSD function at higher spatial frequencies had to be extrapolated.

Based on the PSD determined within this PhD thesis, the contributions to the  $\kappa_B$  value were calculated for each decade in which the roughness components are completely available. The results are also given in Fig. 4.3.

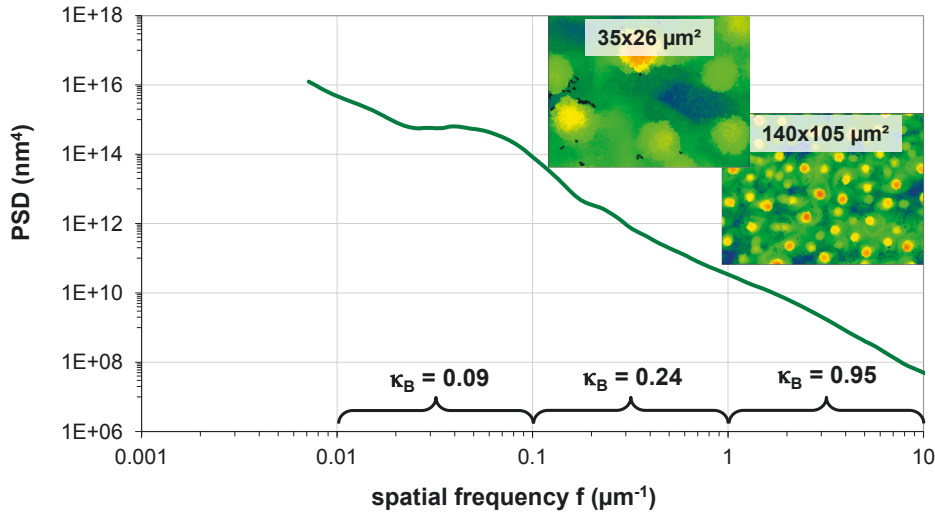


Fig. 4.3: PSD function and wetting parameter of dried lotus leaf. Embedded picture: WLI topography images.

The summarized  $\kappa_B$  value ( $0.01 \mu\text{m}^{-1} \leq f \leq 10 \mu\text{m}^{-1}$ :  $\kappa_B = 1.28$ ) of the lotus leaf as classical example for self-cleaning clearly exceed the threshold for superhydrophobicity.

The general assumption for the lotus leaf in the literature [100-103] is that the microstructure of the papillae in combination with the nanostructure of the wax crystals are responsible for the superhydrophobicity. The microstructure can be seen as hump in the PSD function. Nevertheless, the contribution to the  $\kappa_B$  value in the spatial frequency range where the microstructures are taken into account ( $0.01 \mu\text{m}^{-1} \leq f \leq 1 \mu\text{m}^{-1}$ ) is clearly smaller than the contribution in the higher spatial frequency range ( $> 1 \mu\text{m}^{-1}$ ). Consequently, the superhydrophobicity of the lotus leaf ( $\theta_{aca} = 152^\circ$ ,  $\theta_{rca} = 147^\circ$ , water drops easily roll off a  $2^\circ$  tilted surface) is caused by the nanostructures rather than by the prominent papillae. This also means that hierarchical roughness structures are generally not necessary to achieve superhydrophobic wettability. This conclusion will be substantiated by means of examples of technically fabricated samples in chapter 7.

Furthermore, the group of Barthlott [104] recently reported that a comparison of the mechanical stability between the lotus leaf with its micro-scale papillae and the leaves without papillae leads to the following presumption: The papillae protect the wax crystals between each other, by which the lotus leaf keeps its excellent hydrophobic wetting properties after mechanical stress in contrast to the other kind of leaves for

which the CA decreased by around  $35^\circ$ . These observations could explain the real purpose of the striking humpy microstructure: Mechanical stability rather than superhydrophobicity. The latter is induced by the wax nanostructure crystals, which now could be proven quantitatively for the first time through the  $\kappa_B$  method.

## 4.2 Roughness / porosity and hydrophilicity

Dettre and Johnson not only discussed the effect of surface roughness on hydrophobicity, but also the roughness influence on hydrophilicity. For this purpose, a wetting simulation of an idealized, mono-harmonic surface with  $\theta_Y = 45^\circ$  was performed, which is presented in Fig. 4.4.

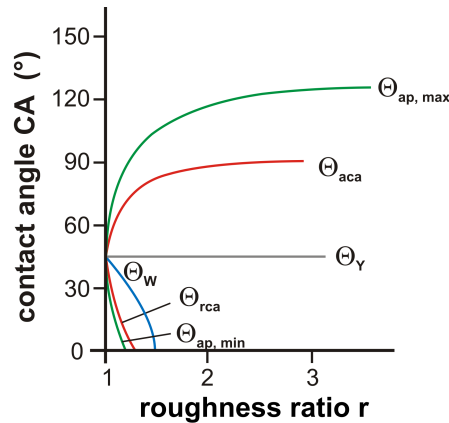


Fig. 4.4: Roughness effect on the CA for an idealized, mono-harmonic surface with an intrinsic CA  $\theta_Y = 45^\circ$  according to [4].

For intrinsic hydrophilic surfaces, a rising surface roughness leads to a steady increase of the CA hysteresis (red curves), analogous to hydrophobic surfaces in the homogenous wetting state. In addition, CA considerably higher than  $90^\circ$  can appear (cf. green curve), because of the existence of metastable CA. Above a certain roughness ratio, the surface is completely wetted (blue curve,  $\theta_{ap} = 0^\circ$ ) [4]. This particular case is not only caused by a specific surface roughness, but also because of the appearance of porosity. The pores lead to a penetration of the liquid phase into the surface structure, which is called wicking effect [15, 50, 105, 106].

The number of publications related to hydrophilicity increases steadily every year [13]. A detailed consideration of the current international published findings leads to the conclusion that the activities for this topic are obviously less than those for hydrophobicity. This is even more the case, if papers dealing with hydrophilic photocatalytic coatings are excluded from consideration.

As for hydrophobic surfaces, the classical relationships for mono-harmonic surfaces were used in the publication to describe the influence of the surface

roughness on the hydrophilic wettability. However, a large number of published studies concerning the relationship between structural properties and hydrophilicity describe the surface characteristics only by qualitative images determined through SEM [11, 105, 107] or through simple roughness parameters calculated from the topography [15, 108, 109]. Additionally, many works deal either with the surface roughness or the porosity effect on the wettability and neglect the influence of the respective other structural parameter. Extremely rarely both are considered. As one of the few, Law et al. [49] investigated the layer thickness and the particle size influence on the CA behavior of titanium oxide coatings: It could be observed that the best wetting results can be found for coatings with the highest rms roughness realized by a layer thickness of 140 nm and smallest particle diameter of about 60 nm. Particles with this size compared to larger particles lead to the most pores in the thin film structure.

Concerning the utilized wetting analysis methods of the recently published studies, the CA behavior is mostly sufficiently characterized [11, 15, 49, 110, 111]. Nevertheless, quantitative methods to assess the observed fogging behavior are missing [15, 16, 50, 112, 113].

In the context of this PhD work, first systematical investigations about the relationship between the structural properties and hydrophilicity were performed. Therefore, intrinsic hydrophilic samples with different surface roughnesses were studied using the PSD analysis in connection with a  $\kappa_B$  determination for the roughness characterization. In contrast to hydrophobic wetting systems, previous investigations are not available. This means that the possibility of an extension of the  $\kappa_B$  approach to hydrophilic wetting systems was proven for the first time within this thesis. Furthermore, the influence of the porosity on the hydrophilicity was examined. The results will be presented in section 7.3. Moreover, the characteristic hydrophilic wetting quantities which are necessary for the correlation tests will be presented in section 6.2.

## 5 Samples

Optical and engineering surfaces with nano- or microstructures were characterized in order to develop the roughness and wetting analysis methods as well as to investigate the correlation between the roughness, wettability, and optical properties. Various fabrication processes were chosen for the sample generation to achieve different structural properties.

Hydrophilic wetting properties were examined on porous and nanorough oxidized sol-gel coatings, which are intrinsic hydrophilic (Fig. 5.1 left). Roughness-induced hydrophobicity was studied with the help of nanorough oxidized sol-gel coatings and sputtered coatings as well as microrough aluminum surfaces. All type of samples are intrinsic hydrophilic. Hence, a hydrophobic thin top layer has to be applied onto the roughness structure to achieve hydrophobic wetting properties (Fig. 5.1 right).

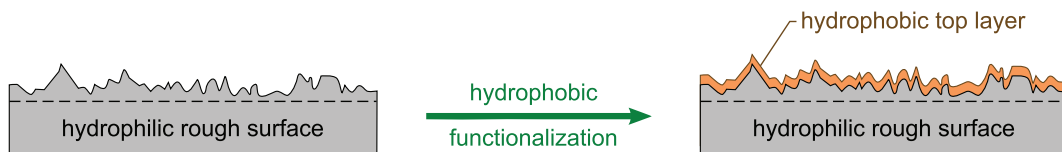


Fig. 5.1: Wetting properties of investigated samples. Left: Rough and intrinsic hydrophilic surface. Right: Rough surface with a hydrophobic top layer.

In this chapter an overview of the fabrication processes of the investigated samples is given including the process parameters and the main reasons for selecting specific thin film layer materials. Finally, the name and the process parameters of each sample are summarized in tabular form.

### 5.1 Nanorough optical coatings

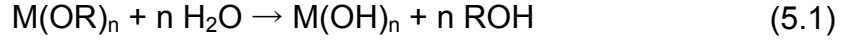
The surface nanostructures are realized by optical coatings. Thereby, particular attention has to be paid to the surface roughness in order to fulfill the visual application requirements of drinking and decorating glasses or glasses for mirrors and shower cubicles in the bathroom. For this reason, the main contribution to the surface roughness, which is essential for special wetting behavior, has to be in an optically negligible bandwidth ( $f < 2.5 \mu\text{m}^{-1}$ ), which can be realized by nano-scale roughness. In this case the scatter losses induced from surface roughness are tolerable (cf. section 3.3).

#### *Sol-gel coatings*

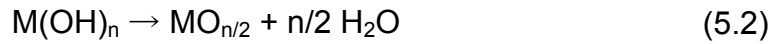
Nanostructured sol-gel coatings were produced by wet chemical reactions of metal alkoxides to synthesize a gel on the basis of a sol at ETC PRODUCTS GmbH [114].



The wet chemical reactions of the sol-gel technique are hydrolysis and condensation [31, 115, 116]. During the hydrolysis reaction, an alkoxide of a metal (M) reacts with water to a hydroxide and a corresponding alcohol [117]:



The resulting hydroxides polymerize with each other, and particles with a diameter of 1 nm up to 100 nm are formed from the precursors [117]:



Both equations are generalized. For real systems the chemical reactions are more complicated.

The sol-gel coatings used in this thesis were deposited by a dip coating process, in which the substrate is dipped into the solution and then removed out of the liquid with a constant velocity. Through vaporization of volatile matter, the sol film transforms to a gel film. Finally, a thin film layer, which strongly adheres to the substrate surface, is formed during a thermal treatment [31].

Aluminum oxide ( $Al_2O_3$ ) and silicon oxide ( $SiO_2$ ) were chosen as thin film materials because the structural properties, such as surface roughness, porosity, and layer thickness, could be varied easily and systematically using the sol-gel process and the dip coating technique. For instance, the thin film roughness of  $Al_2O_3$  layers with a thickness of approximately 250 nm can be influenced by a thermal treatment. The hydrophilic samples were realized with  $SiO_2$  layers of approximately 120 nm thickness and embedded  $SiO_2$  nanoparticles. These nanoparticles were available in a large variation of particle diameter ( $d_{particle}$ ) and particle concentration ( $c_{particle}$ ). In addition, the withdrawal velocity ( $v_{draw}$ ) and number of dipping iteration ( $N_{dip}$ ) of the sol-gel process can be easily changed. This leads to a variation of surface roughness, porosity, and film thickness of the nanorough coatings [17].

The variation of all process parameters is important to precisely adapt the wetting properties in order to achieve a self-cleaning or anti-fog effect. A main disadvantage of the sol-gel coatings is the mechanical instability. However, the focus of this work lies on the structural and wetting properties and not the mechanical stability of the samples.

### *Sputtered coatings*

In a second fabrication process nanorough zinc oxide (ZnO) thin film layers were deposited by high power impulse magnetron sputtering (HiPIMS), which is a high-

energy physical vapor deposition (PVD) technique [118]. The coatings were sputtered at the Fraunhofer IST [119].

The HiPIMS process is performed in a vacuum chamber in which two magnetron targets (cathode) with bipolar potentials are located towards the substrate (anode). After the recipient is filled with argon as process gas, the target is sputtered through the bombardment with high-energy ions, and the zinc atoms move through the vacuum chamber to deposit onto the substrate. The presence of oxygen as reactive gas leads to the formation of ZnO [120-122].

The main advantages of the HiPIMS technique compared to conventional sputtering processes are the high plasma density and the high fraction of the ionized sputtering material. As a result an improved control of the film growth can be achieved leading to excellent film properties such as high density, improved adhesion, hardness as well as surface roughness and coatings with better optical properties [118, 121, 123, 124].

In the “Diplomarbeit thesis” [31] the roughness structure of sputtered zirconium oxide and yttrium doped zirconium oxide coatings were examined. It became apparent that the sputtered coatings of these materials were not sufficient to achieve suitable roughness structures, which in combination with a hydrophobic functionalization would yield superhydrophobic wettability. For this reason, ZnO was chosen as an alternative sputtering material to fabricate roughness structures with a sufficiently high aspect ratio. The thin film material ZnO also exhibits columnar growth [125] and a distinct crystal orientation during the growth. Thus, smaller width of structures can be realized compared to the width of zirconium oxide structures. This is not solely important for specific wettability but in addition for excellent optical quality [122].

To receive surface characteristics with optimal functional properties, different process parameters were systematically varied: target bias, oxygen partial pressure, and layer thickness. The assessment of the resulting surface quality was performed with the help of the roughness based wetting parameter. However, an increasing surface roughness causes an increased scatter loss of the sample as discussed by means of Eq. (2.12). Therefore, for a further sample series a two-step growth process with plasma treatment was performed to realize surface structures with an improved aspect ratio and steady lateral dimensions. The aim was to achieve small width of the ZnO structures through an initially low oxygen partial pressure and to influence especially the surface texture by a plasma treatment. Subsequently, a deposition of a second ZnO layer under a high oxygen partial pressure should result in an increased height of the roughness structure [122].

The sol-gel coatings were deposited onto soda lime glass plates. For the sputtered nanorough coatings, crystal glass slices were used.

Because all oxidized coatings are intrinsic hydrophilic, the  $\text{Al}_2\text{O}_3$  and ZnO thin film layers have to be overcoated with a hydrophobic top layer (see Fig. 5.1 right and section 5.3) to investigate the relationship between surface roughness and hydrophobicity. The  $\text{SiO}_2$  coatings required no additional chemical functionalization because for these sample the hydrophilicity is of interest.

An overview of the samples including information about the process parameters is given in section 5.4.

### 5.2 Microrough engineering surfaces

Within the frame of this work, the investigation of the correlation between the surface roughness and hydrophobicity are focused on nanorough coatings for optical applications. In addition to these nanostructures, the influence of microstructures on the wettability of engineering surfaces is of interest, too. For this purpose, the university UFRGS in Brazil [126] provided four polished aluminum sheets with different surface characteristics to achieve superhydrophobicity. The specific samples are listed in section 6.4

The aluminum substrates were structured by two different methods: chemical etching and electrochemical anodization. The polished substrates were dipped into a concentrated solution of hydrogen chloride for a defined time [127] to roughen the surfaces by chemical etching. Otherwise, anodization is a process where an oxide film is produced by an electrochemical oxidation of the aluminum. The resulting film is denoted as anodic aluminum oxide. During the anodization in an electrochemical cell, water molecules split into  $\text{O}^{2-}$  and  $\text{OH}^-$  anions at the interface oxide - electrolyte. Afterwards, the anions react with aluminum ions or move to the aluminum surface. At the metal - oxide interface, the aluminum is oxidized to  $\text{Al}^{3+}$  cations. These cations either react with the  $\text{O}^{2-}$  and  $\text{OH}^-$  anions to form  $\text{Al}_2\text{O}_3$  or move to the electrolytes [128]. The electrolytes can be changed in concentration, temperature, and pH-value. Furthermore, the applied potential voltage and the duration of treatment can be adjusted to influence the formation of the film. The exact process parameter can be found in [127].

After structuring the aluminum sheets, the four samples were overcoated with trimethoxypropylsilane (TPMSi) and a top layer of polytetrafluoroethylene (PTFE) to achieve hydrophobic wetting properties. TPMSi forms a covalent bonding with the Al substrate as well as with the PTFE and was applied by sol-gel technique via dip coating. PTFE was deposited by PVD [129].

### 5.3 Hydrophobic functionalization

As mentioned at the beginning of this chapter, the oxidized coatings (sol-gel and sputtered) are intrinsic hydrophilic (Fig. 5.1 left), which means that the SiO<sub>2</sub> thin films does not need any further steps of preparation for hydrophilic applications. In contrast, to correlate the surface roughness and hydrophobicity by means of Al<sub>2</sub>O<sub>3</sub> and ZnO thin films, a hydrophobic top layer with a low surface energy on the top of the roughness structure is required (Fig. 5.1 right). For the sake of simplicity the hydrophobic top layer is just denoted as top layer from now on.

Particularly effective for decreasing the surface energy, and hence increasing the hydrophobicity, are top layers containing fluorine [130]. Nevertheless, previous studies within the “Diplomararbeit thesis” [31] and this thesis indicated that a variety of influencing factors of the top layer significantly affect the wetting behavior. These are:

- The material of the top layer (i.e. the intrinsic CA),
- the chemical and physical bonding between the roughness structure and the top layer,
- the deposition process and the point of deposition time of the top layer, and
- the thickness of the top layer.

As a consequence, for every changed system (i.e. material and dimension of the roughness structure) the chemical functionalization through a top layer has to be examined and adapted. Thereby, the main demand is that the top layer should not influence the roughness characteristic: no smoothing or roughing. A systematic investigation of these aspects would however go beyond the scope of this work. Anyhow, in a previous test the intrinsic CA of the used top layers on pure glass substrates were determined. Yet, basic investigations concerning the influence of the deposition time as well as the material of the top layer were performed.

The Al<sub>2</sub>O<sub>3</sub> and ZnO nanostructures were overcoated with a fluoroalkylsilane layer of about 5 nm thickness using the dip-coating technology. This standard top layer denoted as PolyF1 exhibits a  $\theta_{aca} = 108^\circ$  and  $\theta_{rca} = 88^\circ$  on pure glass substrates and was prepared at ETC PRODUCTS GmbH [114].

Beside PolyF1 a further hydrophobic material was utilized. The main idea of this second hydrophobic material was to shorten the time between the deposition of nanorough ZnO layers and the overcoating with a top layer. A fluoroalkylsilane from Merck KGaA was a suitable choice, because this product could be applied at Fraunhofer IST. Thus, the Fraunhofer IST manufactured both, the rough ZnO thin films and the top layers [119]. According to [131] and the results of a previous wetting analysis, the material WR4<sup>®</sup> exhibits the best hydrophobic wetting properties (lowest

surface energy: 13.8 mN/m, highest CA:  $\theta_{aca} = 115^\circ$  and  $\theta_{rca} = 107^\circ$ ) with good adhesion on oxidized coatings, which are offered by Merck. The thickness of the top layer WR4<sup>®</sup> was optimized for hydrophobicity depending on the ZnO thin film roughness. Under the present circumstances, the maximum thickness of the WR4<sup>®</sup> layer is 20 nm.

In the subsequent chapter 6, ZnO coatings were characterized for the development of the wetting analysis methods. Only for these samples, a further preparation step was performed to enhanced the hydrophobicity before the ZnO roughness characteristic was overcoated with PolyF1: An adhesive silicate layer was deposited through a flame treatment [114, 132, 133] onto the ZnO thin film to improve the bounding of the top layer to the roughness structure.

### 5.4 List of samples

The investigated samples as well as the corresponding process parameters are listed in the following tables. Tab. 5.1 refers to the nanorough optical coatings for hydrophobic applications. Tab. 5.2 summarizes the nanorough optical coatings for hydrophilic wettability. Finally, the microrough engineering samples are summarized in Tab. 5.3 on the next page.

## 5 Samples

Tab. 5.1: Nanorough optical coatings for hydrophobic application.

sample	process parameter	material of top layer
<i>sputtered ZnO coatings for wetting analysis (chapter 6)</i>		
<b>F1</b>	d = 1.3 μm; 1x flame treatment	PolyF1
<b>F2</b>	d = 1.3 μm; 2x flame treatment	
<b>F3</b>	d = 1.3 μm; 4x flame treatment	
<i>Al<sub>2</sub>O<sub>3</sub> sol-gel coatings (characterization in chapter 7)</i>		
<b>A1, A2</b>	thermal treatment	PolyF1
<b>A3</b>	without thermal treatment	
<i>sputtered ZnO coatings (characterization in chapter 7)</i>		
<b>Z0</b>	d = 0.6 μm	PolyF1
<b>Z1</b>	d = 1.3 μm	
<b>Z2, Z3, Z4</b>	d = 1.8 μm	
<b>Z5</b>	d = 2.0 μm	
<b>Z6</b>	d = 2.4 μm	
<b>Z7</b>	d = 2.0 μm; Ar plasma (t = 5 min)	
<b>Z8</b>	d = 2.0 μm; Ar plasma (t = 10 min)	
<b>Z9</b>	d = 2.0 μm; Ar-O plasma (t = 5 min)	
<b>Z10</b>	d = 2.0 μm; Ar-O plasma (t = 10 min)	PolyF1
<b>Z11</b>	d = 2.4 μm	WR4 (d = 2.5 nm)
<b>Z12</b>	d = 2.4 μm	WR4 (d = 5.0 nm)
<b>Z13, Z15</b>	d = 1.8 μm	WR4 (d = 15 nm)
<b>Z14, Z16</b>	d = 1.8 μm	WR4 (d = 20 nm)

Tab. 5.2: Nanorough SiO<sub>2</sub> sol-gel coatings for hydrophilic application.

sample	varying process parameter	constant process parameter
<b>S1 ... S3</b>	v <sub>draw</sub> : (1; 5; 7) mm/s	d <sub>particle</sub> = 20 nm; N <sub>dip</sub> = 10; c <sub>particle</sub> = 1% w/w
<b>S4 ... S7</b>	N <sub>dip</sub> : 5; 10; 15; 20	d <sub>particle</sub> = 20 nm; c <sub>particle</sub> = 1% w/w; v <sub>draw</sub> = 1 mm/s
<b>S8 .. S11</b>	d <sub>particle</sub> : (5; 15; 35; 50) nm	N <sub>dip</sub> = 15; c <sub>particle</sub> = 1% w/w; v <sub>draw</sub> = 1 mm/s
<b>S12 ... S14</b>	c <sub>particle</sub> : (0.6; 1.0; 1.4)% w/w	d <sub>particle</sub> = 35 nm; N <sub>dip</sub> = 15; v <sub>draw</sub> = 1 mm/s

Tab. 5.3: Microrough engineering samples for hydrophobic application.

sample	roughness structure	material of top layer
<b>E1</b>	-	silane and PTFE
<b>E2</b>	nanostructure	
<b>E3</b>	microstructure	
<b>E4</b>	nano- and microstructure	

## 6 Advanced wetting analysis

For a first assessment of wetting properties of different solid surfaces, basic CA measurement methods such as a simple apparent CA of a sessile drop are often used. Nevertheless, this kind of simplicity leads to a great variation in the performance and evaluation of the CA behavior depending on the specific analysis conditions: It is rather difficult to compare wetting properties resulting from different wetting analysis methods.

In this chapter, the development of advanced methods for a more thorough wetting analysis are described in detail with the aim to characterize hydrophobic or hydrophilic wettability and to identify as well as classify extreme wetting properties. For this purpose, the most suitable measurement and evaluation methods were selected based on the experience from previous studies such as [31, 72]. These methods were optimized and advanced with novel methods according to the specific wetting systems investigated in this thesis. Afterwards, novel wetting criteria for extreme hydrophobic and hydrophilic wettability were acquired based on the comprehensive wetting analysis methods.

### 6.1 Hydrophobic surfaces

In the current section, a comprehensive wetting analysis for hydrophobic surfaces and its achievement is developed. First, the term superhydrophobicity is introduced using international published definitions as well as findings of previous studies. Afterwards, the development of the wetting analysis methods is explained and illustrated. Finally, novel criteria for superhydrophobicity are introduced based on the findings acquired within this work.

#### 6.1.1 Superhydrophobicity: Common definitions

Intrinsically hydrophobic surfaces exhibit CA of  $\theta_Y > 90^\circ$  according to the Young equation (2.8). The highest observed intrinsic CA of water drops on smooth surfaces is approximately  $120^\circ$ , which occurs on solids with regularly aligned closest-hexagonal-packed  $\text{CF}_3$  groups ( $\gamma_1 = 6.7 \text{ mJ/m}^2$ ) [134, 135]. To reach extreme hydrophobic wettability with  $\theta_{ap} > 120^\circ$ , a combination of low surface tension and specific surface roughness is required [7, 127]. More precisely, wetting has to occur in the heterogeneous wetting state, for which a surface with a sufficiently high aspect ratio of the roughness structure is essential [136]. This relationship between the surface roughness and wetting behavior was discussed in detail in section 4.1.

In everyday life as well as in science, excellent hydrophobic wettability appears quite often. Nevertheless, there is neither a generally accepted term nor a definition

in literature, though the publications of Marmur [5, 6, 39, 136] provide the theoretical basics for a complete definition.

In this thesis, the most common term “superhydrophobicity” is used. Alternative wording, such as “ultrahydrophobic”, “nonwetable”, “extremely water repellent”, “superhydrophobic”, etc., can also be found [8, 39]. To illustrate the large variety in this field, some frequently published definitions are summarized.

The simplest definition of superhydrophobicity found in literature [9, 18, 85, 92, 137, 138] only requires a CA > 150° as threshold without further specification. Besides the CA, the observation of water drop movements on minimally tilted surfaces was used to identify superhydrophobic wettability [93, 97, 139-142]. However, only a few works consider the importance of the CA hysteresis, as presented in section 2.3 and 4.1. In [23, 86, 95, 143-145] superhydrophobicity is defined by both a CA > 150° and a small CA hysteresis. If both criteria are met, water drops do not adhere on minimally tilted surfaces. Very rarely, the CA behavior is specified using  $\theta_{aca}$  and  $\theta_{rca}$  [146, 147], or the slide-off and roll-off behavior is correctly distinguished [7, 104, 127, 148, 149]. A slide-off behavior of water drops on tilted surfaces is accompanied by homogeneous wetting and thus only possible for hydrophobic wettability.

Aside from the different definitions, almost all investigations of superhydrophobic surfaces aim at realizing the so-called self-cleaning effect. This effect is based on a high aspect ratio of the roughness structure in the heterogeneous wetting state: The contact area between the particle and the solid surface is considerably smaller than the contact area between the particle and the water drop which minimizes the adhesion forces. Thus, particles adhere to the surface of the water drops and are removed by tilting the sample [136] as illustrated in Fig. 6.1.

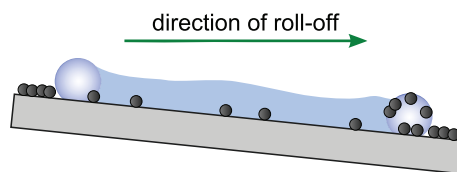


Fig. 6.1: Schematic illustration of the self-cleaning effect by a rolling drop.

### 6.1.2 Comprehensive wetting analysis methods

For the characterization of the wide range of metastable  $\theta_{ap}$  resulting from surface roughness and chemical heterogeneities (cf. Fig. 2.3 in section 2.2), it is necessary to determine the highest and lowest values within this CA range of the real wetting system. This implies that  $\theta_{aca}$  and  $\theta_{rca}$  of sessile drops have to be measured by varying the drop volumes using the needle-in-drop method [17, 38].



For the  $\theta_{aca}$  and  $\theta_{rca}$  measurements, a liquid drop with a defined volume ( $10 \mu\text{l}$ ) is deposited onto the solid surface. Then, the measurement parameters such as dosing volume ( $50 \mu\text{l}$ ) and dosing rates ( $0.5 \mu\text{l/s}$ ) are specified. During the variation of the liquid drop volume, the drop shape follows a characteristic cycle, which is described in detail in [38], and summarized in [17, 31, 72]: While increasing the volume of the drop, the contact points initially seem to be fixed until the highest CA ( $\theta_{aca}$ ) is reached. By decreasing the volume,  $\theta_{rca}$  becomes apparent (as the minimum CA) and the contact points recede (see embedded images in Fig. 6.2). The CA behavior during this cycle is continuously recorded with a video system, and the recorded data is then evaluated by an automated drop shape analysis. For the characterization of wettability based on  $\theta_{aca}$  and  $\theta_{rca}$ , the standard calculation method used for the drop shape analysis is the tangent leaning method. In doing so, the solid surface is defined by a moveable baseline, whereby both contact points of the liquid drop are identified and in this region the drop contour is approached by a polynomial fit of fifth order. Then, the tangent of the drop shape at each contact point is determined and the  $\theta_{ap}$  are the slopes of the tangents. The advantage of this method is that asymmetrical drops can also be analyzed, which occur for non-ideal surfaces.

Based on the tangent leaning method, each frame of the recorded drop shape behavior is analyzed. The resulting CA is plotted as a function of the frame number.  $\theta_{aca}$  and  $\theta_{rca}$  are then defined as the arithmetic average of all CA in the range of the first and second plateau, respectively. Fig. 6.2 shows an example of such a measurement.

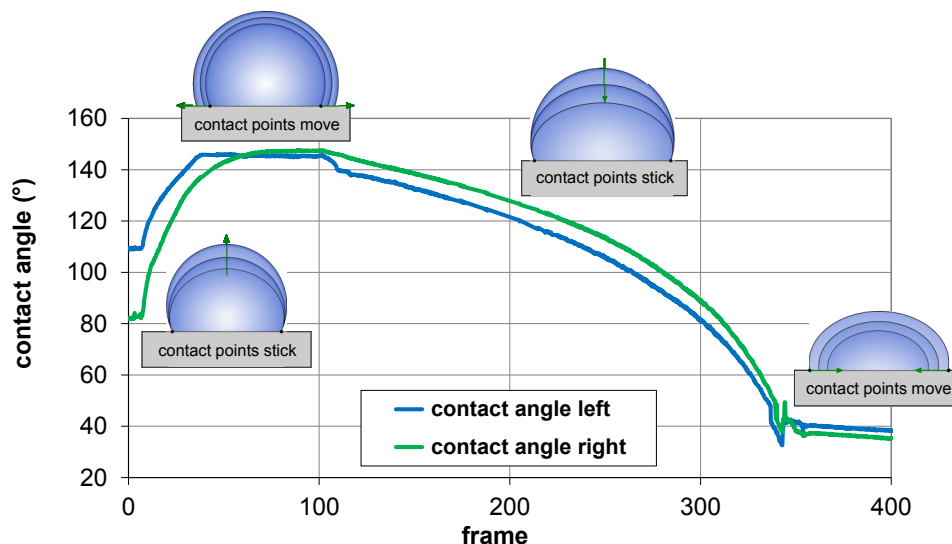


Fig. 6.2: CA as a function of the frame including the cycle of the advancing and receding CA.

Within the framework of this thesis, the examinations of hydrophobic surfaces led to the conclusion that for the analysis of the plateaus the arithmetic average cannot be used for all wetting systems because stick-slip behavior is observed during drop

movement, which causes oscillations within the plateaus. In these cases, direct comparisons of the frames between the plotted CA data and the recorded CA behavior is necessary to identify the evaluable frames.

Furthermore, the  $\theta_{\text{rca}}$  determination becomes more complicated with decreasing the  $\theta_{\text{rca}}$  and completely fails for surfaces with  $\theta_{\text{rca}} < 20^\circ$ . To optimize the analysis of the receding drop behavior, the dosing rate was reduced to 0.2 mm/s for the determination of  $\theta_{\text{rca}}$ . This adaptation leads to a substantial improvement of wetting analysis because the analysis is closer to the thermodynamical equilibrium of the wetting systems with an acceptable increase of measuring time. Furthermore, the dosing volume of the  $\theta_{\text{rca}}$  determination can be increased to 60  $\mu\text{l}$  for an improved analysis of the receding drop behavior. As a result,  $\theta_{\text{rca}}$  up to values around  $5^\circ$  can be measured.

In addition to the CA, knowledge of the slide-off and roll-off behavior of water drops is crucial for a meaningful wetting analysis of hydrophobic surfaces [75, 150]. Technically, this special wetting performance is characterized using the motorized tilting base unit of the CA measuring instrument OCA 20, which can rotate about its horizontal axis up to  $90^\circ$ . During the measurement, the video system continuously records the inclination angle of the CA measuring instrument, the drop shape, and the motion of the drop.

For the characterization of drop movement of a liquid on a solid, a drop with a volume of 30  $\mu\text{l}$  is deposited onto the sample surface. The sample is then tilted with a constant and the lowest possible velocity. During the inclination of the sample, the drop is initially pinned at its position and the drop shape becomes asymmetrical because of the downhill force. When reaching a critical tilt angle, the drop slides or rolls off the surface. The roll-off or slide-off angle  $\alpha$  is then defined as the minimum tilt angle at which a drop starts sliding or rolling off the surface [31, 72]. It is not unusual that a drop stays pinned at its start position until the maximum inclination angle is reached. For the sake of simplicity, the slide-off and roll-off angles are denoted as tilt base angle  $\alpha$  in the following. It is interesting to note that  $\alpha$  is directly connected to the width of the CA hysteresis [7, 17, 151].

The methods introduced above were applied to a first sample series consisting of three sputtered ZnO thin film layers with hydrophobic top layers. The samples differ in the varying number of flame treatment processes (see section 5.3).

As the wetting analysis results in Fig. 6.3 show, sample F1 exhibits comparable wetting properties as the classical example for superhydrophobicity (lotus leaf) presented in chapter 4. Thus, this surface can be denoted as superhydrophobic:  $\theta_{\text{aca}} > 150^\circ$ , a small CA hysteresis of around  $30^\circ$  and drops roll-off a minimal tilted

surfaces. In contrast, sample Z3 is only hydrophobic, because of the high CA hysteresis and drops only slide off at tilt angles around 40°. The observed wetting properties of sample F2 could not be categorized as hydrophobic or superhydrophobic up until now: The observed CA hysteresis and tilt base angle are significantly higher compared to the values of sample F1. In addition, the drop movement on the tilted surface cannot be clearly classified as roll-off or slide-off behavior.

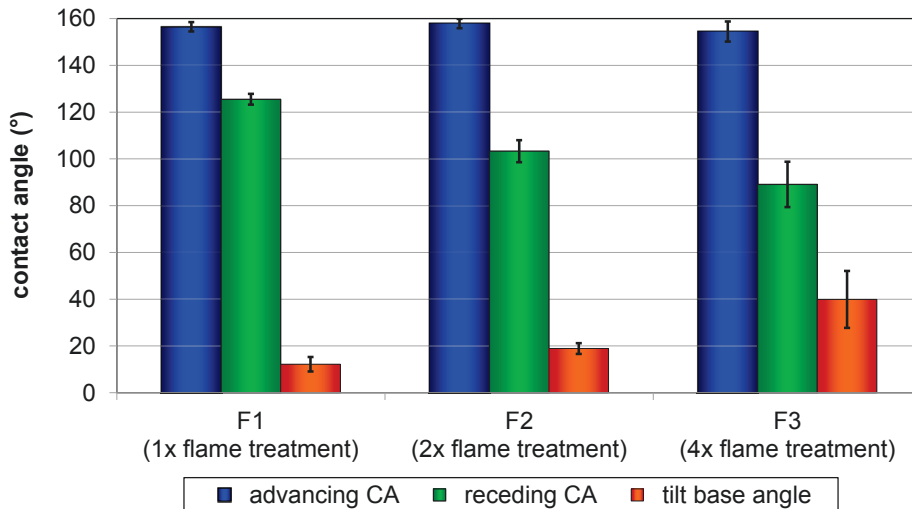


Fig. 6.3: Advancing CA, receding CA and tilt base angle of hydrophobic ZnO coatings.

By comparing the observed results of sample F2 with published natural examples it becomes apparent that the rose petal shows similar wetting properties. Some publications [10, 152, 153] report on superhydrophobicity with high adhesion, which Wang et al. [154] and Feng et al. [155] refer to as the “petal effect”: In contrast to the “lotus effect” or superhydrophobicity with low adhesion, water drops stick on the tilted surface of a rose petal.

The wetting behavior of sample Z2 and the results of the literature research lead to the conclusion that the tilt base angle method, where water drops are carefully deposited on the surface and the surface is slowly tilted afterwards, is often not practical. In nature, raindrops fall with a certain velocity onto tilted surfaces and then bounce off. This can be observed on the rose petal, for instance.

Consequently, on surfaces with large  $\theta_{aca}$  and comparably large CA hysteresis, where drops tend to slide off or stick rather than to roll off, it is more meaningful to study the “dynamic” wetting behavior. Thus, an additional testing method to take this into account was developed within this thesis. The experiment is based on the natural behavior of raindrops falling onto tilted plant leaves at a certain speed. This means, if a drop possesses kinetic energy, it can overcome the sticking forces [156].

The procedure of the developed bouncing experiment is as follows [17, 75, 150]:

A drop with a volume of approximately 6  $\mu\text{l}$  falls from a defined height (6 mm) onto a tilted surface ( $\leq 40^\circ$ ). The corresponding bounce-off angle  $\alpha_{\text{bo}}$  is measured as the minimum tilt angle at which the drop jumps off the surface without residue.

In Fig. 6.4 an example of the bounce-off behavior is given by means of sample F2: A water drop falls from a defined height (left) and bounces off a  $20^\circ$  tilted surfaces (center) without residue (right).

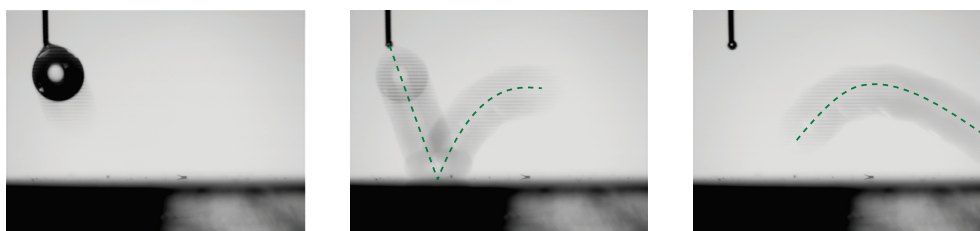


Fig. 6.4: Bouncing experiment: A water drop (left) falls onto a  $20^\circ$  tilted surface (center) and bounces off without residues (right).

For all of the following presentations of bouncing experiment results, the single images of the bounce-off behavior are merged to create one image.

It is important to note that using the bounce-off angle as practical criterion in addition to  $\Theta_{\text{aca}}$ ,  $\Theta_{\text{rca}}$ , and  $\alpha$  to describe hydrophobicity is a first approach so far. With respect to the natural behavior that the rain can clearly differ in its appearance, systematic test series of the bounce-off behavior using varying parameters (drop velocity, drop volume, surface tilt angle, etc.) are necessary. A first research of published investigations yielded that papers address either the effect of different environmental conditions on the bounce-off behavior (e.g. drop velocity, drop diameter, and liquid viscosity) [157, 158] or describe in detail the single phases of the drop impact [147, 154, 159]. For example, Rioboo et al. [160] divided the impact of drops onto dry solid surfaces into four distinct phases: the kinematic phase, the spreading phase, the relaxation phase, and the wetting/equilibrium phase. In addition, basic theoretical assumptions of bouncing drops are summarized in [161]. However, a systematic study of all these aspects goes beyond the scope of this thesis.

### 6.1.3 Novel criteria for superhydrophobicity

After the wetting analysis methods necessary for a comprehensive determination of the hydrophobicity were developed and applied to the first samples of hydrophobic surfaces, robust criteria for superhydrophobicity bridging the gap between theory and practice were acquired within this thesis. The achievement of these novel criteria is based on the findings presented in the previous sections.

Initially, superhydrophobicity was characterized by rather undefined statements based on the result of a first literature review during the “Diplomarbeit thesis” [31]. In the year 2009, Flemming et al. defined superhydrophobicity, which was still called ultrahydrophobicity, using theoretical criteria [27]:

- High water CA  $\theta_{aca} \gtrsim 150^\circ$ ,
- low CA hysteresis, and
- low tilt base angle  $\alpha \lesssim 20^\circ$ .

This definition was then carried into further publications [17, 75, 150] as well as into this thesis with the term “superhydrophobic according to strict theoretical criteria”.

To comply with all criteria, wetting has to occur necessarily in the heterogeneous wetting state [136], where air cavities are entrapped between the liquid and the solid. Essential for this wetting state is a surface with sufficiently high aspect ratios of the roughness structures. This, in turn, is important for the self-cleaning effect based on superhydrophobicity (cf. section 6.1.1) [17]. A prominent natural example for a surface with superhydrophobic properties according to strict theoretical criteria is the lotus leaf (Fig. 6.5).

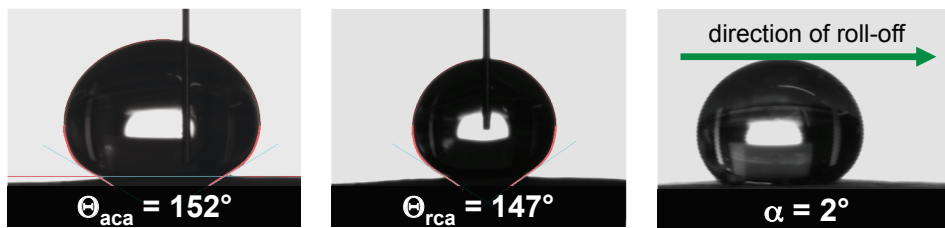


Fig. 6.5: Lotus leaf with superhydrophobic wetting properties according to strict theoretical criteria: Left: Advancing CA. Center: Receding CA. Right: Tilt base angle.

Systematic investigations of sample series with different surface roughness and hydrophobicity revealed that these strict theoretical criteria are not always feasible for practical applications. An example was given in section 6.1.2 and Fig. 6.3, respectively: Sample Z1 clearly meets the strict theoretical criteria and hence exhibits superhydrophobic properties according to these criteria. In contrast, sample F2 can be denoted as a kind of borderline case:  $\theta_{aca} = 158^\circ$  fulfill the first criterion, but the CA hysteresis and  $\alpha$  are slightly larger than the thresholds of the criteria. Similar wetting properties were found for the rose petal, which exhibits a  $\alpha$  slightly higher than  $20^\circ$ .

These observations lead to the conclusion that additional considerations focusing on functional aspects are required. For this reason, the bouncing experiment was introduced. The following practical and less stringent criteria of superhydrophobicity were retrieved from this bouncing experiment [17, 75, 150]:

- High water CA  $\theta_{aca} \gtrsim 140^\circ$ , and
- low bounce-off angle  $\alpha_{bo} \leq 40^\circ$ .

Surfaces that reveal these wetting properties are denoted as “superhydrophobic according to practical aspects”. This kind of definition is sufficient for a wide range of practical applications.

Following this new definition, sample F2 with  $\theta_{aca} = 158^\circ$  (Fig. 6.3) and  $\alpha_{bo} = 20^\circ$  (Fig. 6.4) as well as the rose petal (Fig. 6.6) can be denoted as superhydrophobic according to practical aspects.

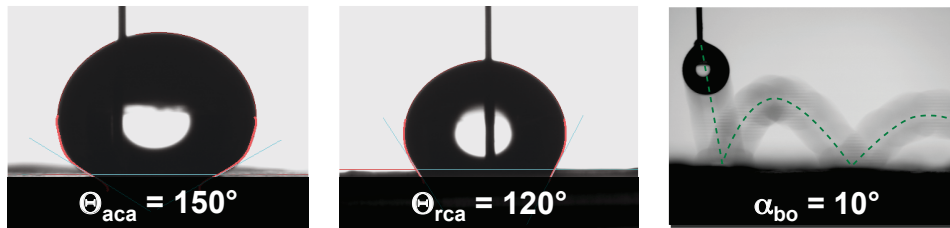


Fig. 6.6: Rose petal with superhydrophobic wetting properties according to practical criteria: Left: Advancing CA. Center: Receding CA. Right: Bounce-off angle.

If a functional hydrophobic surface meets either the “practical” or the “theoretical” criteria, the surface is called superhydrophobic with the corresponding additional specifications. Thus, clear and unambiguous information is provided to the user [150].

For the sake of simplicity, superhydrophobic or “SH” means “superhydrophobic according to strict theoretical criteria”, otherwise it is denoted as “SH<sub>pr</sub>” for “superhydrophobic according to practical aspects”.

## 6.2 Hydrophilic surfaces

Analogous to hydrophobic surfaces, the achievements of the wetting analysis methods to characterize hydrophilicity including the fogging behavior are presented in this section. For the development of the methods, no previous research was available. Hydrophilic surfaces were systematically investigated for the first time in the frame of this thesis.

First, the cause and effect of optical surfaces fogging up as well as published definitions of anti-fog properties are summarized. After that, the developed wetting

analysis methods are presented. Finally, a first approach for the definition of anti-fog criteria is introduced.

### 6.2.1 Anti-fog: Common definitions

As for the term superhydrophobicity, although the term anti-fog is often used for marketing commercial products, there are a large number of different definitions. Most of these published investigations are simultaneously related to strong hydrophilic wetting, which is normally denoted as superhydrophilicity [14].

Based on the publication in [110, 162] the fogging process can be described as follows: When air is supersaturated with dispersed water particles, the temperature of the surface is below the dew point of water vapor, and temporary fluctuations in humidity, temperature, or convection occur, then water vapor condenses into liquid water on the surface. The phenomenology of this fogging depends on the chemical and physical nature of the surface [163]. With respect to optical surfaces, two extreme regimes can be identified [13, 14, 16, 112, 163, 164]:

- Water vapor condenses in the form of small droplets with high  $\theta_{ap}$  on the solid phase. This leads to light scattering and reduced transmittance of optical surfaces.
- Water vapor completely spreads and a continuous liquid film is formed on the solid phase. This prevents light scattering from droplets and improves the transmittance of optical surface compared to the first case.

This implies that anti-fog behavior is based on excellent hydrophilic wettability. Analogous to the term superhydrophobicity, the so-called superhydrophilicity is defined differently in various international publications. Most often a  $\theta_{ap} \leq 5^\circ$  within a timespan of 5 s is used as criterion [15, 49, 108, 113]. In addition, a  $\theta_{ap} = 0^\circ$  is theoretically possible, but in most cases this behavior is not long-term stable because of the attraction of surrounding particles [13].

To achieve extreme hydrophilicity and hence anti-fog properties, a specific surface roughness as well as a certain porosity are required. A wicking effect occurs, when liquid penetrates into the surface roughness and porosity (cf. section 4.2). This results, among other things, in an enhancement of the hydrophilicity [165].

### 6.2.2 Comprehensive wetting analysis methods

The wetting analysis through the desirable  $\theta_{aca}$  and  $\theta_{rca}$  measurements is not applicable for every wetting situation. This method is most qualified for hydrophobic surfaces. Nevertheless, moderate hydrophilic surfaces can also be characterized in

this way. Though, a first investigation of surfaces with  $\theta_{ap} \lesssim 20^\circ$  showed that the determination of  $\theta_{aca}$  and  $\theta_{rca}$  becomes complicated, up to non-evaluable results for extreme hydrophilicity. The reason for the failure is measurement uncertainty because of decreasing contrast between the drop, sample surface, and background with decreasing CA, as well as a vanishing  $\theta_{rca}$ . Thus, another method to quantify the CA behavior of hydrophilic surfaces has to be acquired.

Instead of the  $\theta_{aca}$  and  $\theta_{rca}$  measurements,  $\theta_{ap}$  with a defined volume was determined as a function of the wetting time  $t_w$  [17]. This method is conforming to the wetting analysis methods of international publications which also deal with hydrophilic wetting properties [15, 108, 111, 166, 167].

For the characterization of hydrophilic samples, a liquid drop with a volume of  $1.5 \mu\text{l}$  is deposited onto the solid surface and the drop shape is recorded as a function of  $t_w$  beginning with the first moment of contact between the liquid drop and the solid surface. The period of  $t_w$  depends on the specific hydrophilic wetting system. That means, the CA behavior will be observed until the wetting system reaches its equilibrium and hence a near-constant  $\theta_{ap}$  of the drop contour. Analogous to hydrophobic surfaces, the drop shape data is then analyzed for  $\theta_{ap}$ . Fig. 6.7 shows a typical temporal trend of  $\theta_{ap}$  for a hydrophilic wetting system.

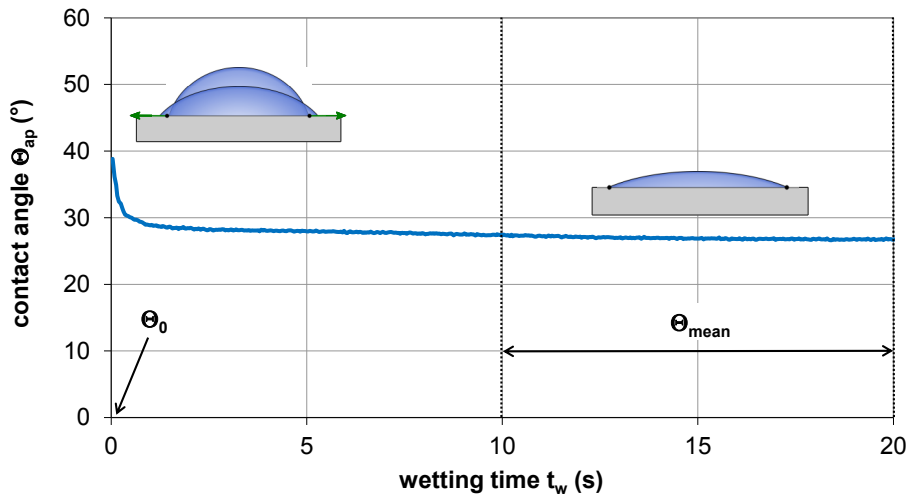


Fig. 6.7: Example for apparent CA as a function of wetting time.

The figure illustrates that the drop spreading on the investigated hydrophilic surfaces is characterized by different wetting phases:

- First phase (beginning with the first contact): Sharp decrease of  $\theta_{ap}$ .
- Mid-phase: Weak and sustained decrease of  $\theta_{ap}$ .
- Final phase: Achieving a stable  $\theta_{ap}$ .



As a direct consequence of this drop spreading behavior, two typical CA can be defined for the investigation during this work:

- $\theta_0$  is  $\theta_{ap}$  at  $t_w = 0$  s,
- $\theta_{mean}$  is the averaged  $\theta_{ap}$  between  $t_w = 10$  s ... 20 s.

Furthermore, the dynamics of this hydrophilic CA behavior can be modeled through two different theoretical approaches [168-170]: molecular kinetic and hydrodynamic theory. For the aim of this work, it was not necessary to describe the relaxation of the  $\theta_{ap}$  through such an approach. Nevertheless, first attempts are made to fit a simple power law based on Tanner's law [171] to the spreading behavior of the examined hydrophilic samples, where  $t$  is the wetting time and  $K$  and  $m$  are variable parameters:

$$\theta_{ap} \sim K \cdot t^m . \quad (6.1)$$

Besides the practical utilization of the CA measurement, another important item regarding the adaption of the wetting analysis for hydrophilic wettability includes an optimization of the drop shape analysis. Therefore, an application note from DataPhysics [172] was consulted, which reports on drop shape analysis by means of the four contour analysis methods circle fitting, ellipse fitting, Laplace-Young fitting, and tangent leaning. DataPhysics determined the  $\theta_{ap}$  and its deviation to the ideal drop shape of different CA standards. It turned out that the Laplace-Young fitting is the most exact method but inappropriate for the analysis of recorded video data because of the large memory capacity requirements. For wetting systems with  $\theta_{ap} < 30^\circ$ , the circle fitting exhibits the next best results. Based on these information, a series of experiments with hydrophilic coatings was carried out to determine the best fitting method for the wetting system examined in this work. For the evaluation of the suitability of the contour analysis methods, the Laplace-Young fitting is used as the reference method. The  $\theta_{ap}$  of surfaces with different hydrophilic wettability were observed and analyzed with circle fitting, ellipse fitting, and tangent leaning. This evaluation led to the conclusion that for the hydrophilic wetting system investigated in this thesis, the  $\theta_{ap}$  calculated by ellipse fitting shows the smallest deviations from the reference CA determined by the Laplace-Young fitting. For that reason, the ellipse fitting is used to analyze the drop shapes in the case of hydrophilic surfaces.

Another problem of extremely hydrophilic surfaces with  $\theta_{ap}$  virtually zero is that the drop shape is just inadequately or not evaluable at all because of the low contrast between the background, liquid drop, and solid surface. The critical minimal evaluable CA was determined in the context of [173]. Depending on the wetting

system and thus on the contrast, the critical minimal evaluable CA varies between  $3^\circ$  and  $6^\circ$ .

The fabrication and investigation of hydrophilic optical surfaces aims at a realization of anti-fog properties. Therefore, a novel method was acquired within this work to quantify the fogging behavior of hydrophilic surfaces, meaning in form and in time-dependent course. Comparable procedures can be found in the literature [16, 110, 112, 113, 164, 174], however, only with a qualitative assessment of the observed results.

The measurement setup of the fogging experiment consists of a beaker filled with distilled water placed onto a hotplate, a sample holder lying on top of the beaker, and a thermometer to control the water temperature. The distance between the water surface and the sample surface is 80 mm. Next to this setup a reflected-light microscope from Leica is located to observe and capture the fogging behavior. A 5x objective with a field of view of  $1.7 \times 1.4 \text{ mm}^2$  is used. Fig. 6.8 shows the entire setup.

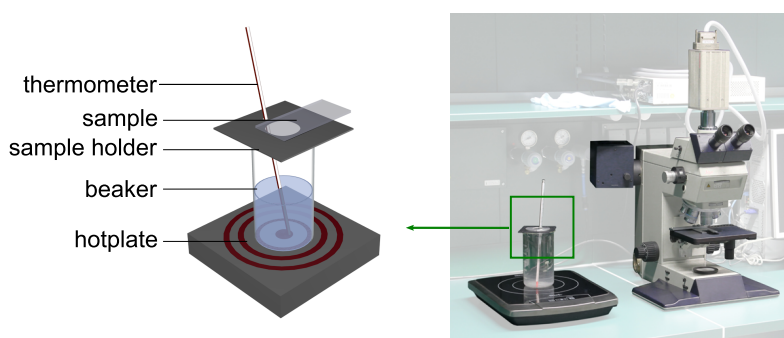


Fig. 6.8: Schematic illustration of the evaporation setup (left) and photograph of the fogging experiment setup (right).

The fogging experiment is carried out according to the listed procedure:

- Heat up water to  $50^\circ\text{C} \pm 3^\circ\text{C}$ .
- Expose the sample to water vapor for 30 s.
- Move the sample from the evaporation setup to the microscope stage (approximately 5 s).
- Record the fogging process of the sample using the microscope.

The fogging behavior is evaluated afterwards for drop shape and chronological development:

- $N_{\text{drops}}$ : Number of visible fogging droplets in the field of view of  $1.7 \times 1.4 \text{ mm}^2$  after 10 s.
- $t_{\text{fog}}$ : Fogging time at which the fog has been completely dissolved in the field of view of  $1.7 \times 1.4 \text{ mm}^2$  (uncertainty estimated to be  $\pm 3 \text{ s}$ ).

During previous investigations, a fogging time of 10 s to count  $N_{\text{drops}}$  turned out to be most suitable, because the assessment by means of droplet shape and number is best. At a later time, depending on the wetting behavior of the specific sample surface, the condensed water on the sample might have been mostly dissolved and an analysis of the fogging behavior would be more difficult.

In addition to the characterization of the fogging behavior, the presented setup is also suited for an identification of inhomogeneities and defects of hydrophilic as well as hydrophobic optical coatings.

### 6.2.3 Novel criteria for anti-fog surfaces

A literature research concerning the definition of anti-fog behavior (c.f. section 6.2.1) and findings during the development of the wetting analysis methods (c.f. section 6.2.2) have directly influenced the achievement of the wetting criteria for anti-fog based on hydrophilicity.

To denote a functional surface as “anti-fogging”, the following two criteria have to be met [17, 75]:

- Low water CA  $\theta_{\text{mean}} \lesssim 10^\circ$ , and
- the condensing water wets the surface completely and instantaneously.

The images left and center in Fig. 6.9 show an example of a sol-gel coating, which fulfills both criteria. Thus, this surface can be denoted as hydrophilic with anti-fog properties. By way of comparison, the fogging behavior of a pure glass substrate, which exhibits a huge number of fogging droplets, is shown in Fig. 6.9 right.

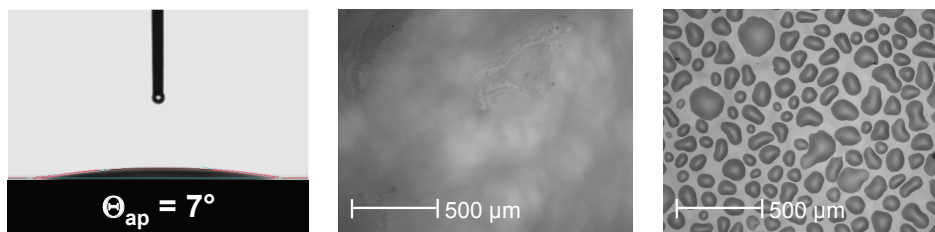


Fig. 6.9: Hydrophilic nanorough  $\text{SiO}_2$  coating. Left: Apparent CA at a wetting time of 2.5 s. Center: Fogging experiment. Right: Fogging experiment of hydrophilic uncoated glass substrate.

## 6.3 Summary

First of all, the measurements of the wetting analysis methods are performed under constant measurement conditions. The measurement positions have to be free of prior wetting with the test liquid or another liquid as well as without defects or inhomogeneities. For the fogging experiment, the ambient temperature and the humidity are constant. Otherwise, the wetting results will be affected [15, 147].

In summary, comprehensive wetting analysis methods to characterize the hydrophobic as well as hydrophilic wetting properties were acquired within the framework of this thesis. For this purpose, existing methods such as  $\theta_{aca}$ ,  $\theta_{rca}$ , and  $\alpha$  measurements were developed further with respect to the specific wetting systems investigated in this work. Furthermore, novel methods referring to practical aspects such as the bouncing experiment and the fogging experiment were introduced.

Based on these comprehensive wetting analysis methods, novel criteria for extreme wetting behavior were defined. The term superhydrophobicity was distinguished into strict theoretical and practical criteria. In the case of the term anti-fog, a first definition with respect to functional applications was presented.

In the following chapter, the entire wetting methodology is applied to different sample series with the focus on investigating the correlation between structural properties and wettability. At the same time, the applicability of the methodology will be examined.

## 7 Results and discussion

The combination and subsequent utilization of the roughness and wetting analysis methods and results described in chapter 3, 4, and 6 support the entire chain of a technological process for the fabrication of nano- and microstructured surfaces with superhydrophobic properties in a twofold way (Fig. 7.1): First, it defines the appropriate roughness in the design process in contrast to conventional trial-and-error approaches. Second, the control and the characterization of the fabricated roughness structures and the resulting wetting properties can be independently analyzed from the hydrophobic material properties [17].

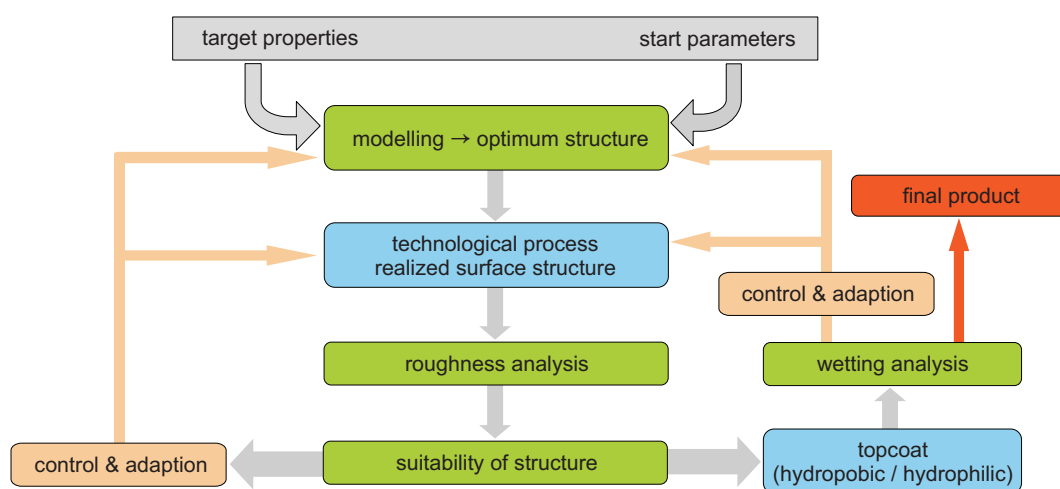


Fig. 7.1: Measurement and analysis methodology for nano- and microrough surfaces.

In this chapter, the presented measurement and analysis methodology is applied to various samples consisting of different surface materials, roughness structures, and chemical properties.

For hydrophobic wetting systems, the investigations of the following topics were of interest:

- Suitability tests of the presented methodology with respect to:
  - Applicability of the characterization methods (e.g. bounce-off experiments) as well as of the novel criteria for superhydrophobicity, and
  - application range for specific surfaces structures (nanorough optical coatings and microrough engineering surfaces).
- Support of process optimization for the fabrication of nanorough optical coatings regarding their structure properties to achieve superhydrophobicity which, at the same time, fulfill the requirements for low scatter losses.
- Achievement of reliable  $\kappa_B$  thresholds with respect to the two criteria of superhydrophobicity (SH and SH<sub>pr</sub>; see section 6).

For the investigation of hydrophilic surfaces, the main research focus was to prove the possibility for extending the  $\kappa_B$  approach to hydrophilic wetting systems. Therefore, studies about the correlation between  $\kappa_B$  and roughness-induced hydrophilicity were performed. In theory, the method should work in a similar way for the hydrophilic as well as for the hydrophobic domain, but a possible influence of porosity was not yet considered. For this purpose, first systematical investigations of the relation between the process parameters, structural properties, and wettability according to the process chain shown in Fig. 7.1 was carried out. The structural properties include not only surface roughness but also porosity and layer thickness.

The results and discussion of these studies are presented in the following sections.

### 7.1 Validation of the methodology for superhydrophobicity

The validity of the entire measurement and analysis methodology including the novel criteria for superhydrophobicity, which were introduced in chapter 6, are verified for  $\text{Al}_2\text{O}_3$  sol-gel coatings with a hydrophobic top layer based on their roughness and wetting characteristics. Besides the investigation of the correlation between roughness and wettability, the scatter losses of these sol-gel coatings fabricated under different process conditions are also determined.

The nanostructures of the  $\text{Al}_2\text{O}_3$  sol-gel coatings are shown in Fig. 7.2 and the results of the subsequent PSD analysis is presented in Fig. 7.3 together with the PSD of an uncoated glass substrate. The  $\kappa_B$  values calculated from the PSD functions for each decade between a spatial frequency of  $1 \mu\text{m}^{-1}$  and  $1000 \mu\text{m}^{-1}$  are listed in Tab. 7.1.

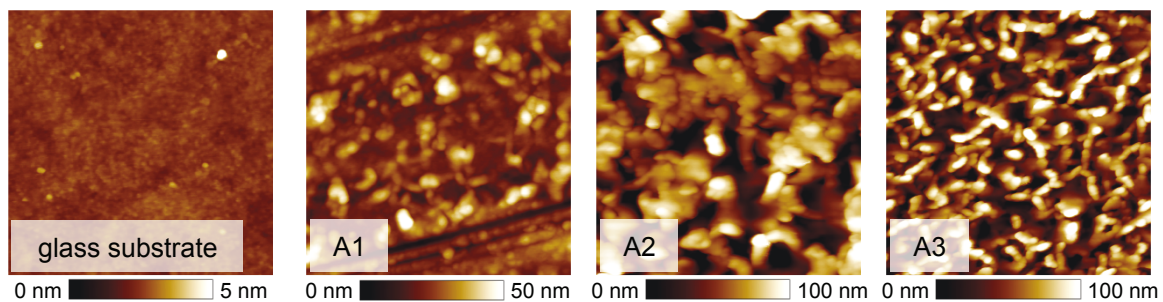


Fig. 7.2: AFM topography images of an uncoated glass substrate ( $\sigma = 0.23 \text{ nm}$ ) and  $\text{Al}_2\text{O}_3$  sol-gel coatings (Sample A1:  $\sigma = 6.5 \text{ nm}$ ; sample A2:  $\sigma = 24.0 \text{ nm}$ ; sample A3:  $\sigma = 24.3 \text{ nm}$ ). Scan area:  $1 \times 1 \mu\text{m}^2$ .

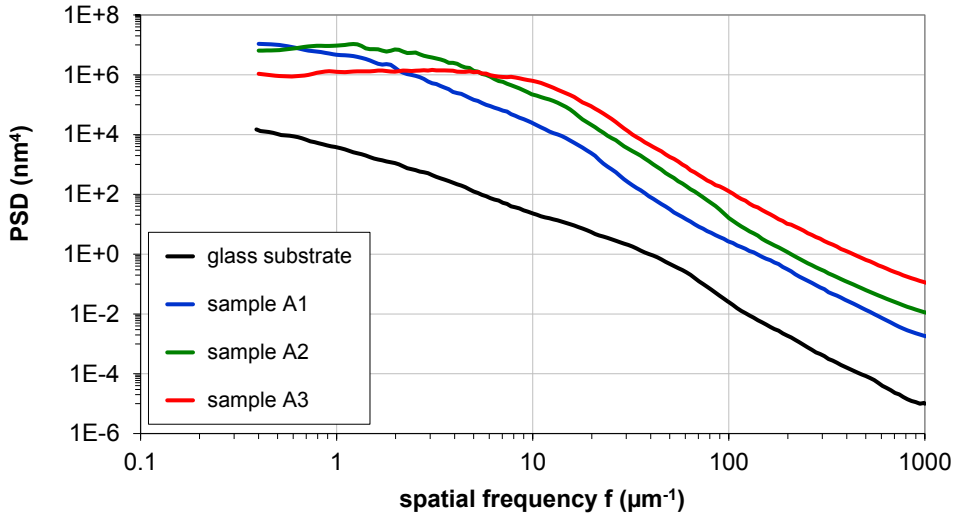


Fig. 7.3: PSD functions of uncoated glass substrate and  $\text{Al}_2\text{O}_3$  sol-gel coatings.

Tab. 7.1: Wetting parameters of  $\text{Al}_2\text{O}_3$  sol-gel coatings.

sample	$\kappa_B$ in different spatial bandwidths			
	$(1 - 10) \mu\text{m}^{-1}$	$(10 - 100) \mu\text{m}^{-1}$	$(100 - 1000) \mu\text{m}^{-1}$	$(1 - 1000) \mu\text{m}^{-1}$
<b>A1</b>	0.02	0.04	0.06	<b>0.12</b>
<b>A2</b>	0.05	0.12	0.13	<b>0.30</b>
<b>A3</b>	0.05	0.24	0.40	<b>0.69</b>

The AFM images and PSD functions reveal three types of  $\text{Al}_2\text{O}_3$  coatings which show different surface characteristics. It is important to note that sample A2 and sample A3 exhibit almost the same rms roughness values because of the comparable vertical dimensions of their nanostructures. However, the PSD functions and subsequent  $\kappa_B$  calculation reveal different roughness characteristics: Sample A2 exhibits a  $\kappa_B$  value of 0.30. Sample A3 with a  $\kappa_B$  value of 0.69 clearly exceeds the threshold which was introduced in chapter 4. For this sample, the potential for superhydrophobicity is stated.

These results prove that simple roughness parameters like rms roughness are not suitable to assess the roughness characteristic with respect to the wettability. A more complex method based on PSD analysis is necessary which considers the vertical as well as the lateral dimension of the roughness components.

The results of the wetting analysis for the hydrophobic  $\text{Al}_2\text{O}_3$  coatings are summarized in Fig. 7.4.

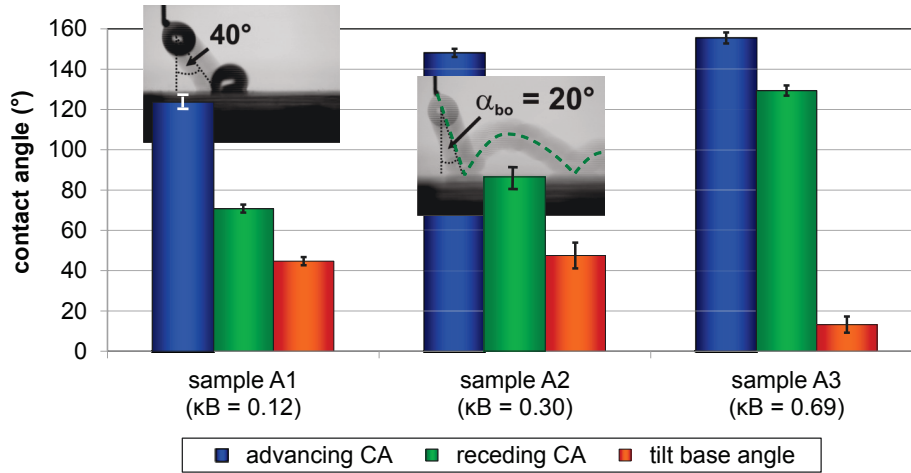


Fig. 7.4: Advancing CA, receding CA, and tilt base angle of  $\text{Al}_2\text{O}_3$  sol-gel coatings. The embedded pictures show the bounce-off behavior of sample A1 and A2.

For sample A3, the prediction of superhydrophobicity was confirmed by the measured high advancing and receding CA of  $\theta_{aca} = 156^\circ$  and  $\theta_{rca} = 129^\circ$  (i.e. CA hysteresis as low as  $30^\circ$ ). Also, only a small tilt base angle of  $\alpha = 13^\circ$  was necessary to observe a roll-off behavior of water drops from the sample surface. The self-cleaning effect of this sample, resulting from the heterogeneous wetting state, is demonstrated in Fig. 7.5: A spherical water drop rolls off the surface and removes artificial contaminants (graphite powder) on its track.



Fig. 7.5: Self-cleaning effect on  $\text{Al}_2\text{O}_3$  sol-gel coating (sample A3) with superhydrophobic properties according to strict theoretical criteria.

For sample A2, a promising  $\theta_{aca}$  of  $148^\circ$  was obtained, but on the tilted surface the water drops only slide of the surface for  $\alpha = 48^\circ$ . A roll-off movement was not observed, owing to the high CA hysteresis of  $62^\circ$ . Hence, according to the novel criteria introduced in chapter 6, sample A2 is termed as superhydrophobic according to practical aspects ( $\text{SH}_{pr}$ ), because of the low bounce-off angle ( $\alpha_{bo} = 20^\circ$ ) visible in Fig. 7.4 as embedded picture. As sample A3 with SH wetting properties, sample A2 reveals a self-cleaning effect as well (Fig. 7.6): Bouncing drops gradually remove artificial contaminations on their tracks. The first picture of this test shows that the graphite powder adheres at the drop surface rather than at the sample surface. The procedure of this qualitative self-cleaning experiment is described in [161].





Fig. 7.6: Self-cleaning effect on  $\text{Al}_2\text{O}_3$  sol-gel coating (sample A2) with superhydrophobic properties according to practical criteria. Left: Bounced drop covered with graphite powder. Center: Surface after two bouncing drops. Right: Surface after several bouncing drops.

The observation of the self-cleaning effect on surfaces with  $\text{SH}_{\text{pr}}$  leads to the conclusion that the more practical criteria of superhydrophobicity is also sufficient to classify a surface with respect to the desired self-cleaning effect.

The sample with the lowest  $\kappa_{\text{B}}$  value of 0.12 exhibits a quite small CA and the bouncing experiment reveals falling water drops sticking on the tilted ( $40^\circ$ ) surface (see Fig. 7.4). Thus, the wetting situation is in the homogeneous regime.

The results of the light scattering measurements at a wavelength of 532 nm are shown in Fig. 7.7.

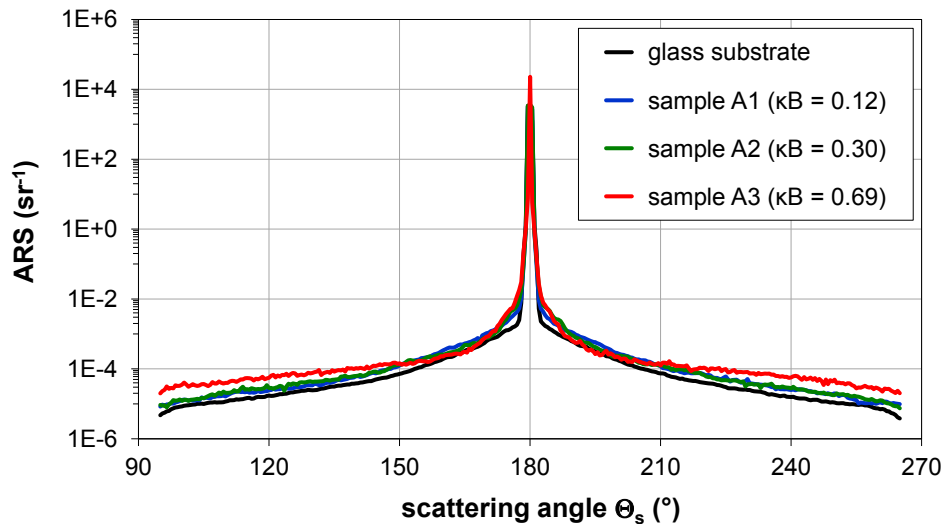


Fig. 7.7: Results of ARS measurements of uncoated glass substrate and  $\text{Al}_2\text{O}_3$  sol-gel coatings.

Even though the highest scattering signal can be observed for the superhydrophobic sample A3, its overall scatter loss remains as low as  $\text{TS}_{\text{f}} = 0.08\%$  (transmission direction) and hence well below the threshold determined by optically esthetic requirements (cf. section 3.4). By looking at the PSD functions and the  $\kappa_{\text{B}}$  values for each spatial frequency decade, it becomes apparent that the main contribution to the  $\kappa_{\text{B}}$  value and the related increased hydrophobicity mainly occurs in the high spatial

frequency range ( $f > 10 \mu\text{m}^{-1}$ ). In the visible spectral range ( $f < 2.5 \mu\text{m}^{-1}$ ), these roughness structures only lead to uncritical values for the scatter loss.

In summary, the presented results of the  $\text{Al}_2\text{O}_3$  sol-gel coatings demonstrate that the suggested wetting analysis methods including the criteria for superhydrophobicity as well as the complete methodology based on the wetting parameter  $\kappa_B$  are suitable to predict, define, and control roughness structures for optimal hydrophobic wetting behavior of nanorough surfaces.

Furthermore, the roughness and wetting properties of sample A2 lead to the conclusion that a  $\kappa_B$  threshold of 0.3 is very promising for  $\text{SH}_{\text{pr}}$ . This was confirmed by the self-cleaning effect which is comparable to the self-cleaning effect of sample A3 with SH wetting behavior. A roughness characteristic with a  $\kappa_B$  value above 0.4 is needed to achieve surfaces with SH properties. This threshold is confirmed by means of sample A3. The conclusions of the previous “Diplomarbeit thesis” [31] also indicate this threshold limit for a sputtered nanorough zirconium oxide coating: For this sample, a  $\kappa_B$  value of 0.43 and the wetting properties of  $\theta_{\text{aca}} > 150^\circ$ , small CA hysteresis, and roll-off behavior of  $\alpha < 10^\circ$  have been observed.

Finally, it was shown that superhydrophobicity combined with low scatter losses could be achieved by nanostructuring.

## 7.2 Hydrophobic and superhydrophobic nanorough optical coatings

In this section, the measurement and analysis methodology is applied to sputtered ZnO coatings to investigate the control and optimization potential for the coating process. For this purpose, promising roughness structures are defined by modeling “virtual coatings”. Afterwards, the influence of different process parameters on the ZnO layer roughness structures as well as its suitability for superhydrophobicity is studied. The resulting conclusions are then proved by means of the wetting analysis. Moreover, first investigations regarding the effect of chemical functionalization on wettability are performed. Finally, the optical properties with respect to the sample application for easy to clean gastronomic and decorating glass as well as the long-term stability of promising functional surfaces are discussed.

At the same time, the suitability of the methodology for the specific roughness characteristic is evaluated.

### 7.2.1 Roughness and wetting properties

#### *Simulation of promising roughness structures for superhydrophobicity*

For the realization of optimal hydrophobic wettability, the effect of roughness structures on the wetting parameter is simulated. The advantage of this approach is

that start parameters for a subsequent systematical improvement of the sputter process can be defined.

For the simulations, PSD functions (Fig. 7.8) which were calculated from topography data of an uncoated substrate (Fig. 7.9 left) and of a first ZnO layer (Fig. 7.9 right) are used as starting point. The intrinsic roughness of the ZnO layer can then be described by an ABC model-PSD function (cf. section 2.1).

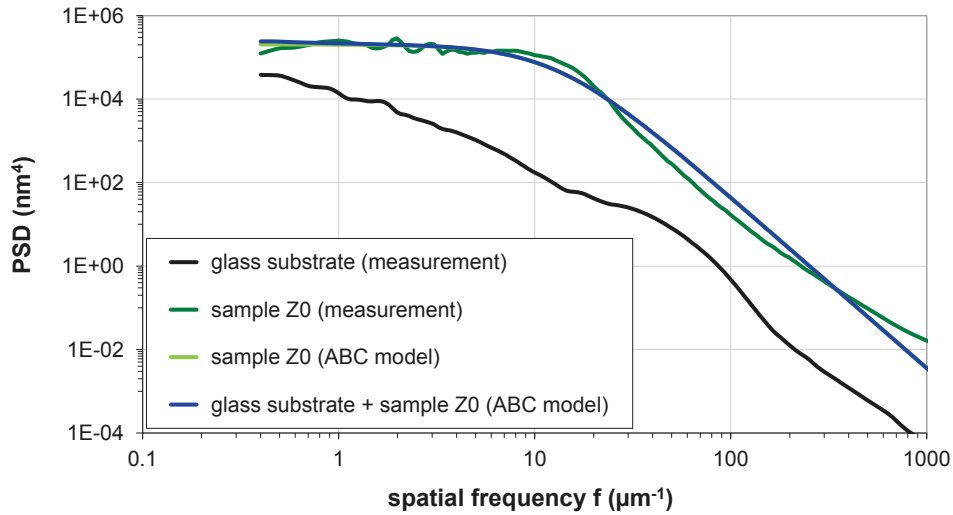


Fig. 7.8: Measurement and simulation results: PSD functions of uncoated glass substrate and ZnO layer.

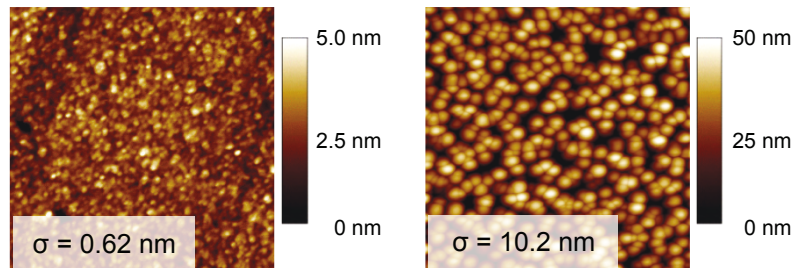


Fig. 7.9: Topography images of uncoated glass substrate (left) and ZnO layer (sample Z0) with a layer thickness of 600 nm (right). Scan area:  $1 \times 1 \mu\text{m}^2$ .

The ABC model-PSD functions (light green and blue curves) were fitted to the measured PSD function of sample Z0 (dark green curve) in such a way that the resulting wetting parameter  $\kappa_B$  is comparable to the  $\kappa_B$  value determined from the PSD function of the measured surface characteristics. This  $\kappa_B$  value is 0.29 and does not clearly exceed the threshold of 0.3 defined in the summary of the previous section.

Using the model-PSD, roughness structures with  $\kappa_B > 0.3$  were simulated. Thereby, the rms roughness  $\sigma_{ABC}$  and the correlation length  $\tau_{ABC}$  as the vertical and lateral evolution of surface morphology of sample Z0 were varied according to Eq. (2.5). In a first test,  $\sigma_{ABC}$  was steadily increased at constant  $\tau_{ABC}$  to simulate a high

aspect ratio. The corresponding model-PSDs are labeled A and B. In a second test  $\tau_{ABC}$  was also varied. The corresponding PSDs are denoted C and D. To compare the different PSDs, a similar ratio  $\sigma_{ABC}/\tau_{ABC}$  was chosen. Tab. 7.2 summarizes the used modeling parameters and Fig. 7.10 shows the corresponding PSD functions.

Tab. 7.2: Structural parameters of the model-PSD of sample Z0 and simulated model-PSD functions.

model-PSD	$\sigma_{ABC}$ (nm)	$\tau_{ABC}$ (nm)	$\sigma_{ABC} / \tau_{ABC}$
sample Z0	10	21	0.48
simulation A	14	21	0.67
simulation B	18	21	0.86
simulation C	18	27	0.67
simulation D	23	27	0.85

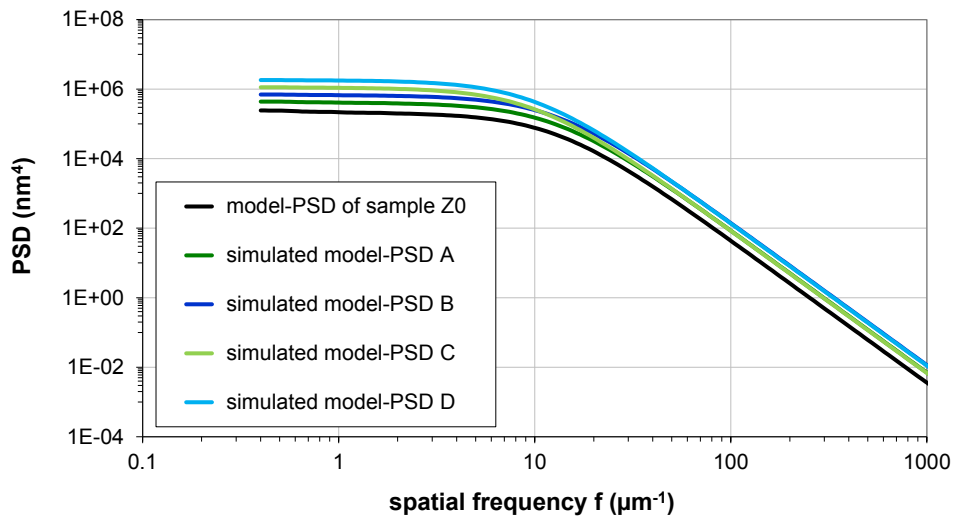


Fig. 7.10: Model-PSD of sample Z0 and simulated model-PSD functions for different aspect ratio of the surface structure.

The higher aspect ratio of the roughness structures resulting from larger  $\sigma_{ABC}$  values enables  $\kappa_B$  values of up to 0.5 (Tab. 7.3). Especially the contribution to the wetting parameter in the spatial frequency range  $f > 10 \mu\text{m}^{-1}$  is affected.

Tab. 7.3: Wetting parameters of the model-PSD of sample Z0 and simulated model-PSD functions.

model-PSD	$\kappa_B$ in different spatial bandwidths			
	$(1 - 10) \mu\text{m}^{-1}$	$(10 - 100) \mu\text{m}^{-1}$	$(100 - 1000) \mu\text{m}^{-1}$	$(1 - 1000) \mu\text{m}^{-1}$
sample Z0	0.02	0.13	0.15	<b>0.29</b>
simulation A	0.02	0.18	0.20	<b>0.40</b>
simulation B	0.03	0.23	0.26	<b>0.52</b>
simulation C	0.03	0.19	0.20	<b>0.42</b>
simulation D	0.04	0.24	0.26	<b>0.54</b>

Beside the enhancement of the roughness structures at high spatial frequencies, the increased ratio  $\sigma_{ABC}/\tau_{ABC}$  also leads to an enhancement of the PSD values in a spatial frequency range  $< 10 \mu\text{m}^{-1}$ . This corresponds to the critical spatial bandwidth for light scattering ( $f < 2.5 \mu\text{m}^{-1}$ ). The effect is smaller for the model-PSDs A and B than for the model-PSDs C and D.

For the technological sputtering process, the results of this simulation analysis imply that the vertical dimension of further ZnO roughness structures has to be increased by a factor of  $\geq 1.5$  compared to the roughness components of sample Z0. The lateral structural dimension should be similar to those of the original roughness structure of sample Z0 to minimize the effect of light scattering.

In conclusion, the simulation revealed that an optimized roughness characteristic of nanostructures is suitable to achieve superhydrophobicity.

### *ZnO coatings with varying layer thickness*

According to the previous simulation, the roughness structures of sputtered optical coatings were optimized using the  $\kappa_B$  approach in such a way that, in combination with a hydrophobic top layer, a high potential for superhydrophobic wetting properties is achieved.

In a first sample series, the layer thickness of the ZnO layers was varied continuously by choosing different parameters for the sputtering process. This enabled a systematic study of the influence of the layer thickness on the wetting-relevant surface characteristics and the related effect on the wettability.

The roughness measurement results of the ZnO coatings with varying layer thickness are presented below. Several measurements were performed in different scan areas to minimize local variations in the surface roughness. The calculated arithmetical results of at least two individual measurement positions are listed in Tab. 7.4. Selected topography images of the investigated samples can be seen in Fig. 7.11. Thereby, a scan area of  $1 \times 1 \mu\text{m}^2$  was chosen because the significant roughness structures of these coatings can be perfectly seen in this scan area.

Tab. 7.4: Rms roughness values of ZnO coatings with different layer thicknesses. Scan areas:  $0.5 \times 0.5 \mu\text{m}^2$ ,  $1 \times 1 \mu\text{m}^2$ , and  $10 \times 10 \mu\text{m}^2$ .

sample	d (nm)	$\sigma$ (nm)		
		$0.5 \times 0.5 \mu\text{m}^2$	$1 \times 1 \mu\text{m}^2$	$10 \times 10 \mu\text{m}^2$
Z1	1.3	24.1	25.7	23.1
Z2	1.8	38.5	38.5	39.8
Z3	1.8	39.9	39.9	39.2
Z4	1.8	25.0	22.5	15.3
Z5	2.0	20.1	21.9	23.7
Z6	2.4	42.3	43.3	44.2

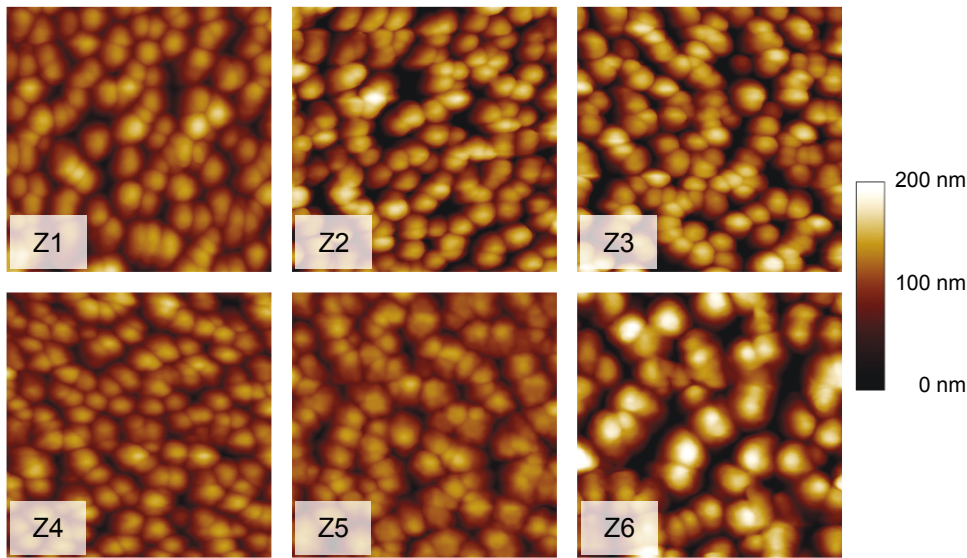


Fig. 7.11: AFM topography images of ZnO coatings with increasing layer thickness from sample Z1 to sample Z6. Scan area:  $1 \times 1 \mu\text{m}^2$ .

The investigated scan areas indicate that the vertical dimensions of the ZnO roughness components increase with the layer thickness and thus lead to an enhanced rms roughness (except for samples Z4 and Z5). Sample Z4 exhibits the same layer thickness as samples Z2 and Z3, but the surfaces roughness in the investigated scan areas is clearly smaller than for the other two surfaces. This shows that the sputtering process is not completely reproducible.

The qualitative assessment of the roughness structures shown in Fig. 7.11 leads to the conclusion that the lateral dimension of the roughness components is unaffected by the increasing layer thickness up to a layer thickness of  $2 \mu\text{m}$  (sample Z5). Only sample Z6 with a layer thickness of  $2.4 \mu\text{m}$  exhibits a significant enhancement of the roughness structures in the lateral and the vertical direction.

For all samples the PSDs were determined based on AFM measurements in the spatial frequency range between  $0.4 \mu\text{m}^{-1}$  and  $1000 \mu\text{m}^{-1}$  (Fig. 7.12). Furthermore, the  $\kappa_B$  values were calculated for different spatial frequency decades (Tab. 7.5).

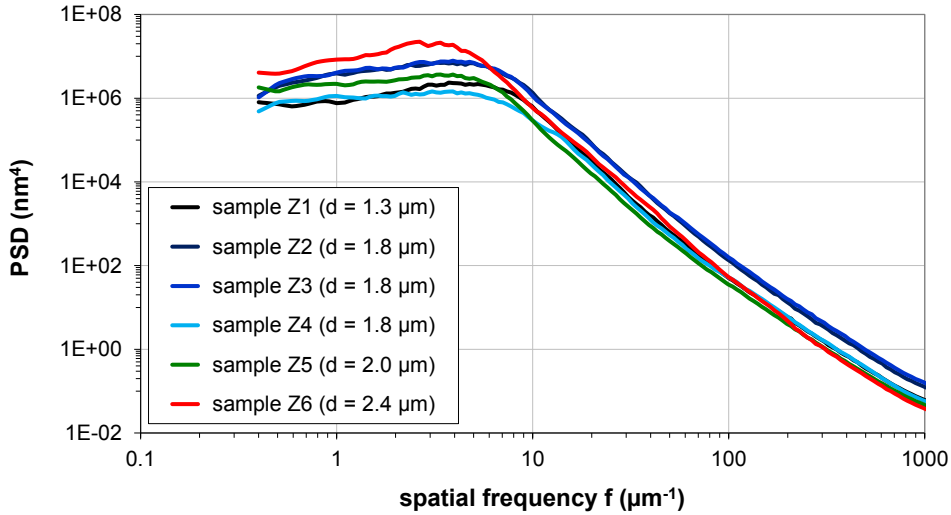


Fig. 7.12: PSD functions of ZnO coatings with varying layer thickness.

Tab. 7.5: Wetting parameters of ZnO coatings with varying layer thickness.

sample	d (nm)	$\kappa_B$ in different spatial bandwidths			
		$(1 - 10) \mu\text{m}^{-1}$	$(10 - 100) \mu\text{m}^{-1}$	$(100 - 1000) \mu\text{m}^{-1}$	$(1 - 1000) \mu\text{m}^{-1}$
<b>Z1</b>	<b>1.3</b>	0.06	0.16	0.29	<b>0.51</b>
<b>Z2</b>	<b>1.8</b>	0.09	0.25	0.44	<b>0.78</b>
<b>Z3</b>	<b>1.8</b>	0.10	0.25	0.49	<b>0.84</b>
<b>Z4</b>	<b>1.8</b>	0.04	0.14	0.30	<b>0.48</b>
<b>Z5</b>	<b>2.0</b>	0.06	0.12	0.25	<b>0.42</b>
<b>Z6</b>	<b>2.4</b>	0.10	0.18	0.25	<b>0.53</b>

The contributions to the wetting parameter below  $f = 0.4 \mu\text{m}^{-1}$  are negligible, which was proven in the “Diplomarbeit thesis” [31] and is also confirmed throughout this work since the spatial frequency range between  $1 \mu\text{m}^{-1}$  to  $10 \mu\text{m}^{-1}$  only leads to minor contribution to the  $\kappa_B$  value. The main contribution for such nanostructured surfaces can be observed in the high spatial frequency decade between  $10 \mu\text{m}^{-1}$  and  $1000 \mu\text{m}^{-1}$  as mentioned in section 3.1.

Sample Z6 with the highest layer thickness as well as the highest rms roughness in the investigated scan areas does not necessarily exhibits the largest  $\kappa_B$  value, because of the relatively large lateral dimension of the ZnO roughness components. It turned out that the  $\kappa_B$  values of all investigated ZnO coatings exceeded the threshold for superhydrophobicity and hence the potential for superhydrophobicity is stated. Furthermore, the results imply that an optimal roughness structure for superhydrophobicity can be observed for ZnO coatings with a layer thickness of  $1.8 \mu\text{m}$ . The PSD analysis including the subsequent  $\kappa_B$  calculation proves that an increased layer thickness does not necessarily lead to more promising structural properties for superhydrophobicity. The same holds true for the rms roughness: Higher rms values do not imply higher  $\kappa_B$  values.

As figure Fig. 7.13. indicates, all samples show similar  $\theta_{aca}$  above  $140^\circ$  within their standard deviation. The lowest  $\theta_{aca}$  can be found for sample Z5 which also exhibits the lowest  $\kappa_B$  value. The  $\theta_{rca}$  of the characterized ZnO coatings vary between  $30^\circ$  and  $70^\circ$  with a high CA hysteresis for all samples. Thus, SH has not been achieved. This conclusion is confirmed by the circumstance that no sample shows a roll-off behavior of spherical formed water drops. Nevertheless, for the samples with the highest  $\kappa_B$  values a bounce-off behavior of water drops falling on tilted surfaces ( $\alpha_{bo} = 30^\circ$ ) can be observed. Hence, according to the definition in chapter 6, the samples Z2, Z3, and Z6 meet the SH<sub>pr</sub> criteria.

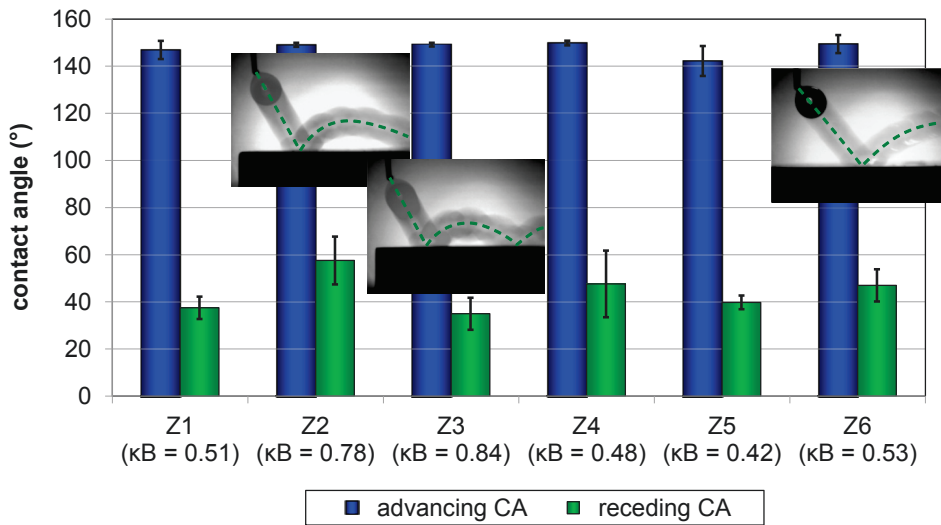


Fig. 7.13: Advancing CA, receding CA, and bounce-off behavior ( $\alpha_{bo} = 30^\circ$ ) of ZnO coatings with varying layer thickness.

### ZnO coatings fabricated by a two-step sputtering process

The used methodology was extended to further optimization of the coating process, because of the very promising results for superhydrophobicity as well as the correlation between the roughness and wetting from the layer thickness study of the ZnO layers. Thereby, the aim was to fabricate samples which exhibit roughness structures with high aspect ratio in combination with small lateral dimension in order to achieve optimal hydrophobicity and optimal optical properties. This could be realized by a two-step process with plasma treatment (cf. section 5.1). After the sample preparation, a comprehensive roughness analysis was performed. The most promising sample for potential superhydrophobicity was then overcoated with a hydrophobic top layer and afterwards analyzed with respect to surface roughness as well as for wettability.

The AFM topography image of sample Z8, depicted in Fig. 7.14, shows hexagonal roughness structures with a central peak. The non-columnar roughness structures of sample Z9 were not intended. The cause of this effect was a disturbance during the



sputtering process. The highest surface roughness (see Tab. 7.6) of the investigated samples was observed for the ZnO coating treated with an Ar-O plasma for 10 minutes (sample Z10).

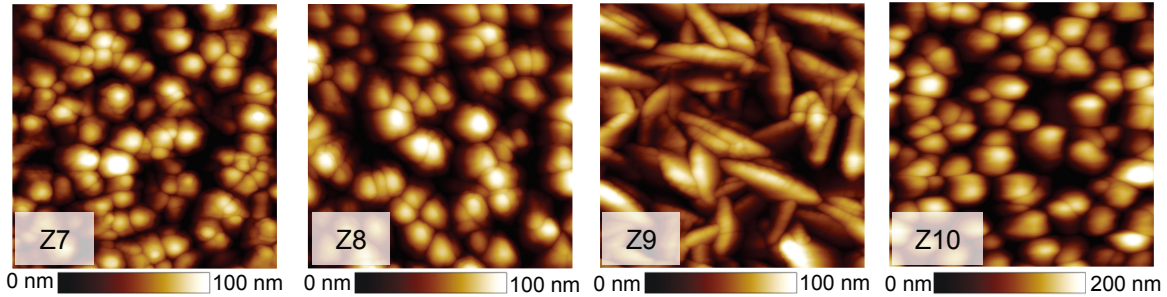


Fig. 7.14: AFM topography images of ZnO coatings fabricated by two-step process. Scan area:  $1 \times 1 \mu\text{m}^2$ .

Tab. 7.6: Rms roughness values of ZnO coatings fabricated by a two-step process. Scan areas:  $0.5 \times 0.5 \mu\text{m}^2$ ,  $1 \times 1 \mu\text{m}^2$ , and  $10 \times 10 \mu\text{m}^2$ .

sample	parameter	$\sigma$ (nm)		
		$0.5 \times 0.5 \mu\text{m}^2$	$1 \times 1 \mu\text{m}^2$	$10 \times 10 \mu\text{m}^2$
Z7	Ar (t = 5 min)	17.5	19.5	20.1
Z8	Ar (t = 10 min)	19.3	19.0	21.8
Z9	Ar + O (t = 5 min)	20.6	19.1	18.4
Z10	Ar + O (t = 10 min)	41.9	45.3	39.3

The most promising roughness structure concerning optimal hydrophobic wettability is achieved by a treatment with Ar-O plasma for 10 minutes (see Fig. 7.15 and Tab. 7.7): The corresponding sample Z10 has a  $\kappa_B$  value of 0.61 which exceeds the threshold for superhydrophobicity and hence is suitable for a functionalization with a hydrophobic top layer.

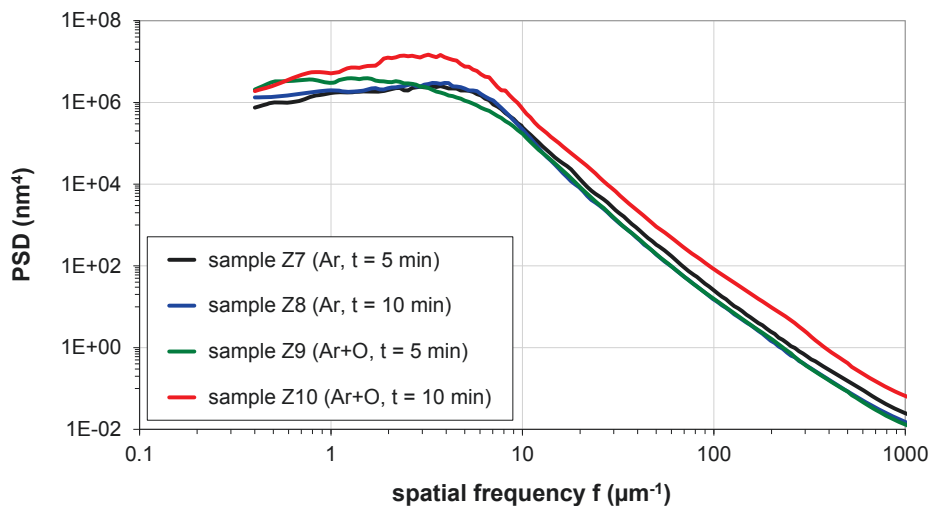


Fig. 7.15: PSD functions of ZnO coatings fabricated by a two-step process.

Tab. 7.7: Wetting parameters of ZnO coatings fabricated by a two-step process.

sample	parameter	$\kappa_B$ in different spatial bandwidths			
		$(1 - 10)$ $\mu m^{-1}$	$(10 - 100)$ $\mu m^{-1}$	$(100 - 1000)$ $\mu m^{-1}$	$(1 - 1000)$ $\mu m^{-1}$
Z7	Ar (t = 5 min)	0.05	0.11	0.19	<b>0.35</b>
Z8	Ar (t = 10 min)	0.05	0.08	0.15	<b>0.28</b>
Z9	Ar + O (t = 5 min)	0.04	0.08	0.14	<b>0.27</b>
Z10	Ar + O (t = 10 min)	0.10	0.18	0.34	<b>0.61</b>

The characterization results before and after the hydrophobic functionalization of sample Z10 are presented in the following. Furthermore, a comparison to the analysis results of the superhydrophobic sample Z6 with the lowest  $\kappa_B$  value within the first sample series are listed below.

Fig. 7.16 show that within the scan area  $10 \times 10 \mu m^2$ , the roughness structures as well as the rms roughness are very similar before and after the hydrophobic functionalization. Only in the high resolution  $1 \times 1 \mu m^2$  scan area, a slight increase of the roughness structures can be observed after the hydrophobic functionalization. The corresponding rms roughness values with and without hydrophobic topcoat are 47.2 nm and 41.2 nm, respectively.

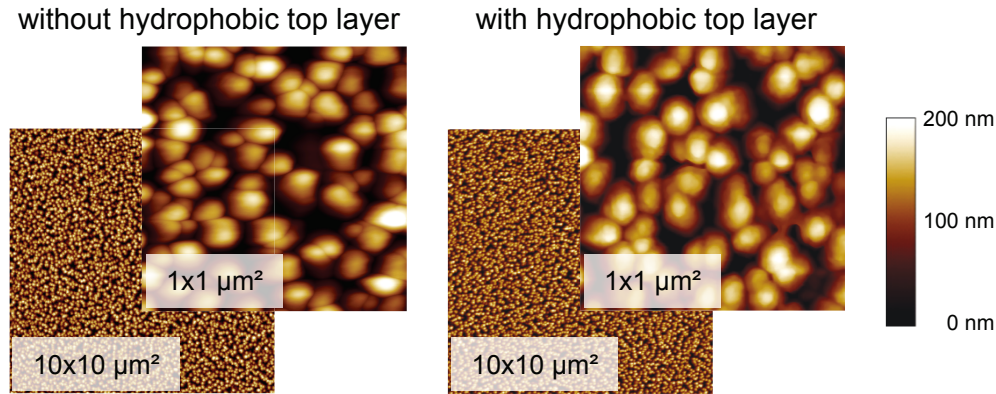


Fig. 7.16: AFM topography images in different scan areas of sample Z10 before (left) and after (right) hydrophobic functionalization.

The observed enhancement of the surface roughness for sample Z10 caused by the top layer can also be observed in the high spatial frequency range ( $f > 10 \mu m^{-1}$ ) for the PSD analysis (Fig. 7.17). In comparison to sample Z6, it can be concluded that the two-step process does not lead to the desired results: The PSD functions of sample Z6 and sample Z10 are comparable in the scatter-relevant spatial frequency range.

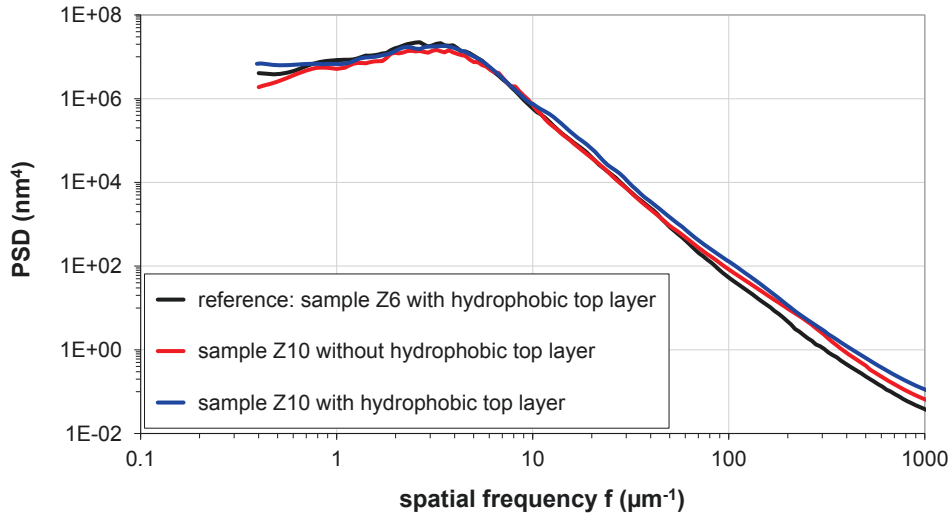


Fig. 7.17: PSD functions of sample Z6 (reference sample) as well as sample Z10 before and after hydrophobic functionalization.

Tab. 7.8: Wetting parameters of sample Z6 (reference sample) as well as sample Z10 before and after hydrophobic functionalization.

sample	top layer	$\kappa_B$ in different spatial bandwidths			
		$(1 - 10) \mu m^{-1}$	$(10 - 100) \mu m^{-1}$	$(100 - 1000) \mu m^{-1}$	$(1 - 1000) \mu m^{-1}$
Z6	with	0.10	0.18	0.25	<b>0.53</b>
Z10	without	0.10	0.18	0.34	<b>0.61</b>
Z10	with	0.10	0.22	0.41	<b>0.73</b>

Nevertheless, the wetting results shown in Fig. 7.18 reveal that sample Z10 exhibits a  $\Theta_{aca}$  of  $148^\circ$  in combination with a high CA hysteresis of  $129^\circ$ . Although, no roll-off behavior of water drops on a slightly tilted surface is observed. However, water drops jump off the surface without residue at  $\alpha_{bo} = 40^\circ$  as shown in the right image of Fig. 7.18. The prediction of superhydrophobicity was partly confirmed by the observed  $SH_{pr}$  wetting properties.



Fig. 7.18: Advancing CA (left), receding CA (center), and bounce-off angle (right) of sample Z10.

In summary, the used methodology based on the wetting parameter allowed to optimize the sputtering process in order to achieve superhydrophobic surfaces according to practical aspects. The relevant roughness characteristics for wetting were realized by nanoroughness in a high spatial frequency range. Simultaneously,

the mid spatial frequency roughness could be kept low in order to minimize the scatter loss which will be examined in section 7.2.3.

### 7.2.2 Effect of hydrophobic functionalization on wettability

Besides the influence of roughness structures, the impact of the chemical components on the wettability has to be investigated. As outlined in section 5.3, only two questions of the complex topic hydrophobic functionalization are studied in this work.

As shown in section 7.1, roughness structures with a  $\kappa_B$  value of more than 0.3 might have potential for superhydrophobicity. But the investigation of the oxidized ZnO coatings (section 7.2.1) revealed that even high  $\kappa_B$  values did not lead to superhydrophobic properties. Besides the fact that the  $\kappa_B$  threshold is only an essential criterion and not a sufficient one, a possible explanation might be the period of time (several days) between the sputtering process and the hydrophobic functionalization. This assumption was examined using a sample series of ZnO layers, which was coated with the hydrophobic top layer WR4 immediately after the sputtering process. Furthermore, the influence of the new top layer material WR4 on the roughness characteristic of the sputtered coatings was investigated.

First of all, the wettability of water on smooth glass substrates coated with the standard hydrophobic top layer PolyF1 was compared to the wettability of a smooth glass substrate coated with WR4. As presented in section 5.3, the glass substrate with WR4 exhibits a higher  $\theta_{aca}$  in combination with a lower CA hysteresis. Hence, the top layer material WR4 reveals better intrinsic wetting properties than the top layer PolyF1 independent from the sputtered roughness characteristic. This statement is non-transferable to the wetting behavior of rough surfaces, because of the complex interaction between roughness layer and top layer (cf. section 5.3).

The characterization results of a sample series consisting of small layer thicknesses of WR4 ( $\leq 10$  nm) are compared to a ZnO coating with PolyF1 as standard hydrophobic top layer. The small layer thickness was chosen in order to avoid a change of the ZnO roughness structures.

The topography images, rms values (Fig. 7.19), and PSD functions (Fig. 7.20) of the investigated samples show similar roughness structures for sample Z6 with the hydrophobic top layer PolyF1 and for the samples Z11 and Z12 with WR4 as hydrophobic functionalization. Thus, the layer material WR4 does not smooth the ZnO roughness characteristic. However, above a spatial frequency of  $100 \mu\text{m}^{-1}$  the PSDs and the  $\kappa_B$  values of both samples Z11 and Z12 are higher than the PSD and  $\kappa_B$  value of the sample Z6. One reason might be that the top layer material only

connects to the top roughness structure rather than to the entire structure. Thus, only the vertical dimension of the roughness components increases.

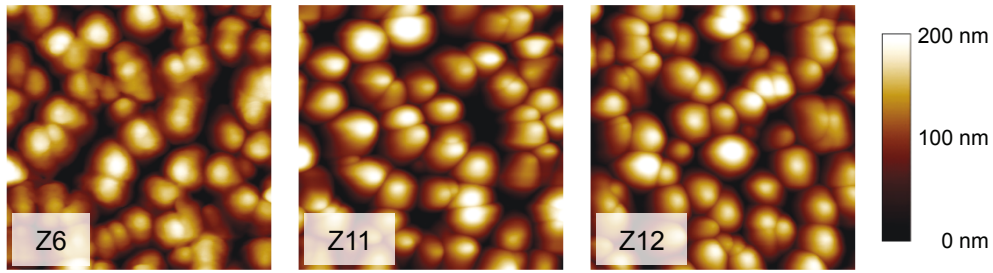


Fig. 7.19: AFM topography images of ZnO coatings with varying hydrophobic top layer (sample Z6: PolyF1,  $\sigma = 43.0$  nm; sample Z11: WR4 with  $d = 2.5$  nm,  $\sigma = 47.3$  nm; sample Z12: WR4 with  $d = 5.0$  nm,  $\sigma = 45.7$  nm). Scan area:  $1 \times 1 \mu\text{m}^2$ .

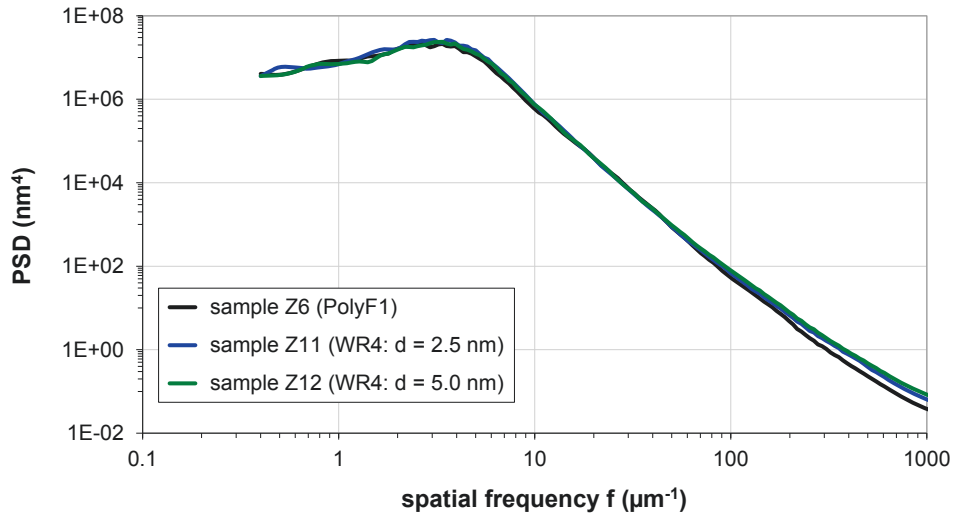


Fig. 7.20: PSD functions of ZnO coatings with varying hydrophobic top layer.

Tab. 7.9: Wetting parameters of ZnO coatings with varying hydrophobic top layer.

sample	top layer	$\kappa_B$ in different spatial bandwidths			
		$(1 - 10) \mu\text{m}^{-1}$	$(10 - 100) \mu\text{m}^{-1}$	$(100 - 1000) \mu\text{m}^{-1}$	$(1 - 1000) \mu\text{m}^{-1}$
Z6	PolyF1	0.10	0.18	0.25	<b>0.53</b>
Z11	2.5 nm WR4	0.12	0.18	0.31	<b>0.61</b>
Z12	5.0 nm WR4	0.11	0.18	0.34	<b>0.63</b>

Although both samples functionalized with WR4 exceed the threshold for superhydrophobicity, neither of them exhibits satisfying wetting properties (Fig. 7.21):  $\theta_{aca} \leq 140^\circ$ , no receding behavior of water drops and sticking water drops on the tilted surface during the bounce-off experiment.

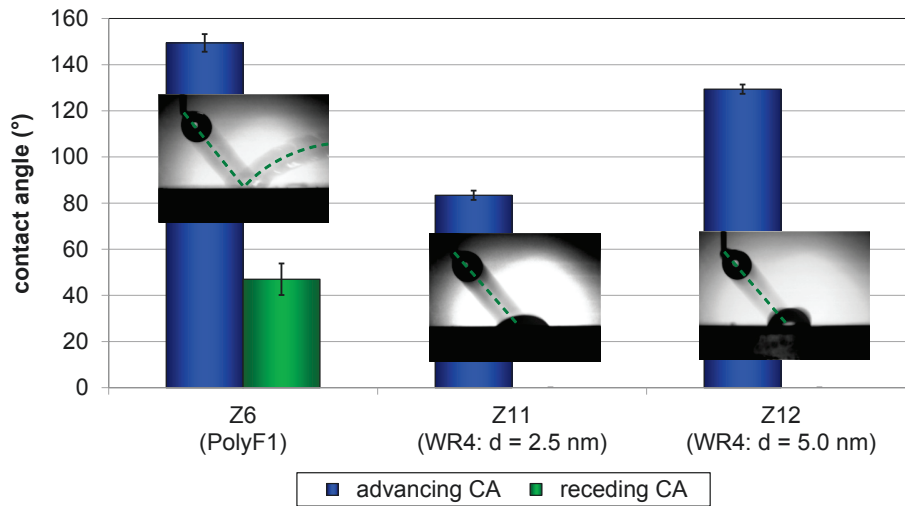


Fig. 7.21: Advancing CA, receding CA, and bounce-off behavior of the ZnO coatings with varying hydrophobic top layer. The embedded pictures show the bounce-off behavior from 40° tilted surfaces.

Because of these results, another sample series of ZnO coatings functionalized with the top layer material WR4 and higher layer thicknesses (15 nm and 20 nm) were fabricated. The roughness and wetting analysis was performed in comparison to a ZnO coating with PolyF1 (sample Z4) as top layer.

The roughness analysis results (Fig. 7.22, Fig. 7.23, and Tab. 7.10) for sample Z14 to Z16 compared to the results of sample Z4 indicate that the top layer WR4 with a higher layer thickness does not lead to a smoothing effect on the roughness structures of the ZnO coatings. The samples show small variations in the  $\kappa_B$  values, but all samples exceed the threshold. The reason for this variation is the imperfect repeatability of the sputtering process.

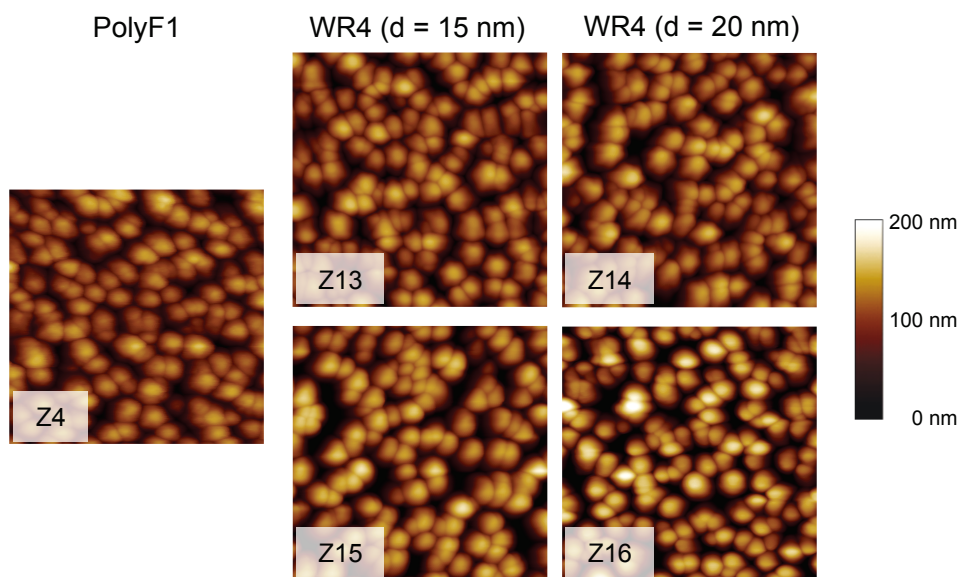


Fig. 7.22: AFM topography images of ZnO coatings with varying hydrophobic top layer (sample Z4:  $\sigma = 23.7$  nm; sample Z13:  $\sigma = 26.1$  nm; sample Z14:  $\sigma = 28.3$  nm; sample Z15:  $\sigma = 36.1$  nm; sample Z16:  $\sigma = 39.5$  nm). Scan area:  $1 \times 1 \mu\text{m}^2$ .

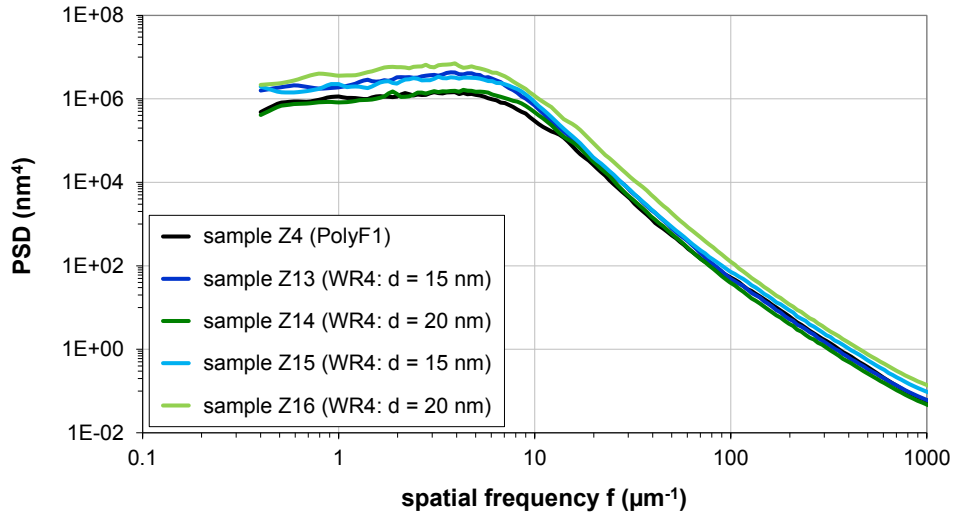


Fig. 7.23: PSD functions of ZnO coatings with varying hydrophobic top layer.

Tab. 7.10: Wetting parameters of ZnO coatings with varying hydrophobic top layer.

sample	top layer	$\kappa_B$ in different spatial bandwidths			
		$(1 - 10) \mu m^{-1}$	$(10 - 100) \mu m^{-1}$	$(100 - 1000) \mu m^{-1}$	$(1 - 1000) \mu m^{-1}$
<b>Z6</b>	<b>PolyF1</b>	0.04	0.14	0.30	<b>0.48</b>
<b>Z13</b>	<b>15 nm WR4</b>	0.07	0.17	0.29	<b>0.53</b>
<b>Z14</b>	<b>20 nm WR4</b>	0.05	0.15	0.25	<b>0.45</b>
<b>Z15</b>	<b>15 nm WR4</b>	0.07	0.18	0.36	<b>0.61</b>
<b>Z16</b>	<b>20 nm WR4</b>	0.09	0.26	0.43	<b>0.78</b>

As Fig. 7.24 indicates, all samples functionalized with the hydrophobic top layer material WR4 with a thickness of about 15 nm or 20 nm are superhydrophobic. Sample Z13 and sample Z14 are  $SH_{pr}$ , because of  $\alpha_{bo} = 40^\circ$ . Furthermore, the roughness characteristics of both samples yield a  $\kappa_B$  value which is comparable to the  $\kappa_B$  value of the “non-superhydrophobic” sample Z4 with PolyF1 as hydrophobic top layer.

In addition, two samples (Z15 and Z16) can be termed as superhydrophobic according to strict theoretical criteria:  $\Theta_{aca} > 150^\circ$  and small CA hysteresis of less than  $45^\circ$ . Thus, spherical water drops easily roll-off from minimally tilted surfaces, because of the heterogeneous wetting state.

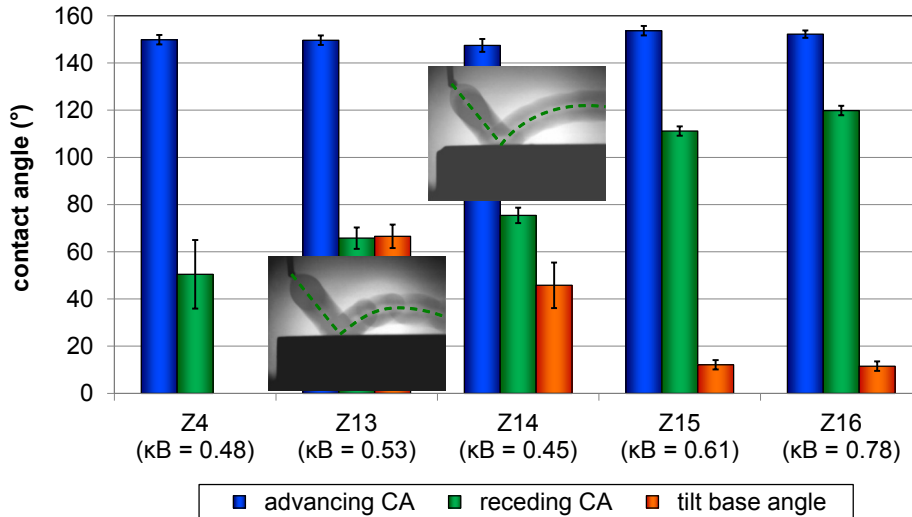


Fig. 7.24: Advancing CA, receding CA, tilt base angle, and bounce-off behavior of the ZnO coatings with varying hydrophobic top layer. The embedded pictures show the bounce-off behavior.

The study of the deposition time influence led to the result that the wetting behavior of nanorough coatings was improved by a reduction of the time period between structuring and hydrophobic functionalization. However, it was not possible to completely exclude the influence of the intrinsic chemical properties of the hydrophobic top layer material, because both materials PolyF1 and WR4 were not investigated under equal conditions (deposition process and time) in this thesis. As presented in section 5.3 for smooth glass substrates, the top layer WR4 shows better intrinsic hydrophobic properties than the top layer material PolyF1.

### 7.2.3 Optical properties and stability

Angle resolved scattering measurements were performed for selected superhydrophobic samples compared to an uncoated glass substrate at a wavelength of 532 nm. These measurements aimed at the determination of the scatter losses of the nanorough optical surfaces.

The measured ARS curves depicted in Fig. 7.25 show two distinct peaks at  $\theta_s = 0^\circ$  (reflection direction) and  $180^\circ$  (transmission direction), corresponding to the direction of specular reflection and transmission. As expected, the light scattering of the nanorough coatings is substantially higher than the light scattering of the uncoated glass substrate. The highest ARS values can be observed for sample Z10, which also exhibits a small peak at  $\theta_s = 75^\circ$  in the ARS curve. The ARS curve of sample Z14 possesses such a peak in the range of its shoulders, too. These peaks are measurement artifacts.



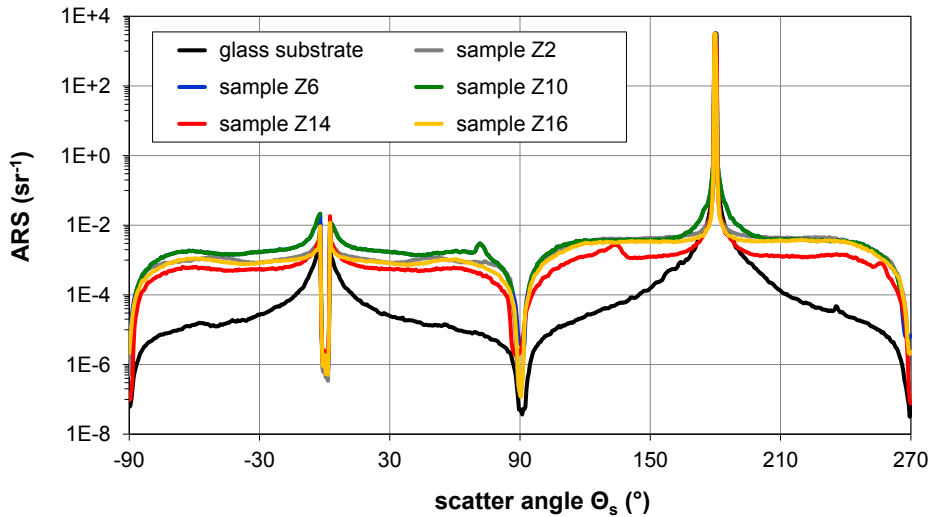


Fig. 7.25: ARS measurements of an uncoated glass substrate and superhydrophobic ZnO coatings.

The scatter loss of all samples was determined from the ARS data as described in section 2.3. As illustrated in Fig. 7.26, the resulting  $TS_f$  values of all examined superhydrophobic ZnO samples exceed the threshold for uncritical scattering (cf. section 3.3) into the transmission hemisphere. Although the main contribution to the necessary roughness structures for the wetting properties occur in the high spatial frequency range (see discussion in section 7.2.1), the roughness of the coatings in the scatter-relevant spatial frequency range induced unacceptable scatter losses. Furthermore, the scatter losses increased with increasing surface roughness.

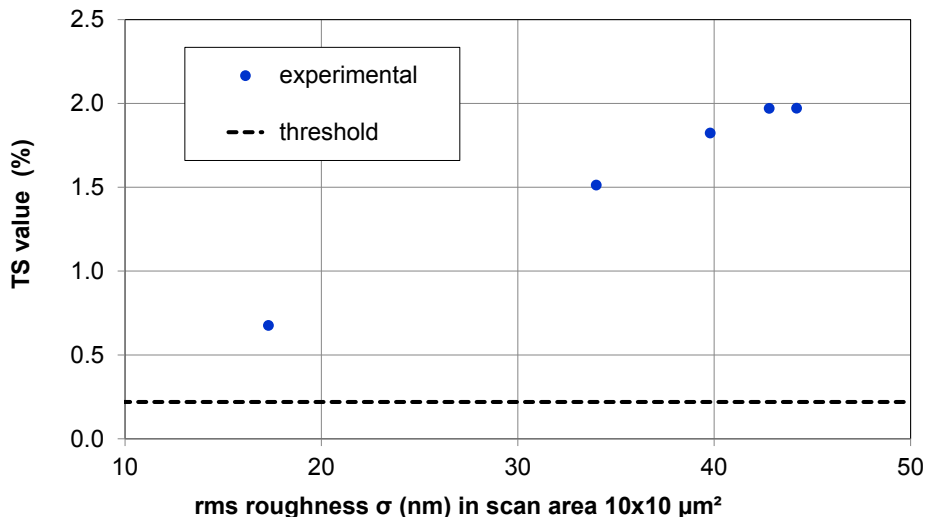


Fig. 7.26:  $TS_f$  values of superhydrophobic ZnO coatings compared to threshold level for uncritical scattering (cf. section 3.3).

Beside the optical properties, the mechanical stability is a further important parameter of optical coatings with superhydrophobic wettability. As for the light scattering, the problem arises that the mechanical stability decreases with increasing

surface roughness. In [87, 139], the authors studied the mechanical resistance to abrasion of sand. Mechanical robustness of a structure is considered as the resistance against the impact of rain drops in [97, 145]. In most cases however, mechanical stability is not discussed.

For the investigated samples in this thesis, the mechanical stability was examined with a chemo-mechanical hand-abrasion test called ABREX from Innowep GmbH. These abrasion tests reveal that the roughness structures of sputtered ZnO layer already fail under soft condition (small load, few abrasion cycles). This is described in [175]. Nevertheless, the mechanical instability will always be a problem for superhydrophobic surfaces, because of the contradictory relation between a certain surface roughness necessary for the wettability and its negative effect on the mechanical stability.

To investigate the long-term stability without mechanical stress, selected ZnO coatings with superhydrophobic behavior were analyzed regarding wettability after a three year time period.

Samples Z2, Z6, and Z10 which have a ZnO coating and PolyF1 as hydrophobic top layer still fulfill the criteria for  $SH_{pr}$ :  $\Theta_{aca} > 140^\circ$  (Fig. 7.27) and  $\alpha_{bo} \leq 40^\circ$  (Fig. 7.28). In contrast to these results, the wettability of the ZnO coatings with WR4 as hydrophobic top layers (see Fig. 7.27 and Fig. 7.28) deteriorate: Within the tolerance of the CA measurement,  $\Theta_{aca}$  is stable after three years, but the  $\Theta_{rca}$  considerably decreased. The bounce-off experiments show that the samples Z14 and Z16 are no longer superhydrophobic by the definition of section 6.1.3, because fallen drops stick to a  $40^\circ$  tilted surface (sample Z14) or residues can be observed (sample Z16).

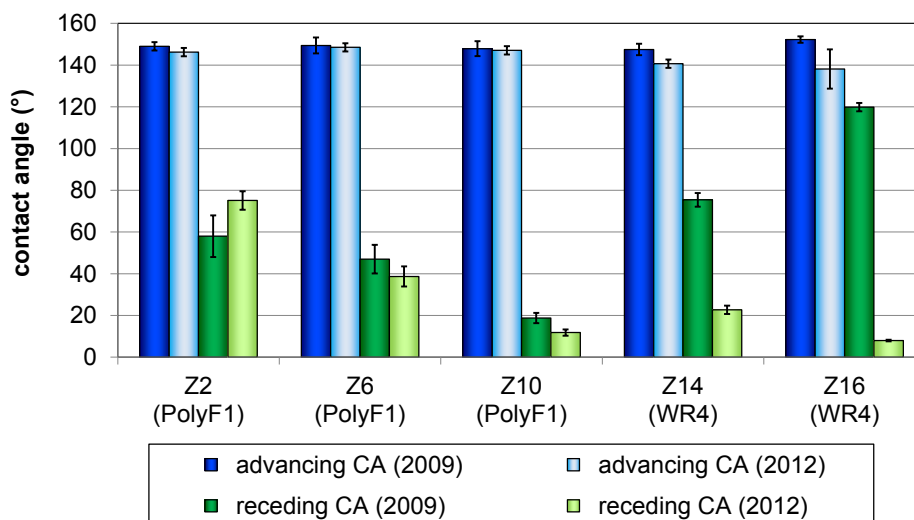


Fig. 7.27: Advancing CA and receding CA of ZnO coatings right after fabrication (2009) and three years later (2012).

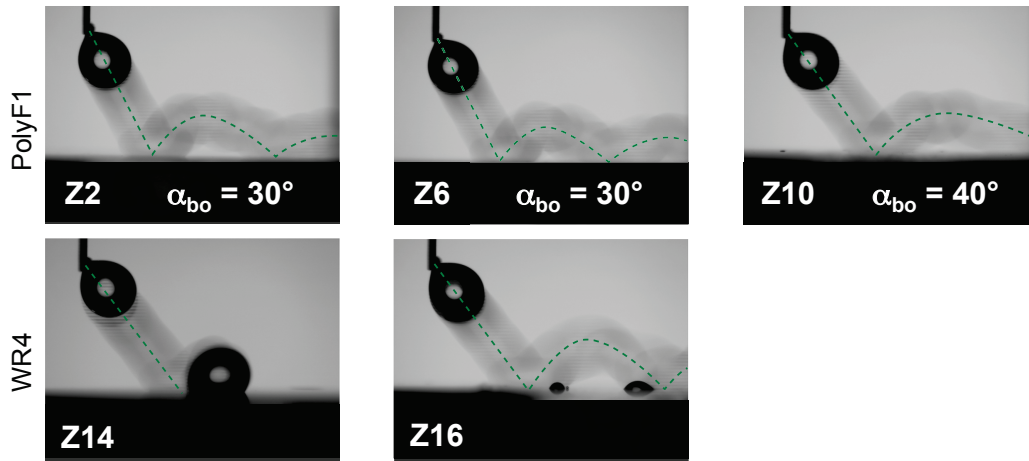


Fig. 7.28: Bounce-off experiment of ZnO coatings three years after fabrication.

For the samples Z14 and Z16 the question arises why both samples are hydrophobic and not superhydrophobic after three years without applying any mechanical stress. The reason for this deterioration of the wettability is either a damaged roughness structure or the chemical property of the hydrophobic top layer WR4 is gone.

The surface characteristic of both coatings can be proven by repeating and comparing the AFM measurements of both ZnO coatings right after the fabrication and three years later.

The roughness analysis results summarized in Fig. 7.29 and Fig. 7.30 reveal that the initial roughness structures of both samples are still intact. For sample Z14, the surface roughness (rms value and PSD function) increased after three years. Thus, the  $\kappa_B$  value increased from 0.45 to 0.57. The current nanostructure of sample Z16 is similar to the structure right after the coating fabrication. It can be concluded that the loss of the superhydrophobicity of both samples with WR4 as hydrophobic top layer is caused by a reduction of the intrinsic chemical properties.

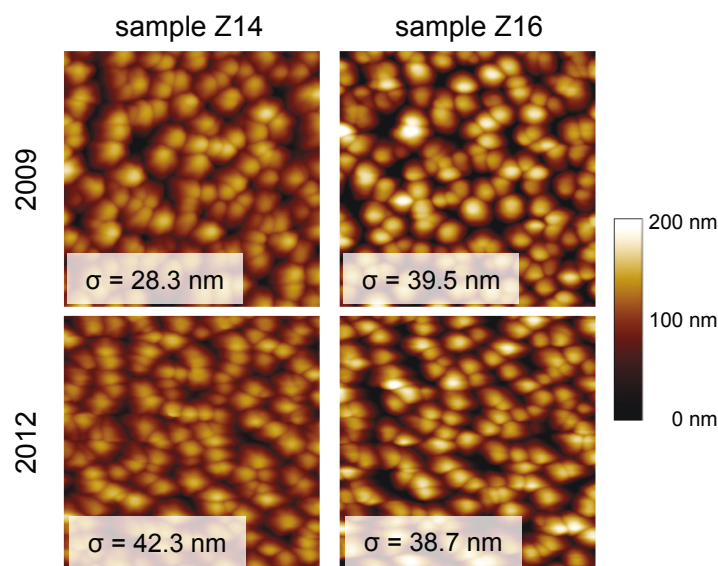


Fig. 7.29: Comparison between the roughness structure of samples Z14 and Z16 right after the fabrication (2009) and three years later (2012).

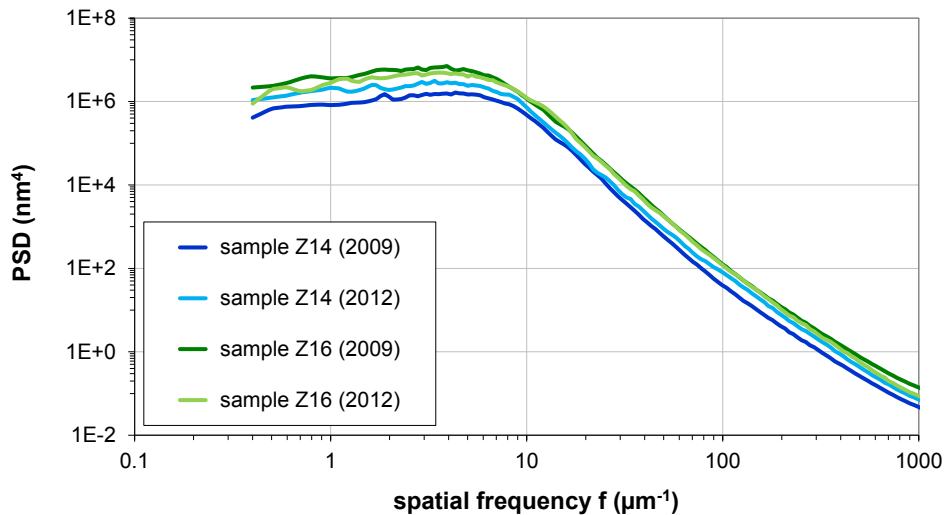


Fig. 7.30: Comparison between the PSDs of samples Z14 and Z16 right after the fabrication (2009) and three years later (2012).

The conclusions of this section are: The scatter losses of the investigated superhydrophobic samples exceed the threshold for uncritical visual scatter losses and hence are unacceptable for the specific sample application mentioned in chapter 5.

The surfaces with PolyF1 as top layer are superhydrophobic over a long time period, whereas the surfaces with WR4 as top layer exhibit only hydrophobic wetting properties after three years.

#### 7.2.4 Summary

The comprehensive study of the hydrophobic and superhydrophobic nanorough optical coatings using the measurement and analysis methodology results in the following conclusions:

- The optimization of the sputter process has been supported by the developed methodology based on the wetting parameter  $\kappa_B$ . A variation of the layer thickness leads to a variation of the roughness characteristic and hence to samples with varying  $\kappa_B$  values.
- Besides a sample series with varying ZnO layer thickness, a two-step sputter process was performed in order to fabricate a roughness characteristic with superhydrophobic wettability in combination with improved optical properties. However, the roughness structures were similar in the scatter-relevant spatial frequency range of both samples series (layer thickness variation and two-step process).
- Superhydrophobic samples have been fabricated by nanorough (non-hierarchical) ZnO coatings.

- The scatter losses induced by surface roughness of the superhydrophobic samples are higher than the acceptable scatter losses determined by optically esthetic requirements.
- A hydrophobic functionalization right after the sputter process led to an improved wettability: Sample with  $\kappa_B = 0.46$  is SH<sub>pr</sub>, and samples with  $\kappa_B \geq 0.6$  are SH. However, the superhydrophobic wetting properties of these samples with WR4 as top layer vanish after three years.
- Long-term experiments give rise to the assumption that the wettability of ZnO layers with PolyF1 as hydrophobic top layer could be stable over several years if they are not exposed to mechanical stress.

Concerning the suitability of the methodology for the specific ZnO roughness characteristic, the main conclusions are:

- The methodology could be used to predict, define, and control the roughness characteristic of nanorough ZnO thin film layers for optimal hydrophobicity in contrast to conventional trial-and-error approaches.
- The  $\kappa_B$  method enables separate control and characterization of the wetting effect of the fabricated roughness structures independent from the hydrophobic material properties.
- The observed results confirm the  $\kappa_B$  thresholds of 0.3 for SH<sub>pr</sub> and 0.4 for SH, which were acquired in section 7.1.

In conclusion, hierarchical structuring of the surfaces is not necessary to achieve superhydrophobic wetting properties. As shown by the lotus leaf (section 4.1), Al<sub>2</sub>O<sub>3</sub> sol-gel coatings (section 7.1), and ZnO sputtered coatings (section 7.2), nanorough structures are suitable to realize superhydrophobicity.

### 7.3 Hydrophilic nanorough optical coatings

In the following, the results of a first attempt to extend the roughness structure assessment based on the wetting parameter for hydrophobic wetting properties to hydrophilic surfaces is presented. Furthermore, the novel wetting analysis methods introduced in section 6.2 were utilized to characterize hydrophilicity.

These investigations aimed at supporting the process optimization concerning structural properties for anti-fog behavior. At the same time, the correlations between the process parameters, structural properties, and hydrophilic wettability were investigated. For this purpose, the process parameters of four sample series with

hydrophilic SiO<sub>2</sub> layers were systematically varied (see chapter 5). Finally, the light scattering of selected samples is presented.

### 7.3.1 Structural properties and hydrophilicity

In the first series consisting of three samples, the withdrawal velocity ( $v_{\text{draw}}$ ) was varied. The other process parameters (particle diameter:  $d_{\text{particle}} = 20$  nm, number of dip iterations:  $N_{\text{dip}} = 10$ , particle concentration:  $c_{\text{particle}} = 1\%$  w/w) were kept constant during the fabrication process.

The results of the AFM measurements and subsequent analysis (topography images, rms roughnesses, PSD functions, and  $\kappa_B$  values) are given in Fig. 7.31, Fig. 7.32, Tab. 7.11, and Tab. 7.12.

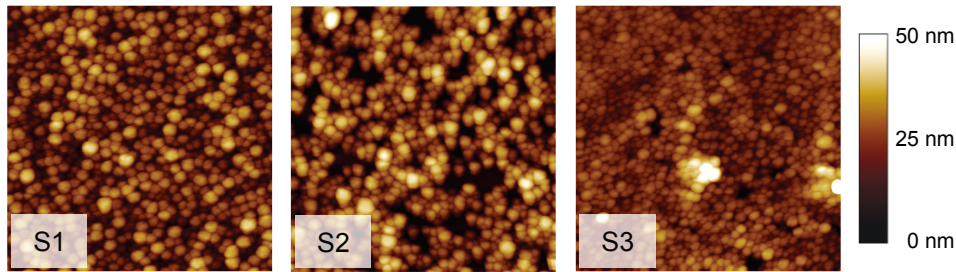


Fig. 7.31: AFM topography images of SiO<sub>2</sub> coatings with varying withdrawal velocity ( $v_{\text{draw}}$  from left to right: 1 mm/s, 2 mm/s, 3 mm/s). Scan area:  $1 \times 1 \mu\text{m}^2$ .

Tab. 7.11: Rms roughness values of SiO<sub>2</sub> coatings with varying withdrawal velocity.

sample	$v_{\text{draw}}$ (mm/s)	$\sigma$ (nm)		
		$0.5 \times 0.5 \mu\text{m}^2$	$1 \times 1 \mu\text{m}^2$	$10 \times 10 \mu\text{m}^2$
S1	1	5.8	5.8	6.1
S2	2	8.2	9.8	4.7
S3	5	5.6	5.8	5.4

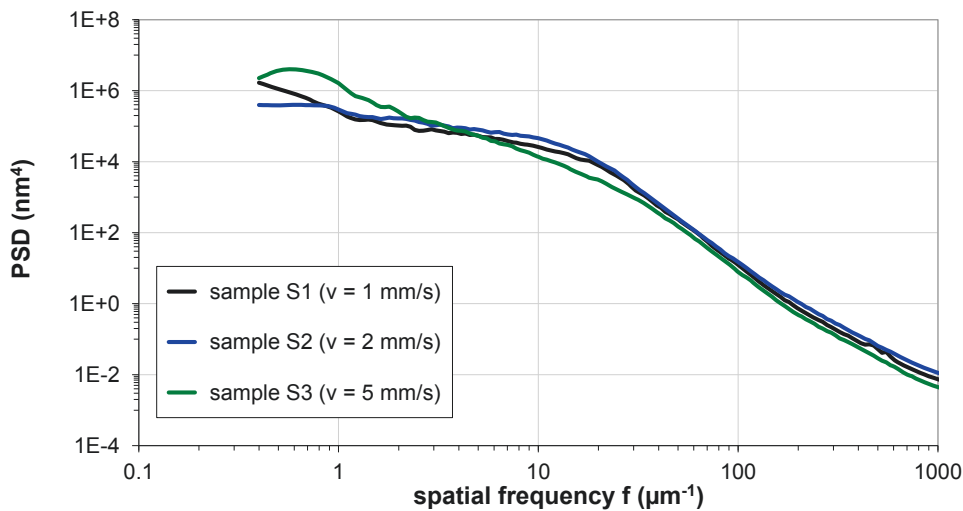


Fig. 7.32: PSD functions of SiO<sub>2</sub> coatings with varying withdrawal velocity.

Tab. 7.12: Wetting parameters of SiO<sub>2</sub> coatings with varying withdrawal velocity.

sample	V <sub>draw</sub> (mm/s)	κ <sub>B</sub> in different spatial bandwidths			
		(1 - 10) μm <sup>-1</sup>	(10 - 100) μm <sup>-1</sup>	(100 - 1000) μm <sup>-1</sup>	(1 - 1000) μm <sup>-1</sup>
<b>S1</b>	<b>1</b>	0.01	0.08	0.11	<b>0.20</b>
<b>S2</b>	<b>2</b>	0.01	0.09	0.13	<b>0.23</b>
<b>S3</b>	<b>5</b>	0.01	0.06	0.09	<b>0.16</b>

As for the hydrophobic ZnO coatings (section 7.2.1), the κ<sub>B</sub> values listed in Tab. 7.12 confirm the statements of section 3.1: The high spatial frequency range (10 μm<sup>-1</sup> ≤ f ≤ 1000 μm<sup>-1</sup>) represents the wetting-relevant range for coatings with nanorough surface characteristics because of the negligible κ<sub>B</sub> values for spatial frequencies smaller than 10 μm<sup>-1</sup>. From now on, only the summarized κ<sub>B</sub> value (1 μm<sup>-1</sup> ≤ f ≤ 1000 μm<sup>-1</sup>) will be used for the following discussion.

The topography images and quantities show that the roughness characteristics of all samples slightly differ from each other: The PSDs as well as κ<sub>B</sub> values increase from sample S3 to sample S1 and from sample S1 to sample S2. A clear correlation to v<sub>draw</sub> cannot be observed. It has however to be taken into consideration that the differences in κ<sub>B</sub> might be dominated by measurement uncertainty. The uncertainty of the κ<sub>B</sub> values amounts to ≤ 0.05 depending on determination and combination of the PSD functions from single measurements which are influenced by the surface quality and measurement artifacts (cf. section 3.1).

The determination of the porosity F and layer thickness d according to the method presented in section 3.4 leads to the following results:

- Sample S1: d = 82 nm and F = 23%.
- Sample S2: d = 69 nm and F = 6%.
- Sample S3: d = 12 nm and F = 5 %.

Based on the theoretical aspects discussed in section 2.2 and the findings of section 4.1 that increasing surface roughness and porosity result in enhanced hydrophilic wettability, the structural analysis results lead to the following expectation: The samples fabricated by smaller withdrawal velocities are more promising concerning optimal hydrophilicity than sample S3 fabricated with higher velocity (5 mm/s), because of the higher surface roughness and porosity of samples S1 and S2 compared to the structural properties of sample S3.

The results of the CA measurements are depicted in Fig. 7.33 as a function of the wetting time. In addition, for each sample, a function according to Eq. (6.1) was fitted to the CA behavior using K and m as fit parameters.

By comparing the fit parameters with the CA behavior, which are listed in Tab. 7.13, it becomes apparent that smaller  $K$  and  $m$  values are accompanied by stronger hydrophilic wettability (smaller CA) and faster spreading, respectively.

As predicted, sample S3 with the lowest  $\kappa_B$  value, lowest layer thickness, and lowest porosity exhibits the highest CA ( $\theta_0$  and  $\theta_{\text{mean}}$ ). Furthermore, the most fogging droplets ( $N_{\text{drops}}$ ) within this samples series (see Fig. 7.34) occur for this surface during the fogging experiment. The best wetting properties (small CA and less  $N_{\text{drops}}$ ) were achieved for sample S1 with comparatively high  $\kappa_B$  and high  $F$ .

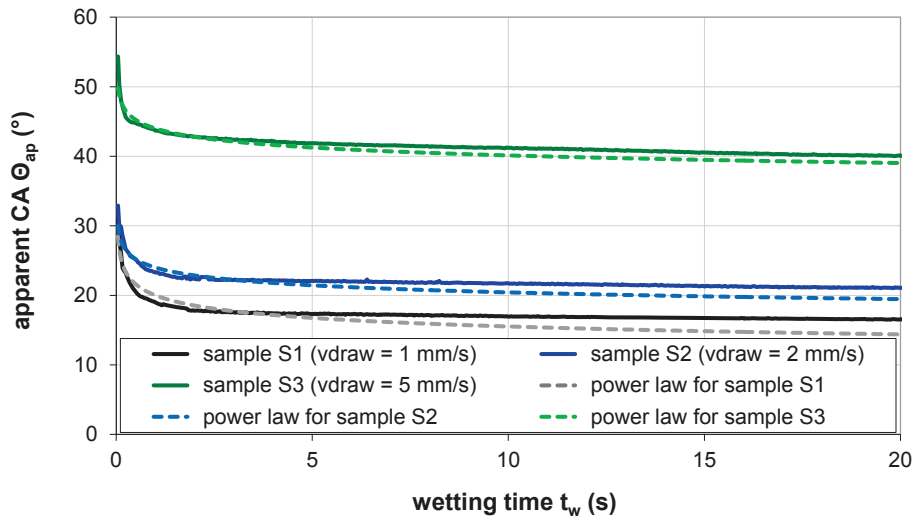


Fig. 7.33: CA behavior as a function of the wetting time of  $\text{SiO}_2$  sol-gel coatings with varying withdrawal velocity.

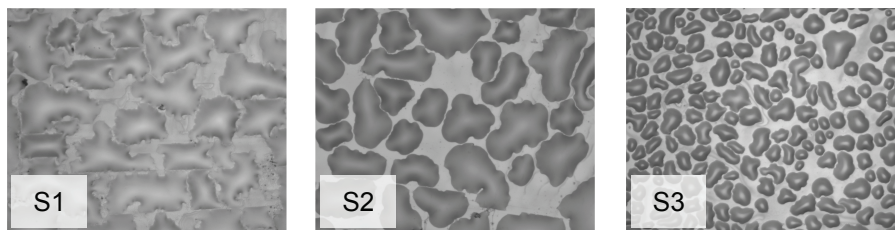


Fig. 7.34: Fogging behavior at  $t = 10$  s of  $\text{SiO}_2$  coatings with varying withdrawal velocity.

Tab. 7.13: List of wetting analysis results of  $\text{SiO}_2$  coatings with varying withdrawal velocity.

sample	$v_{\text{draw}}$ (mm/s)	CA behavior			fogging behavior	
		$\theta_0$ ( $^\circ$ )	$\theta_{\text{mean}}$ ( $^\circ$ )	fit parameters	$N_{\text{drops}}$	$t_{\text{fog}}$ (s)
S1	1	31	17	$K = 20; m = -0.11$	27	37
S2	2	33	21	$K = 24; m = -0.07$	35	36
S3	5	54	41	$K = 44; m = -0.04$	171	28

The presented results indicate a first correlation: The withdrawal velocity directly influences the layer thickness and thus the structural parameters effect the CA as well as  $N_{\text{drops}}$ .



For the second sample series of SiO<sub>2</sub> coatings with a varying number of dip iterations ( $N_{\text{dip}}$ ),  $v_{\text{draw}}$  is set to 1 mm/s, because the previous results indicate that the best hydrophilicity is achieved with the smallest withdrawal velocity. For particle diameter and particle concentration, the same parameters as for the first sample series were chosen.

Beside the topography images of a scan area of  $1 \times 1 \mu\text{m}^2$ , the topography images of a  $10 \times 10 \mu\text{m}^2$  scan area are presented in Fig. 7.35 in order to examine the homogeneity of the coatings. These images in the  $10 \times 10 \mu\text{m}^2$  scan areas show a dune-like roughness structure, especially for sample S6. This long correlated inhomogeneities might lead to inhomogeneous wetting properties.

The rms roughness (Tab. 7.14) and PSD functions (Fig. 7.36) in a spatial frequency range between  $100 \mu\text{m}^{-1}$  and  $1000 \mu\text{m}^{-1}$  reveal that with increasing  $N_{\text{dip}}$  the roughness quantities decrease. The highest  $\kappa_B$  value is observed for sample S4, which was fabricated through 5 dip iterations. Furthermore, the higher  $N_{\text{dip}}$  the higher is the layer thickness. Yet changes of  $N_{\text{dip}}$  do not affect the porosity.

Based on these results, the question arises which structural parameter (surface roughness or layer thickness) has a bigger influence on the wettability. The following wetting analysis was performed to clarify this question.

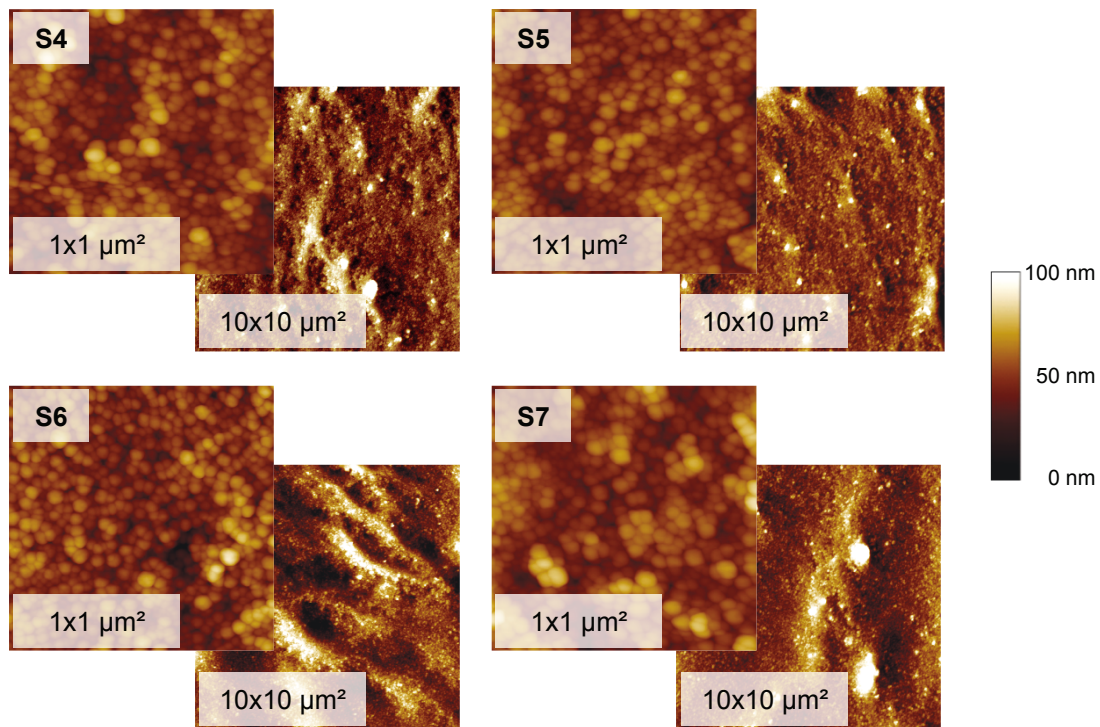


Fig. 7.35: AFM topography images of SiO<sub>2</sub> coatings with varying number of dipping iteration ( $N_{\text{dip}}$  from S4 to S7: 5, 10, 15, 20). Scan area:  $1 \times 1 \mu\text{m}^2$  and  $10 \times 10 \mu\text{m}^2$ .

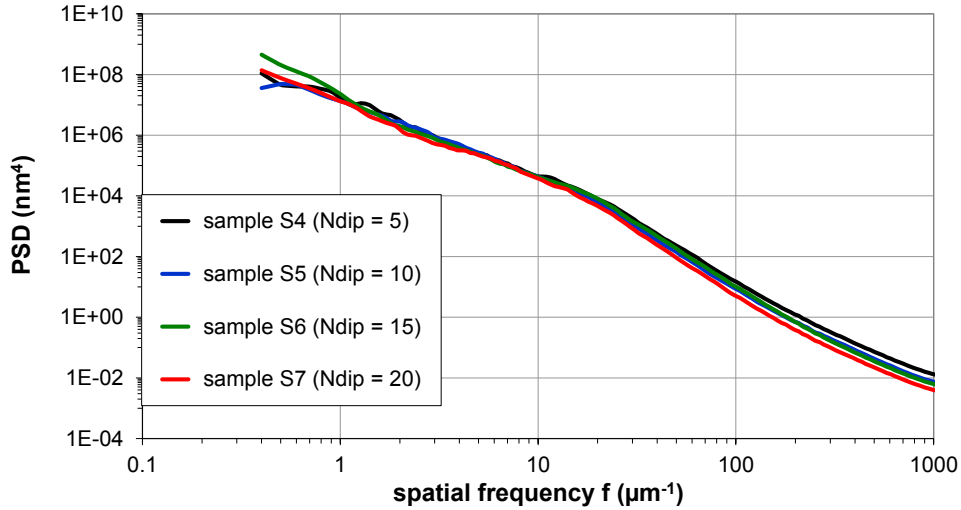


Fig. 7.36: PSD functions of SiO<sub>2</sub> coatings with varying number of dipping iteration.

Tab. 7.14: List of structural analysis results of SiO<sub>2</sub> coatings with varying number of dipping iteration.

sample	N <sub>dip</sub>	σ (nm)			κ <sub>B</sub>	d (nm)	F (%)
		0.5x0.5 μm <sup>2</sup>	1x1 μm <sup>2</sup>	10x10 μm <sup>2</sup>			
S4	5	11.2	9.4	17.0	0.24	49	41
S5	10	8.6	8.5	15.1	0.19	86	42
S6	15	7.8	8.2	24.3	0.19	136	48
S7	20	5.8	10.0	17.1	0.16	175	40

The results of the CA measurements (Fig. 7.37) and the fogging experiment (Fig. 7.38) show an excellent wetting behavior of sample S6 with  $\theta_{\text{mean}} < 4^\circ$  and complete as well as instantaneous wetting of condensing water. The other samples also exhibit comparatively good hydrophilic wettability with just small differences between each other (Tab. 7.15).

The results imply that with increasing N<sub>dip</sub>, and related decreasing κ<sub>B</sub> value, and increasing layer thickness, the fogging behavior is improved. However, because of the weak differences in the results, it is important to note that a robust correlation between structural properties and wettability cannot be determined.

The observed fit parameter of the CA behavior listed in Tab. 7.15 confirm the statement of Nonomura [176] who determined the fit parameter  $m = -0.3$  for the Tanner law in Eq. (6.1).

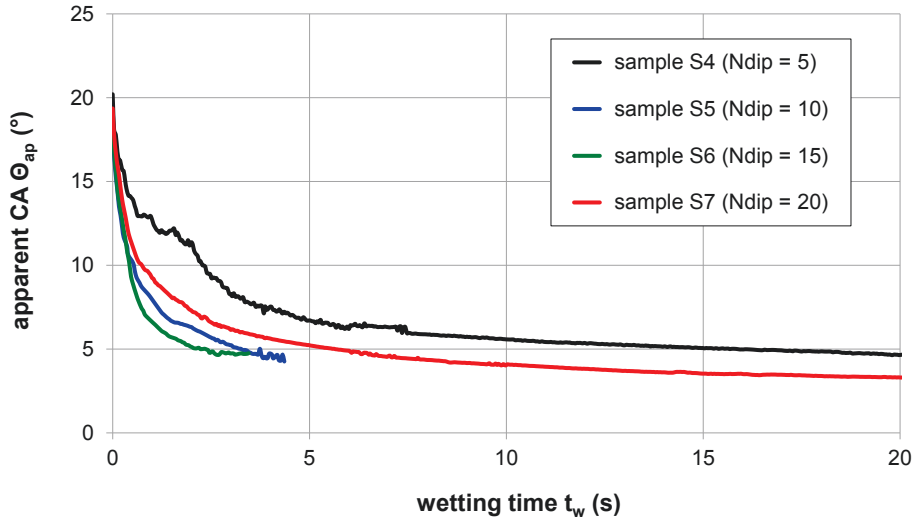


Fig. 7.37: CA behavior as a function of the wetting time of SiO<sub>2</sub> coatings with varying number of dipping iteration.

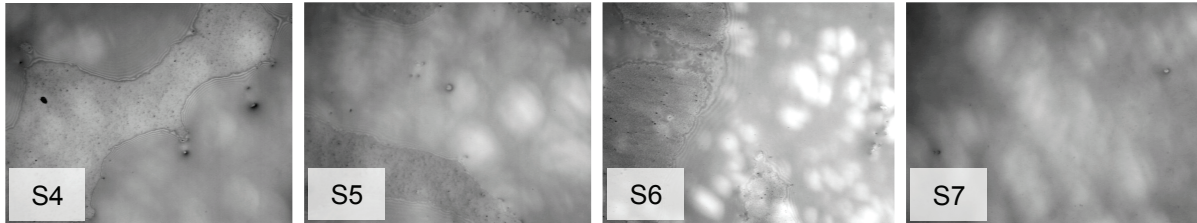


Fig. 7.38: Fogging behavior at  $t = 10$  s of SiO<sub>2</sub> coatings with varying number of dipping iteration.

Tab. 7.15: List of wetting analysis results of SiO<sub>2</sub> coatings with varying number of dipping iteration.

sample	N <sub>dip</sub>	CA behavior			fogging behavior	
		$\Theta_0$ (°)	$\Theta_{\text{mean}}$ (°)	fit parameters	N <sub>drops</sub>	t <sub>fog</sub> (s)
S4	5	19	5	$K = 11; m = -0.30$	2	47
S5	10	18	< 4	$K = 7.7; m = -0.34$	2	43
S6	15	18	< 4	$K = 6.7; m = -0.35$	1	25
S7	20	19	19	$K = 8.8; m = -0.33$	1	33

So far, the optimal hydrophilicity for SiO<sub>2</sub> coatings was realized through process parameters of  $v_{\text{draw}} = 1$  mm/s and  $N_{\text{dip}} = 15$ . These parameters were, therefore, used for the fabrication of the third sample series consisting of a particle diameter variation. A preliminary study and published results in [49] (cf. section 4.2) yielded that a particle diameter of  $> 70$  nm results in unacceptable structural and hydrophilic wetting properties (e.g. for  $d_{\text{particle}} = 100$  nm:  $\kappa_B = 0.13$ ,  $N_{\text{drops}} = 128$ ). Thus, only the influence of particles up to a diameter of 50 nm was investigated with respect to structural properties as well as wettability within this thesis.

As can be seen from the analysis results given in Fig. 7.39, Fig. 7.40, and Tab. 7.16, the higher the particle diameter the larger the roughness components in vertical

and lateral dimension: The rms roughness and the PSD function of the samples S10 and S11 are higher than the rms roughness and PSDs of the samples S8 and S9.

The layer thicknesses and porosities of samples S10 and S11 could not be estimated, because both samples exhibit particularly high scatter losses. Thus, the modeled spectra could not be fitted to the measured transmittance and reflectance spectra (cf. section 3.4). For this reason, an investigation of the correlation between the process parameters, structural properties, and wettability is only partly feasible.

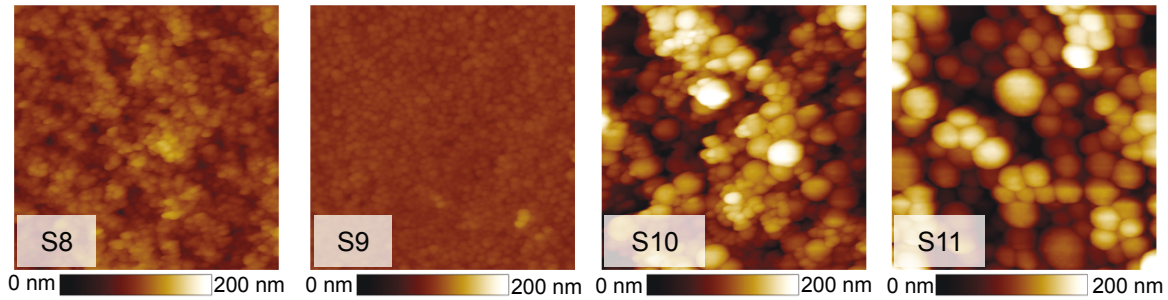


Fig. 7.39: AFM topography images of SiO<sub>2</sub> coatings with varying particle diameter ( $d_{\text{particle}}$  from S8 to S11: 5 nm, 15 nm, 35 nm, 50 nm). Scan area: 1x1  $\mu\text{m}^2$ .

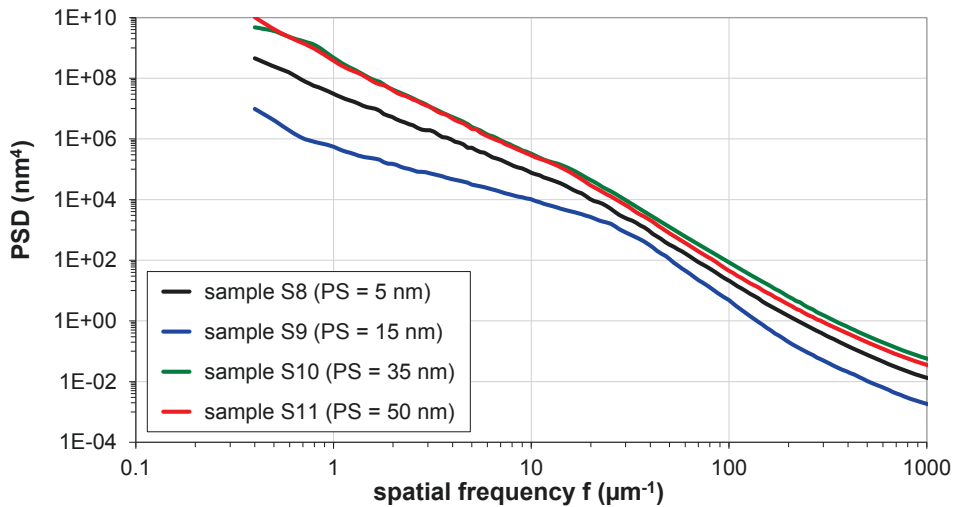


Fig. 7.40: PSD functions of SiO<sub>2</sub> coatings with varying particle diameter.

Tab. 7.16: List of structural analysis results of SiO<sub>2</sub> coatings with varying particle diameter.

sample	$d_{\text{particle}}$ (nm)	$\sigma$ (nm)			$\kappa_B$	d (nm)	F (%)
		0.5x0.5 $\mu\text{m}^2$	1x1 $\mu\text{m}^2$	10x10 $\mu\text{m}^2$			
S8	5	12.0	13.0	28.0	0.28	199	34
S9	15	3.9	3.9	5.1	0.11	119	20
S10	35	46.7	40.7	104.5	0.57	-	-
S11	50	35.4	43.0	102.5	0.46	-	-

The CA behavior in Fig. 7.41 and the fogging experiment images in Fig. 7.42 reveal that the best hydrophilic wettability is reached for sample S10, which was fabricated

using a SiO<sub>2</sub> particle diameter of 35 nm leading to the highest observed  $\kappa_B$  value:  $\theta_{\text{mean}} < 4^\circ$ ; The fit parameters  $K$  and  $m$  are the smallest in this sample series; In addition, during the evaporation with steam, a continuous film of condensed water was formed on the surface (Fig. 7.42), which dissolved after 10 s. Thus, this SiO<sub>2</sub> coating can be denoted as anti-fogging according to the criteria introduced in section 6.2.3.

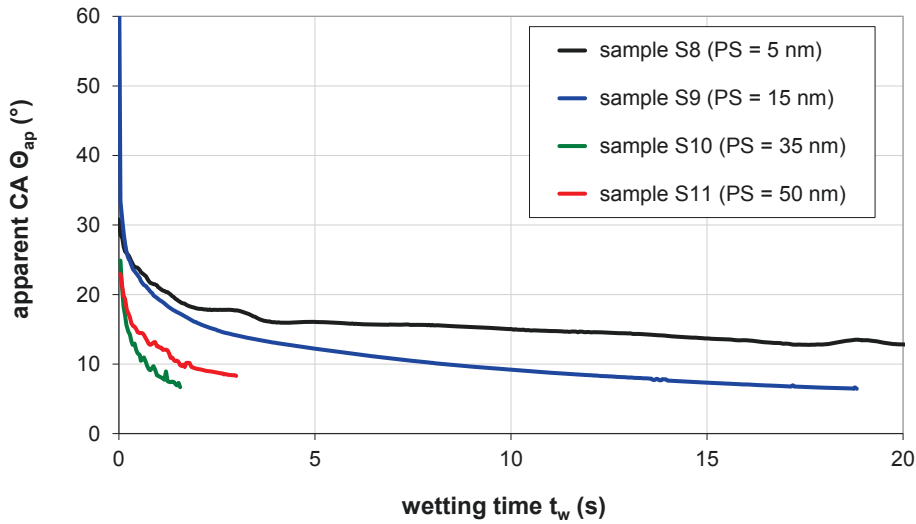


Fig. 7.41: CA behavior as a function of the wetting time of SiO<sub>2</sub> coatings with varying particle diameter.

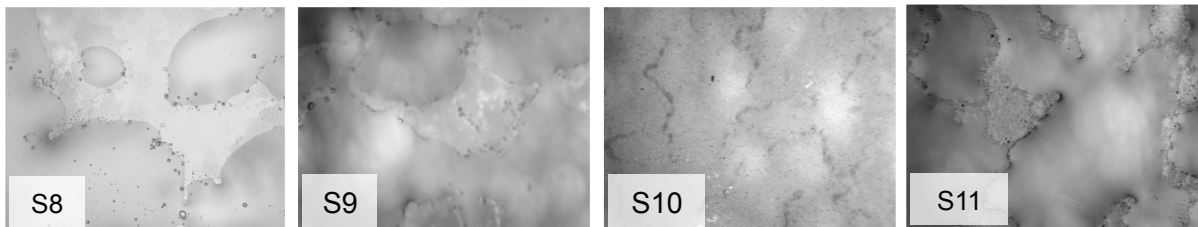


Fig. 7.42: Fogging behavior at  $t = 10$  s of SiO<sub>2</sub> coatings with varying particle diameter.

Tab. 7.17: List of wetting analysis results of SiO<sub>2</sub> coatings with varying particle diameter.

sample	$d_{\text{particle}}$ (nm)	CA behavior			fogging behavior	
		$\theta_0$ (°)	$\theta_{\text{mean}}$ (°)	fit parameters	$N_{\text{drops}}$	$t_{\text{fog}}$ (s)
S8	5	31	14	$K = 20.5; m = -0.14$	3	38
S9	15	34	8	$K = 28.5; m = -0.24$	4	32
S10	35	25	< 4	$K = 8.5; m = -0.37$	-	10
S11	50	23	< 4	$K = 11.7; m = -0.27$	4	41

With respect to possible correlation, the summarized results indicate that larger SiO<sub>2</sub> particles lead to higher surface roughness and thus to smaller CA as well as to improved fogging behavior. Nevertheless, this observation is only valid for particles smaller than 50 nm (cf. section 3.4).

Finally, the analysis results of three SiO<sub>2</sub> layers fabricated through varying particle concentration ( $c_{\text{particle}}$ ) and constant  $d_{\text{particle}} = 35 \text{ nm}$ ,  $N_{\text{dip}} = 15$ , and  $v_{\text{draw}} = 1 \text{ mm/s}$  are presented below. The results include neither porosity nor layer thickness, because it was not possible to achieve a meaningful adaptation of the modeled spectra on the measured transmittance and reflectance spectra (cf. section 3.4).

The assessment of the topography images (Fig. 7.43) illustrates that the investigated SiO<sub>2</sub> coatings possess comparable surface morphologies. Based on the roughness analysis results, the best hydrophilic wettability is expected for sample S13: This surface exhibits the highest PSD function (see Fig. 7.44) in the high spatial frequency range as well as the highest  $\kappa_B$  value (see Tab. 7.18) within this sample series.

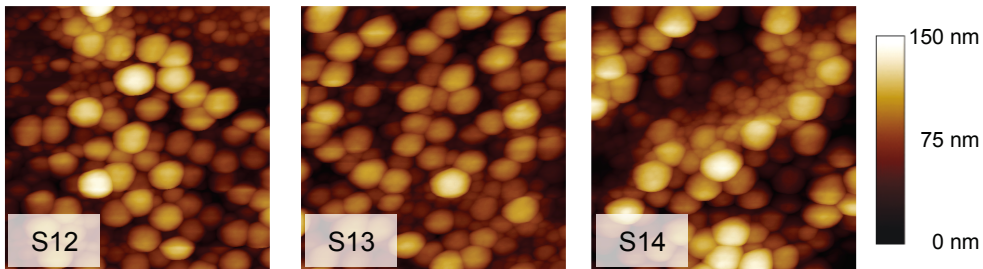


Fig. 7.43: AFM topography images of SiO<sub>2</sub> coatings with varying particle concentration ( $c_{\text{particle}}$  from S12 to S14: 0.6% w/w, 1.0% w/w, 1.4% w/w). Scan area:  $1 \times 1 \mu\text{m}^2$ .

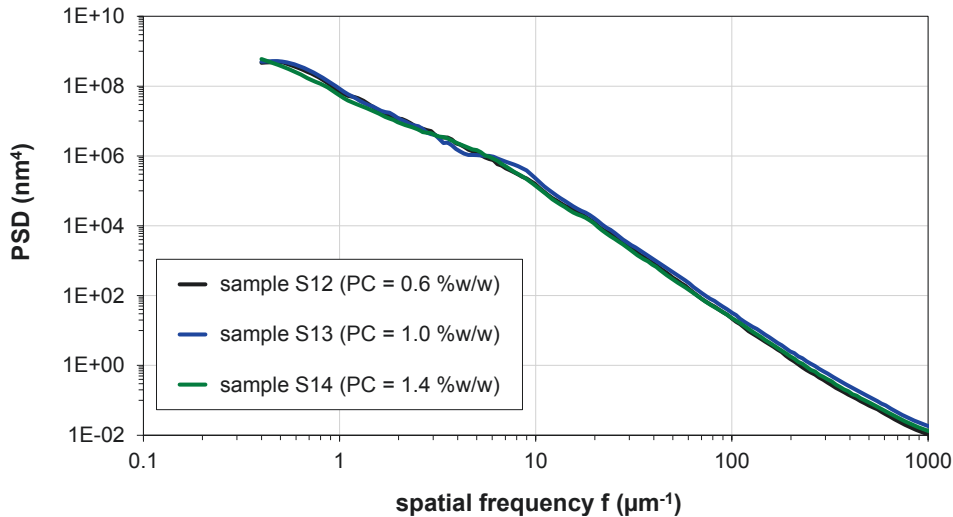


Fig. 7.44: PSD functions of SiO<sub>2</sub> coatings with varying particle concentration.

Tab. 7.18: List of structural analysis results of SiO<sub>2</sub> coatings with varying particle concentration.

sample	$c_{\text{particle}}$ (% w/w)	$\sigma$ (nm)			$\kappa_B$
		$0.5 \times 0.5 \mu\text{m}^2$	$1 \times 1 \mu\text{m}^2$	$10 \times 10 \mu\text{m}^2$	
S12	0.6	13.5	19.5	34.4	0.29
S13	1.0	20.8	22.1	37.3	0.35
S14	1.4	19.1	19.6	35.5	0.30

The wetting analysis results listed in Tab. 7.19 prove that sample S13 with the highest  $\kappa_B$  indeed yields the best hydrophilic wetting behavior within this sample series: smallest CA, smallest fit parameter, and shortest fogging time.

Nevertheless, sample S13 fabricated under the same process conditions as sample S10, does not exhibit a similar excellent wetting behavior: The measured CA is higher than  $10^\circ$  and during the fogging experiment several droplets occur. The reason is that the reproducibility of the structural properties of the samples was not optimized for the first systematical investigation.

Tab. 7.19: List of wetting analysis results of SiO<sub>2</sub> coatings with varying particle concentration.

sample	C <sub>particle</sub> (% w/w)	CA behavior			fogging behavior	
		$\theta_0$ (°)	$\theta_{\text{mean}}$ (°)	fit parameters	N <sub>drops</sub>	t <sub>fog</sub> (s)
S12	0.6	23	13	$K = 16.5; m = -0.13$	10	30
S13	1.0	24	11	$K = 15.5; m = -0.15$	10	29
S14	1.4	28	15	$K = 19.0; m = -0.12$	10	36

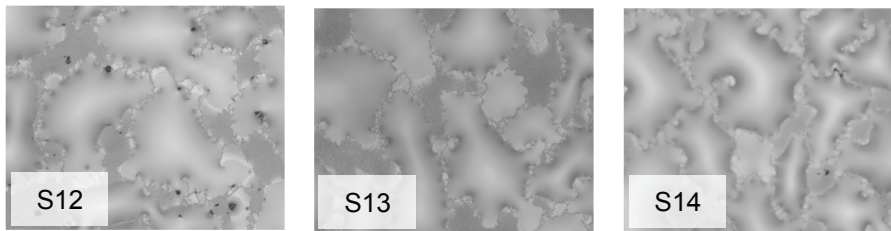


Fig. 7.45: Fogging behavior at t = 10 s of SiO<sub>2</sub> coatings with varying particle concentration.

An important conclusion of the first systematical investigation of the hydrophilic surfaces using the  $\kappa_B$  method is that the wetting-relevant spatial frequency range of nanorough hydrophilic SiO<sub>2</sub> coatings is located between  $10 \mu\text{m}^{-1}$  and  $1000 \mu\text{m}^{-1}$  as for the hydrophobic nanorough surfaces.

The observed correlations between the process parameters, structural properties, and wetting behavior for each of the four sample series are summarized below:

- Decreasing withdrawal velocity leads to increasing layer thickness, which results in decreasing CA and decreasing number of visible fogging droplets.
- Increasing number of dipping iterations leads to increasing surface roughness resulting in improved fogging behavior. But, for this sample series, the difference in the structural and wetting properties are rather small.
- Larger particles result in higher surface roughness, smaller CA, and improved fogging behavior.
- For the sample series with varying particle concentration, the sample with the highest  $\kappa_B$  value exhibits the best hydrophilic wetting.

Nevertheless, it should be mentioned that it was not possible to completely separate the structural properties (surface roughness, porosity, layer thickness) and hence the respective effects on the functional properties within the framework of this thesis. This means, the presented relationships are first results of a first study which have to be substantiated with further investigations.

### 7.3.2 Optical properties

The scattering behavior influenced by surface roughness and probably by porosity is of interest for the hydrophilic SiO<sub>2</sub> coatings with respect to the final sample application, e.g. glasses, bathroom mirrors or shower cubicles. For this purpose, three samples of the examined sample series were selected to determine the scatter losses. Each of the three samples exhibits different structural properties, but similar hydrophilic wetting behavior including sample S10 with anti-fog property.

Angle resolved light scattering measurements were performed at a wavelength of 532 nm using the instrumentation described in section 3.3. The results are shown in Fig. 7.46.

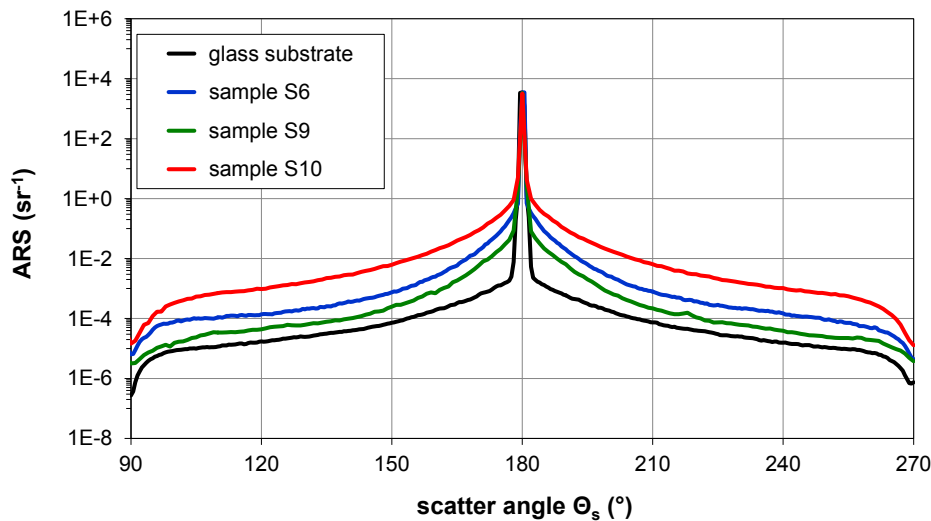


Fig. 7.46: Results of ARS measurements of bare glass substrate and SiO<sub>2</sub> sol-gel coatings.

From the ARS measurements, TS values (transmission direction) of 0.97% (sample S6), 0.28% (sample S9), and 4.66% (sample S10) were determined. Thus, only the scatter loss of sample S9 is close to the threshold of 0.22% for optical esthetic requirements (cf. section 3.4). As presented in the previous section, this sample shows the lowest surface roughness in the scatter-relevant spatial frequency range and the lowest porosity of the three samples. The considerable difference of the scatter losses between these samples results not only from the enhanced roughness, but also from the increased porosity (sample S9:  $F = 20\%$ , sample S6:  $F = 48\%$ ).



### 7.3.3 Summary

In these first systematical investigations of hydrophilic surfaces aiming at anti-fog behavior, structural as well as wetting properties were quantified by means of the novel measurement and analysis methodology. For the first time, in contrast to the most published findings, structural properties were comprehensively determined through rms values and PSD functions as well as by porosity and layer thickness. As described in chapter 4, only a few works reporting on hydrophilicity consider the effect of surface roughness in detail and appropriately. Often, only qualitative analysis by SEM is performed or the structural properties are not considered at all. The same applies to wetting analysis: The fogging behavior is mainly only qualitatively described in the literature [13, 110, 112, 113, 164]. In this thesis, the acquired wetting analysis methods were used to quantify the CA and the fogging behavior of SiO<sub>2</sub> layers.

By utilizing this characterization methodology, the basis for supporting the fabrication process of anti-fog surfaces through SiO<sub>2</sub> layers was given. Furthermore, a first investigation of the relations between the process parameters, structural properties, and hydrophilic wettability were performed.

The general consideration of all analysis results presented in section 7.3.1, independent of the sample series, leads to the conclusion that increasing porosity causes a decreasing apparent CA. This trend is illustrated in Fig. 7.47 using a least square fit of the determined data. Furthermore, the layer thickness influences the wettability as well, although a complete separation from the porosity is not possible yet.

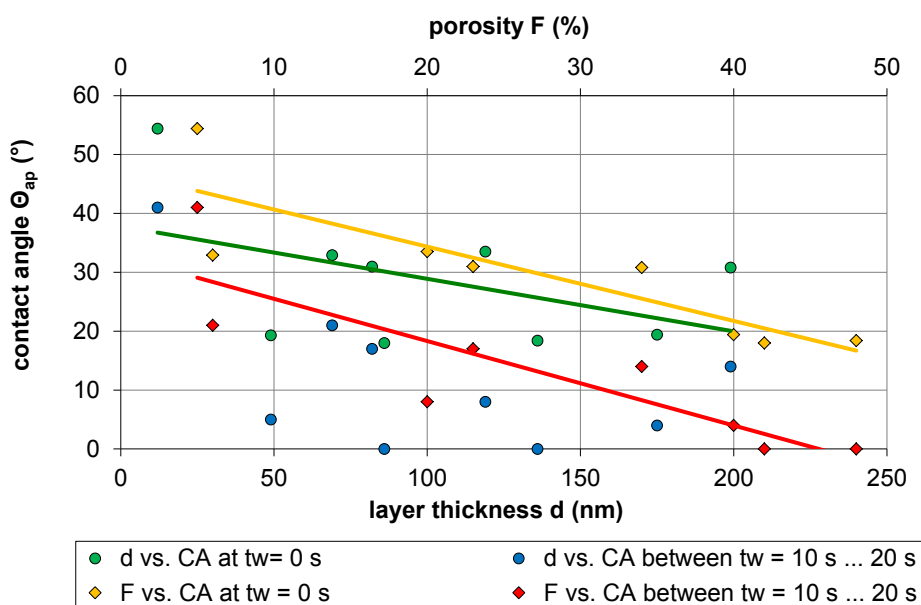


Fig. 7.47: Correlation between layer thickness and apparent CA as well as porosity and apparent CA of all SiO<sub>2</sub> layers investigated within this thesis. The trends are illustrated using least square fitting.

Within this first systematical investigation of hydrophilic coatings, no distinct correlation between the surface roughness and wettability could be observed. However, as mentioned in the theoretical section 2.2, the results indicate that high surface roughness related with high  $\kappa_B$  values has a positive effect on hydrophilicity. For instance, an  $\text{SiO}_2$  layer fabricated through certain process parameters ( $d_{\text{particle}} = 35 \text{ nm}$ ,  $N_{\text{dip}} = 15$ ,  $v_{\text{draw}} = 1 \text{ mm/s}$ ,  $c_{\text{particle}} = 1\% \text{ w/w}$ ) with the highest observed  $\kappa_B$  value (0.57) yielded excellent hydrophilic properties and hence anti-fog behavior as illustrated in Fig. 7.48.



Fig. 7.48: Fogging experiment: Bank note viewed through a glass plate with (half-side) hydrophilic  $\text{SiO}_2$  coating (left, uncoated; right, coated).

In addition to the roughness and wetting analysis, the total scatter of selected hydrophilic surfaces was determined. Since none of these first samples exhibited tolerable scatter as a result of rather high roughness and porosity, further improvement is required.

Summarizing the findings of these first systematic investigations, it can be concluded that the  $\kappa_B$  method established for hydrophobicity can be transferred to hydrophilic surfaces. Nevertheless, it is necessary to confirm this conclusion through larger statistical sample series. Furthermore, in case of hydrophilicity, the structural analysis as part of the methodology has to be extended to porosity and thin film thickness. Finally, the acquired wetting analysis methods (chapter 6.2) are suitable to comprehensively characterize the hydrophilic wettability.

### 7.4 Hydrophobic and superhydrophobic microstructured surfaces

Microstructured aluminum surfaces were fabricated to achieve superhydrophobicity (SH or  $\text{SH}_{\text{pr}}$ ). These engineering surfaces are analyzed with respect to surface roughness and hydrophobicity using the measurement and analysis methodology presented in the preceding sections. In this way, the suitability of this methodology shall be proven for microrough surfaces as well.

The roughness analysis was performed by three different measurement techniques to obtain roughness information within a large spatial frequency range and to identify the wetting-relevant spatial frequencies. As explained in section 3.1, the AFM is used for the high frequency roughness characterization, and the WLI or LSM for the measurements in the mid spatial frequency range. Nevertheless, the following roughness analysis results will show that not all measurement techniques are suited to obtain evaluable topography data of each sample. The reasons for such failures were partly already introduced in section 3.1 and will be further discussed for these particular surfaces.

The rms values determined from the topography data and listed in Tab. 7.20 display that only the WLI was capable to determine the surface morphology in several scan areas of all samples.

Tab. 7.20: Rms roughness of microrough Al surfaces.

sample	$\sigma$ ( $\mu\text{m}$ )				
	184x184 $\mu\text{m}^2$ (LSM)	698x523 $\mu\text{m}^2$ (WLI)	140x105 $\mu\text{m}^2$ (WLI)	70x53 $\mu\text{m}^2$ (WLI)	10x10 $\mu\text{m}^2$ (AFM)
<b>E1</b>	-	1.31	1.31	0.75	0.15
<b>E2</b>	-	0.45	0.34	0.18	0.03
<b>E3</b>	10.1	14.3	9.88	7.55	-
<b>E4</b>	10.2	18.8	9.41	7.09	-

In the high spatial frequency range, the maximum vertical measuring range of the AFM ( $< 5 \mu\text{m}$ ) is smaller than the vertical dimension of the roughness structure of samples E3 and E4 (cf. Fig. 7.49: peak-to-valley  $> 30 \mu\text{m}$ ). Thus, AFM measurements fail for both samples. In contrast, the surface characteristics of the samples E1 and E2 are too smooth (rms  $< 2 \text{ nm}$  for scan area  $184 \times 184 \mu\text{m}^2$ ) to receive consistent data from the LSM measurements (vertical resolution: rms  $< 100 \text{ nm}$  for scan area  $184 \times 184 \mu\text{m}^2$ ). Nevertheless, even for the WLI measurements, missing data points illustrated as black areas in Fig. 7.49 appear at steep roughness structures. These missing topography information negatively influenced the PSD values. Consequently, the PSD functions and  $\kappa_B$  values were not determined in entire investigated spatial frequency range for each sample, as shown in Fig. 7.50 and Tab. 7.21.

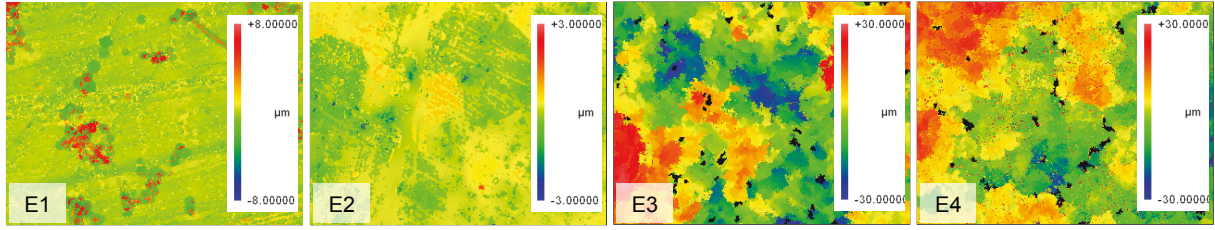


Fig. 7.49: WLI topography images of microrough Al surfaces. Scan area:  $140 \times 105 \mu\text{m}^2$ .

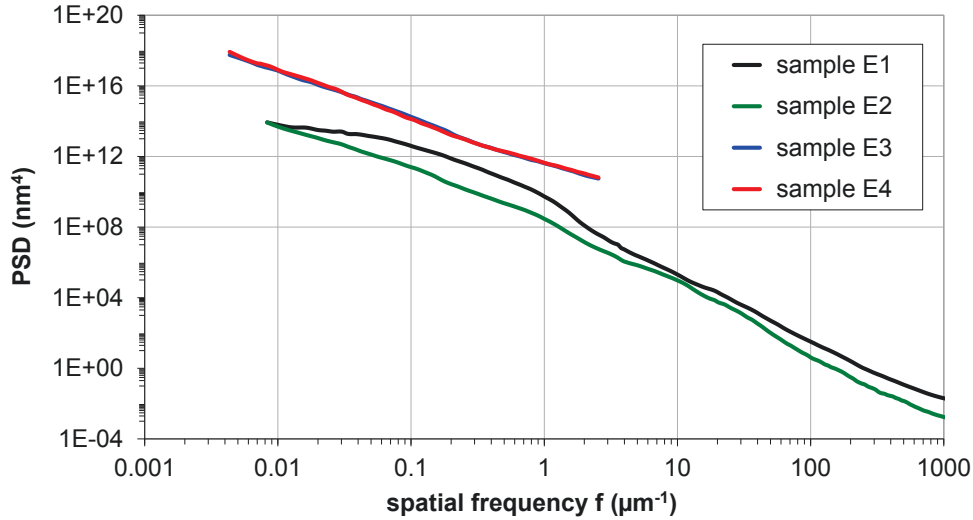


Fig. 7.50: PSD functions of microrough Al surfaces.

Tab. 7.21: Wetting parameters of microrough aluminum surfaces.

sample	$\kappa_B$ in different spatial bandwidths					
	$(0.01 - 0.1) \mu\text{m}^{-1}$	$(0.1 - 1) \mu\text{m}^{-1}$	$(1 - 10) \mu\text{m}^{-1}$	$(10 - 100) \mu\text{m}^{-1}$	$(100 - 1000) \mu\text{m}^{-1}$	$(0.01 - 10) \mu\text{m}^{-1}$
<b>E1</b>	0.02	0.11	0.11	0.12	0.18	<b>0.24</b>
<b>E2</b>	0.01	0.02	0.04	0.06	0.06	<b>0.07</b>
<b>E3</b>	0.15	0.45	0.05	-	-	<b>0.65</b>
<b>E4</b>	0.15	0.43	0.05	-	-	<b>0.63</b>

The  $\kappa_B$  values reveal that the wetting-relevant spatial frequency range of these microrough samples differs from that of the nanorough coatings ( $10 \mu\text{m}^{-1} \leq f \leq 1000 \mu\text{m}^{-1}$ ) investigated in the previous sections. For sample E1 and sample E2, the contributions to the wetting parameter increase step by step with higher spatial frequencies, but only within the uncertainty of the  $\kappa_B$  values (cf. section 7.3.1). For samples E3 and E4, the main contribution to  $\kappa_B$  occurs in the spatial frequency range between  $0.1 \mu\text{m}^{-1}$  and  $10 \mu\text{m}^{-1}$ .

For the following considerations, the fact of different wetting-relevant spatial frequency ranges of all samples are ignored, for the sake of simplicity. The contributions to  $\kappa_B$  are summarized only in the spatial frequency range between  $0.01 \mu\text{m}^{-1}$  and  $10 \mu\text{m}^{-1}$  to compare the roughness based  $\kappa_B$  values. Based on these

results, samples E3 and E4 with a  $\kappa_B$  value higher than 0.4 exceed the threshold, superhydrophobicity becomes possible.

The wetting results given in Fig. 7.51 show that samples E1 and E2 are just hydrophobic: Both surfaces exhibit a CA hysteresis  $\geq 80^\circ$  and drops do not roll or bounce off a tilted surface. In contrast, samples E3 and E4 exhibit a SH effect: The  $\theta_{aca}$  are around  $140^\circ$  combined with a low CA hysteresis of  $\leq 20^\circ$ . Thus, spherical drops easily roll off a slightly tilted surface ( $\alpha \leq 4^\circ$ ).

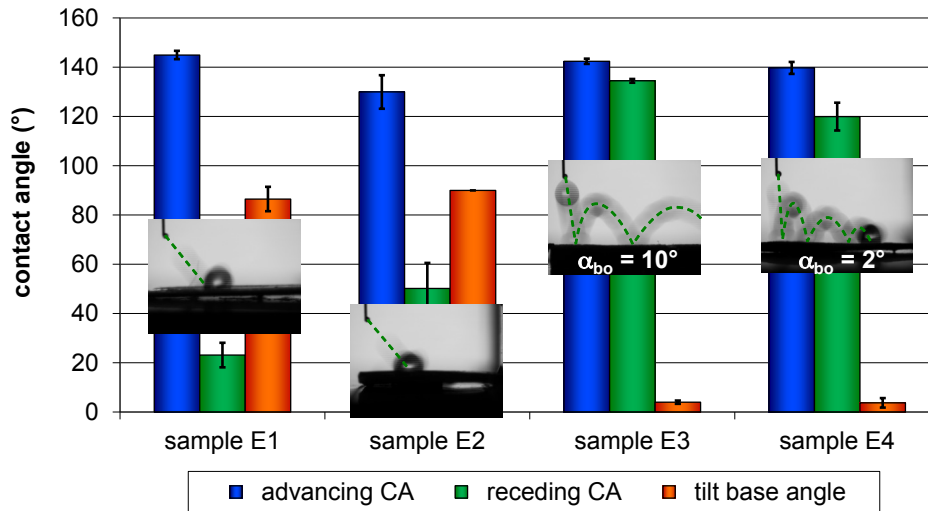


Fig. 7.51: Advancing CA, receding CA, tilt base angle, and bounce-off angle of microrough Al surfaces.

It is important to note that SH can be observed for both samples with  $\theta_{aca} \approx 140^\circ$ , but not  $\theta_{aca} \gtrsim 150^\circ$ , as by definition in section 6.1.3. This shows that the criteria for SH and  $SH_{pr}$  should be handled rather flexible. Small CA hysteresis and the roll-off behavior of water drops are more important for superhydrophobicity. This fact is also mentioned in [36].

The correlation between  $\kappa_B$  and the wetting behavior (Fig. 7.52 on the next page) reveals both wetting states: Homogeneous wetting can be found in the first part ( $0 < \kappa_B < 0.3$ ), which shows high  $\theta_{aca}$  but also high CA hysteresis. In this case, drops stick on tilted samples (up to  $90^\circ$ ). In the second part ( $\kappa_B > 0.6$ ), heterogeneous wetting is observed. Here  $\theta_{aca}$  remained approximately unchanged, but the CA hysteresis decreased significantly. In this regime, the samples exhibit low tilt base angles ( $\alpha < 20^\circ$ ).

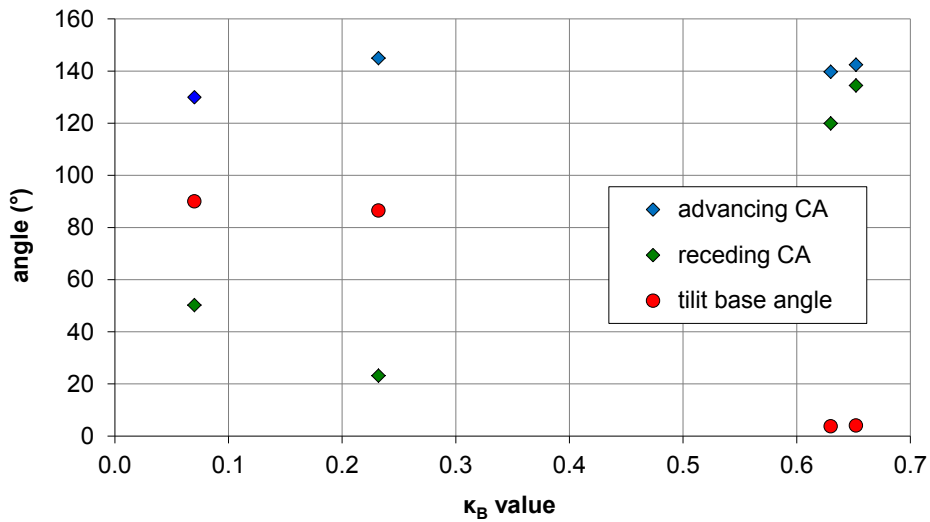


Fig. 7.52: Correlation between the  $\kappa_B$  value and the wetting results of the microrough Al surfaces.

The following conclusions can be drawn from the investigations of the microrough aluminum surfaces:

- The measurement and analysis methodology developed for nanorough surfaces can be used for microrough surfaces as well.
- The  $\kappa_B$  values of samples E1 and E2 do not exceed the threshold for SH<sub>pr</sub> ( $\kappa_B > 0.3$ ). The subsequent wetting analysis results confirm the prediction that both samples are non-superhydrophobic.
- Samples E3 and E4 with a  $\kappa_B > 0.4$  exhibit SH properties.

## 8 Conclusions and outlook

Functional surfaces with specific wetting properties for high quality optical components or mass products with esthetic requirements (e.g. easy to clean lenses and mirrors, decorative glass, bathroom mirrors) are of tremendously increasing interest. For instance, the reduced use of detergents and efficient manufacturing process strategies constitute main keys for resource conservation and thus concerning economical aspects as well. In particular, an effective realization of superhydrophobic and hydrophilic wettability demands a thorough characterization of structural, wetting, and optical properties. This thesis is hence focused on the development of a comprehensive measurement and analysis methodology. This comprises the selection, adaption, and extension of existing roughness and wetting analysis methods as well as the achievement of novel methods with respect to wetting systems with different stochastically rough surfaces and chemical properties.

The roughness characteristics of the samples were described by the root mean square roughness and power spectral density (PSD) functions. Subsequently, the wetting parameter  $\kappa_B$  was calculated from the PSD using a data reduction algorithm developed during earlier investigations. The  $\kappa_B$  approach provides the opportunity to analyze the roughness characteristics of stochastic surface structures with specific wetting properties separated from their chemical conditions. In this thesis, it was proven that the characterization of the high spatial frequency range ( $10 \mu\text{m}^{-1} \leq f \leq 1000 \mu\text{m}^{-1}$ ) is sufficient to assess the roughness potential for optimal hydrophobicity of nanorough surfaces using this approach. Therefore, roughness measurements were performed by Atomic Force Microscopy (AFM) in this range. For microstructured surfaces, the roughness had to be analyzed over a wider spatial frequency range using a combination of AFM and White Light Interferometry or Laser Scanning Microscopy.

For thorough wetting analysis of samples with various roughness characteristics and intrinsic wettabilities, novel methods were developed: In the case of hydrophobic surfaces with advancing contact angles  $\Theta_{aca} > 140^\circ$  and tilt base angles  $\alpha > 20^\circ$ , a procedure based on the natural behavior of raindrops falling onto plant leaves was introduced. The bounce-off angle ( $\alpha_{bo}$ ) was defined as the surface tilt angle at which falling water drops (volume: 6  $\mu\text{l}$ , height: 6 mm) bounce off without any residue.

For the drop spreading behavior of hydrophilic surfaces with apparent contact angles  $\Theta_{ap} \lesssim 20^\circ$ , where advancing and receding contact angle (CA) measurements fail, two characteristic CA were introduced using  $\Theta_{ap}$  as a function of the wetting time ( $t_w$ ):  $\Theta_{ap}$  at  $t_w = 0$  s and an averaged  $\Theta_{ap}$  between  $t_w$  of 10 s and 20 s. The fogging properties were quantified through a new quantitative fogging experiment. During this

experiment, the sample is exposed to water vapor and the recorded fogging behavior is subsequently analyzed regarding the number of droplets and fogging time.

By means of the suggested wetting analysis methods, novel criteria for extreme wettability were established. For superhydrophobicity, practical criteria ( $SH_{pr}$ :  $\theta_{aca} \gtrsim 140^\circ$ ,  $\alpha_{bo} \leq 40^\circ$ ) were introduced beside the definition of strict theoretical criteria (SH:  $\theta_{aca} \gtrsim 150^\circ$ , small CA hysteresis,  $\alpha \lesssim 20^\circ$ ). The term anti-fog was defined through  $\theta_{ap} \lesssim 20^\circ$  and the requirement that the condensing water wets the surface completely and instantaneously.

For the validation of the developed measurement and analysis methodology, the methods were applied to optical and engineering surfaces with different structural and chemical properties. Simultaneously, the correlations between the roughness, wettability, and optical properties were examined.

The investigation of hydrophobic samples with different roughness characteristics revealed that  $\kappa_B$  thresholds of 0.3 and 0.4 are suitable as necessary criteria for  $SH_{pr}$  and SH, respectively. This is proven by the fact that the surfaces investigated in this thesis with  $\kappa_B$  values smaller than these thresholds are not  $SH_{pr}$  or SH. Moreover, the desired self-cleaning effect could be observed for superhydrophobic surfaces, independent of  $SH_{pr}$  or SH.

Furthermore, nanorough  $Al_2O_3$  coatings with superhydrophobic wetting properties combined with low light scattering (scatter loss  $< 0.1\%$  in transmission direction) were presented. For sputtered nanorough ZnO coatings, the manufacturing process was essentially supported up to the realization of superhydrophobicity (e.g. for  $SH_{pr}$ :  $\theta_{aca} = 149^\circ$ ,  $\alpha_{bo} = 30^\circ$ ) through utilization of the presented characterization methodology. It was also shown that the achieved superhydrophobic effect of the ZnO layers with a standard hydrophobic top layer was stable over several years if not exposed to mechanical stress.

The application of the measurement and analysis methodology to  $Al_2O_3$  sol-gel coatings and ZnO sputtered coatings clearly demonstrated that nanorough, non-hierarchical structures are suitable to realize superhydrophobicity. It was proven specifically on the lotus leaf that only the nanostructure causes the superhydrophobicity. The striking microstructure emphasized in the literature is rather responsible for the mechanical stability than for the wettability.

In addition, the methodology was shown to be applicable for assessing microstructured surfaces with respect to superhydrophobicity. Microrough aluminum surfaces clearly exceeded the  $\kappa_B$  value of 0.4 and revealed SH properties.

First systematical investigations of hydrophilic surfaces aiming at anti-fog behavior were performed to extend the roughness analysis methods to hydrophilic wetting systems and to prove the suitability of the acquired hydrophilic wetting analysis



methods. Therefore, the effect of varying process parameters (withdrawal velocity, number of dipping iterations, particle diameter, particle concentration) on the structural properties (roughness, porosity, layer thickness) and hence on the hydrophilicity was examined using nanorough SiO<sub>2</sub> sol-gel coatings.

It was demonstrated that the  $\kappa_B$  approach could be transferred to hydrophilic surfaces. Simultaneously, the utilization of this approach led to the conclusion that the wetting-relevant spatial frequency range of hydrophilic nanostructured surfaces is identical with the relevant range ( $10 \mu\text{m}^{-1} \leq f \leq 1000 \mu\text{m}^{-1}$ ) of hydrophobic nanorough surfaces. The best hydrophilicity, i.e. excellent anti-fog behavior, within the investigated samples was observed for the surface characteristics with the highest  $\kappa_B$  value (0.57). However, not only the surface roughness influenced the hydrophilicity: Increasing porosity caused decreasing apparent CA as well.

In summary, the results achieved within this thesis enabled the development of a comprehensive measurement and analysis methodology applicable to various wettings systems (e.g. nanorough or microrough, hydrophobic or hydrophilic). In contrast to the common utilization of only qualitative methods or simple quantities and definitions to solely assess the surfaces properties, the novel methodology comprises robust quantitative roughness and wetting analysis methods as well as reliable and practically relevant criteria for superhydrophobicity and anti-fog. Using this characterization methodology, systematical investigations, suitable evaluation and comparison of structural and wetting properties of different stochastically rough surfaces as well as linking the functional properties with optical quality have become possible. This thorough methodology constitutes the basis for supporting an effective fabrication of the desired wetting behavior compared to the predominant trial-and-error manufacturing processes which are usually found in the literature.

The findings of this thesis also opened up new issues which should be addressed in future studies. They mainly concern the further development of the bouncing and fogging experiments. For this purpose, additional test series using varying parameters (e.g. drop velocity, drop volume for bouncing experiment or humidity, temperature for fogging experiment) should be examined. Furthermore, observation of the drop shape behavior during the impact of the drop onto the surface with a high-speed camera could be of interest. The structural analysis methods should be extended by the parameter porosity analogously to the  $\kappa_B$  approach.

For superhydrophobicity, the contradictory effect of required surface roughness and mechanical stability should be systematically studied for a correlation between both properties. The observed results of the hydrophilic surfaces aimed at anti-fogging could be confirmed and extended by investigating additional sample series.

## Bibliography

- [1] T. Young: "An Essay on the Cohesion of Fluids", *Philosophical Transactions of the Royal Society of London* 95, 65-87 (1805).
- [2] R. N. Wenzel: "Resistance of Solid Surfaces to Wetting by Water", *Industrial & Engineering Chemistry* 28, 988-994 (1936).
- [3] A. B. D. Cassie and S. Baxter: "Wettability of porous surfaces", *Transactions of the Faraday Society* 40, 546-551 (1944).
- [4] E. Johnson Rulon and H. Dettre Robert: "Contact Angle Hysteresis. I. Study of a Idealized Rough Surface" in *Contact Angle, Wettability, and Adhesion*, R. F. Gould (American Chemical Society, 1964), 112-135.
- [5] A. Marmur: "Wetting on Hydrophobic Rough Surfaces: To Be Heterogeneous or Not To Be?", *Langmuir* 19, 8343-8348 (2003).
- [6] A. Marmur: "Solid-Surface Characterization by Wetting", *Annual Review of Materials Research* 39, 473-489 (2009).
- [7] E. Bittoun and A. Marmur: "Optimizing Super-Hydrophobic Surfaces: Criteria for Comparison of Surface Topographies", *Journal of Adhesion Science and Technology* 23, 401-411 (2009).
- [8] P. Roach, N. J. Shirtcliffe, and M. I. Newton: "Progress in superhydrophobic surface development", *Soft Matter* 4, 224-240 (2008).
- [9] X. Zhang, F. Shi, J. Niu, Y. Jiang, and Z. Wang: "Superhydrophobic surfaces: from structural control to functional application", *Journal of Materials Chemistry* 18, 621-633 (2008).
- [10] X. Liu, Y. Liang, F. Zhou, and W. Liu: "Extreme wettability and tunable adhesion: biomimicking beyond nature?", *Soft Matter* 8, 2070-2086 (2012).
- [11] X.-T. Zhang, O. Sato, M. Taguchi, Y. Einaga, T. Murakami, and A. Fujishima: "Self-Cleaning Particle Coating with Antireflection Properties", *Chemistry of Materials* 17, 696-700 (2005).
- [12] S. Song, L. Jing, S. Li, H. Fu, and Y. Luan: "Superhydrophilic anatase TiO<sub>2</sub> film with the micro- and nanometer-scale hierarchical surface structure", *Materials Letters* 62, 3503-3505 (2008).
- [13] J. Drelich, E. Chibowski, D. D. Meng, and K. Terpilowski: "Hydrophilic and superhydrophilic surfaces and materials", *Soft Matter* 7, 9804-9828 (2011).
- [14] M. F. Rubner: "MIT research could clear up foggy problem", *MIT Tech Talk*, 4 (2005).
- [15] F. Ç. Cebeci, Z. Wu, L. Zhai, R. E. Cohen, and M. F. Rubner: "Nanoporosity-Driven Superhydrophilicity: A Means to Create Multifunctional Antifogging Coatings", *Langmuir* 22, 2856-2862 (2006).
- [16] N. Nuraje, R. Asmatulu, R. E. Cohen, and M. F. Rubner: "Durable Antifog Films from Layer-by-Layer Molecularly Blended Hydrophilic Polysaccharides", *Langmuir* 27, 782-791 (2010).

- [17] L. Coriand, M. Mitterhuber, A. Duparré, and A. Tünnermann: "Definition of roughness structures for superhydrophobic and hydrophilic optical coatings on glass", *Appl. Opt.* 50, C257-C263 (2011).
- [18] H. K. Park, S. W. Yoon, and Y. R. Do: "Superhydrophobicity of 2D SiO<sub>2</sub> hierarchical micro/nanorod structures fabricated using a two-step micro/nanosphere lithography", *Journal of Materials Chemistry* 22, 14035-14041 (2012).
- [19] A. Tropmann, L. Tanguy, P. Koltay, R. Zengerle, and L. Riegger: "Completely Superhydrophobic PDMS Surfaces for Microfluidics", *Langmuir* 28, 8292-8295 (2012).
- [20] H. Teisala, M. Tuominen, M. Aromaa, M. Stepien, J. M. Mäkelä, J. J. Saarinen, M. Toivakka, and J. Kuusipalo: "Nanostructures Increase Water Droplet Adhesion on Hierarchically Rough Superhydrophobic Surfaces", *Langmuir* 28, 3138-3145 (2012).
- [21] M. Nosonovsky and B. Bhushan: "Green Tribology, its History, Challenges, and Perspectives" in *Green Tribology. Biomimetics, Energy Conservation and Sustainability*, M. Nosonovsky and B. Bhushan (Springer Berlin Heidelberg, 2012), 3-22.
- [22] M. Nosonovsky and B. Bhushan: "Lotus Versus Rose: Biomimetic Surface Effects" in *Green Tribology. Biomimetics, Energy Conservation and Sustainability*, M. Nosonovsky and B. Bhushan (Springer Berlin Heidelberg, 2012), 25-40.
- [23] B. Bhushan, Y. C. Jung, and K. Koch: "Self-Cleaning Efficiency of Artificial Superhydrophobic Surfaces", *Langmuir* 25, 3240-3248 (2009).
- [24] Y. He, C. Jiang, H. Yin, J. Chen, and W. Yuan: "Superhydrophobic silicon surfaces with micro-nano hierarchical structures via deep reactive ion etching and galvanic etching", *Journal of Colloid and Interface Science* 364, 219-229 (2011).
- [25] A. Duparré, J. Ferre-Borrull, S. Gliech, G. Notni, J. Steinert, and J. M. Bennett: "Surface Characterization Techniques for Determining the Root-Mean-Square Roughness and Power Spectral Densities of Optical Components", *Appl. Opt.* 41, 154-171 (2002).
- [26] A. Duparré, M. Flemming, J. Steinert, and K. Reihls: "Optical Coatings with Enhanced Roughness for Ultrahydrophobic, Low-Scatter Applications", *Appl. Opt.* 41, 3294-3298 (2002).
- [27] M. Flemming, L. Coriand, and A. Duparré: "Ultra-hydrophobicity Through Stochastic Surface Roughness", *Journal of Adhesion Science and Technology* 23, 381-400 (2009).
- [28] M. Flemming and A. Duparré: "Design and characterization of nanostructured ultrahydrophobic coatings", *Appl. Opt.* 45, 1397-1401 (2006).
- [29] D. J. Whitehouse: *Handbook of Surface Metrology* (Institute of Physics Publishing, Bristol, 1994).
- [30] J. C. Stover: *Optical scattering: measurement and analysis (2nd ed.)*, Optical and Electro-Optical Engineering Series (McGraw-Hill, Inc., New York, 1990).
- [31] L. Coriand: *Experimentelle Untersuchungen zum Benetzungsverhalten mikro- und nanostrukturierter Oberflächen*, Diplomarbeit, Friedrich-Schiller-Universität Jena (2008).

- [32] J. Ferré-Borrull, A. Duparré, and E. Quesnel: "Procedure to Characterize Microroughness of Optical Thin Films: Application to Ion-Beam-Sputtered Vacuum-Ultraviolet Coatings", *Appl. Opt.* 40, 2190-2199 (2001).
- [33] S. Schröder: *Light scattering of optical components at 193 nm and 13.5 nm*, Ph.D. thesis, Friedrich-Schiller-Universität Jena (2008).
- [34] J. M. Bennett and L. Mattsson: "Introduction to Surface Roughness and Scattering", OSA Wahington D.C. (1999).
- [35] A. Marmur: "A Guide to the Equilibrium Contact Angles Maze", *Contact Angle, Wettability and Adhesion* 6, (2009).
- [36] A. Marmur: "Hydro- hygro- oleo- omni-phobic? Terminology of wettability classification", *Soft Matter* 8, 2867-2870 (2012).
- [37] A. Marmur: "Equilibrium contact angles: theory and measurement", *Colloids and Surface A* 116, 55-61 (1996).
- [38] A. Marmur: "Soft contact: measurement and interpretation of contact angles", *Soft Matter* 2, 12-17 (2006).
- [39] A. Marmur: "From Hygrophilic to Superhydrophobic: Theoretical Conditions for Making High-Contact-Angle Surfaces from Low-Contact-Angle Materials", *Langmuir* 24, 7573-7579 (2008).
- [40] U. S. Church, H. A. Jenkinson, and J. M. Zavada: "Relationship between surface scattering and microtopographic features", *Optical Engineering* 18, 125-136 (1979).
- [41] S. Schröder: *Untersuchungen zur Kalibrierung und Messung des Streulichts optischer Komponenten bei 193 nm und 157 nm*, Diplomarbeit, Friedrich-Schiller-Universität Jena (2004).
- [42] A. Duparré: "Light scattering of thin dielectric films" in *Thin Films for Optical Coatings*, R. E. Hummel and K. H. Guenther (Boca Raton: CRC Press, 1995), 273-304.
- [43] A. Duparré: "Light Scattering techniques for the inspection of microcomponents and microstructures" in *Optical Methods for the Inspection of Microsystems*, W. Osten (Taylor & Francis, 2006), 103-119.
- [44] J. M. Elson and J. M. Bennett: "Vector Scattering Theory", *Opt. Eng.* 18, 116-124 (1979).
- [45] P. Bousquet, F. Flory, and P. Roche: "Scattering from multilayer thin films: theory and experiment", *J. Opt. Soc* 71, 1115-1123 (1981).
- [46] A. Duparré: "Scattering from Surfaces and Thin Films" in *Encyclopedia of Modern Optics*, B. Guenther and D. Steel (Elsevier, 2004), 314-321.
- [47] S. Schröder, T. Herffurth, H. Blaschke, and A. Duparré: "Angle-resolved scattering: an effective method for characterizing thin-film coatings", *Appl. Opt.* 50, C164-C171 (2011).
- [48] ISO 13696:2002: *Optics and optical instruments - Test methods for radiation scattered by optical components* (International Organization for Standardization, 2002).

- [49] W. S. Law, S. W. Lam, W. Y. Gan, J. Scott, and R. Amal: "Effect of film thickness and agglomerate size on the superwetting and fog-free characteristics of TiO<sub>2</sub> films", *Thin Solid Films* 517, 5425-5430 (2009).
- [50] W. Y. Gan, S. W. Lam, K. Chiang, R. Amal, H. Zhao, and M. P. Brungs: "Novel TiO<sub>2</sub> thin film with non-UV activated superwetting and antifogging behaviours", *Journal of Materials Chemistry* 17, 952-954 (2007).
- [51] M. Schoeler: *Optische und funktionale Eigenschaften nanoporöser Sol-Gel-Schichten*, Diplomarbeit, Friedrich-Schiller-Universität Jena (2010).
- [52] H. Frey and G. Kienel (ed.): *Dünnschicht Technologie* (VDI Verlag, Düsseldorf, 1987), 455-567.
- [53] O. Stenzel: "Klassische Behandlung der Wechselwirkung elektromagnetischer Strahlung mit Materie" in *Das Dünnschichtspektrum*, (Akademie Verlag GmbH, Berlin, 1996), 9-104.
- [54] R. Petrich and O. Stenzel: "Modeling of transmittance, reflectance and scattering of rough polycrystalline CVD diamond layers in application to the determination of optical constants", *Optical Materials* 3, 65-76 (1994).
- [55] D. E. Aspnes: "Optical properties of thin films", *Thin Solid Films* 89, 249-262 (1982).
- [56] W. Theiß: "Optical properties of porous silicon", *Surface Science Reports* 29, 91-192 (1997).
- [57] D. A. G. Bruggeman: "Berechnung verschiedener physikalischer Konstanten von heterogenen Substanzen. I. Dielektrizitätskonstanten und Leitfähigkeiten der Mischkörper aus isotropen Substanzen", *Annalen der Physik* 416, 636-664 (1935).
- [58] S. Manakasettharn, T.-H. Hsu, G. Myhre, S. Pau, J. A. Taylor, and T. Krupenkin: "Transparent and superhydrophobic Ta<sub>2</sub>O<sub>5</sub> nanostructured thin films", *Opt. Mater. Express* 2, 214-221 (2012).
- [59] Digital Instruments (ed.): "Atomic Force Microscopy, A Current Perspective", *Nanotips. The Journal for Nanoscope Users* 5, 1-5.
- [60] Digital Instruments, Veeco Metrology Group (ed.): "Scanning Probe Microscopy", *Training Notebook*, 4-21 (2000).
- [61] Bruker Corporation (ed.): "Scanning Probe Microscopy" (2011).
- [62] L. Coriand: *Charakterisierung fluoridischer Schichten für den VUV - Spektralbereich mit Hilfe der Rasterkraftmikroskopie*, Studienarbeit, Friedrich-Schiller-Universität Jena (2006).
- [63] M. Flemming, K. Roder, and A. Duparre: "Scanning force microscopy for optical surface metrology", *Proc. SPIE* 5965, 59 650A-1 - 59 650A-10 (2005).
- [64] K. Roder: *Experimentelle und modellmäßige Untersuchungen zu rastersondenmikroskopischen Methoden für die Nanometrologie*, Diplomarbeit, Westsächsische Hochschule Zwickau (FH) (2004).
- [65] P. J. d. Groot: "What is Frequency Domain Analysis", *R&D Technical Bulletin* (Zygo Corporation), 1-7 (1993).

- [66] P. J. d. Groot and L. L. Deck: "Surface profiling by frequency-domain analysis of white light interferograms", Proc. SPIE 2248, 101-104 (1994).
- [67] L. Deck and P. de Groot: "High-speed noncontact profiler based on scanning white-light interferometry", Appl. Opt. 33, 7334-7338 (1994).
- [68] R.-J. Recknagel: *Anwendung der Wavelettransformation auf die Auswertung von Weißlichtinterferogrammen und die Charakterisierung von Oberflächenrauigkeiten*, Diplomarbeit, Friedrich-Schiller-Universität Jena (1996).
- [69] ZygoLOT Europe (ed.): "NewView 7000 - Product guide for the NewView 3D Optical Profiler" (2008).
- [70] S. Wilhelm: "Confocal Laser Scanning Microscopy", 4-27 (2010).
- [71] Carl Zeiss GmbH (ed.): "Das konfokale Laser Scanning Mikroskop."
- [72] M. Flemming: *Methoden der Simulation und Charakterisierung von nanostrukturierten ultrahydrophoben Oberflächen für optische Anwendungen*, Ph.D. thesis, Technische Universität Ilmenau (2007).
- [73] A. Marmur and E. Bittoun: "When Wenzel and Cassie Are Right: Reconciling Local and Global Considerations", Langmuir 25, 1277-1281 (2009).
- [74] DataPhysics Instruments GmbH (ed.): "Betriebsanleitung OCA" (2005).
- [75] A. Duparré and L. Coriand: "Abrollen, abperlen, spreiten", Optik & Photonik 7, 37-41 (2012).
- [76] Light scattering measurements by Fraunhofer IOF Jena, Alexander von Finck.
- [77] A. Finck, M. Hauptvogel, and A. Duparré: "Instrument for close-to-process light scatter measurements of thin film coatings and substrates", Appl. Opt. 50, C321-C328 (2011).
- [78] S. Schröder, S. Gliech, and A. Duparré: "Measurement system to determine the total and angle-resolved light scattering of optical components in the deep-ultraviolet and vacuum-ultraviolet spectral regions", Appl. Opt. 44, 6093-6107 (2005).
- [79] H. Xie, J. Wei, and X. Zhang: "Characterisation of Sol-gel Thin Films by Spectroscopic Ellipsometry", Journal of Physics: Conference Series 28, 95 (2006).
- [80] O. Stenzel, S. Wilbrandt, K. Friedrich, and N. Kaiser: "Realistische Modellierung der NIR/VIS/UVoptischen Konstanten dünner optischer Schichten im Rahmen des Oszillatormodells", Vakuum in Forschung und Praxis 21, 15-23 (2009).
- [81] M. Vayer, T. H. Nguyen, D. Grosso, C. Boissiere, M. A. Hillmyer, and C. Sinturel: "Characterization of Nanoporous Polystyrene Thin Films by Environmental Ellipsometric Porosimetry", Macromolecules 44, 8892-8897 (2011).
- [82] O. Stenzel and R. Petrich: "Flexible construction of error functions and their minimization: application to the calculation of optical constants of absorbing or scattering thin-film materials from spectrophotometric data", Journal of Physics D: Applied Physics 28, 978 (1995).
- [83] O. Stenzel, S. Wilbrandt, and N. Kaiser: "Absolutmessungen von gerichteter Transmission und Reflexion an Festkörperproben in der GPOB unter Nutzung von

- VN-Einsätzen und Anwendung auf die optische Charakterisierung dünner Festkörperschichten", *Colloquium optische Spektroskopie* (2011).
- [84] M. K. Dawood, H. Zheng, N. A. Kurniawan, K. C. Leong, Y. L. Foo, R. Rajagopalan, S. A. Khan, and W. K. Choi: "Modulation of surface wettability of superhydrophobic substrates using Si nanowire arrays and capillary-force-induced nanocoherence", *Soft Matter* 8, 3549-3557 (2012).
- [85] H. P. Jennissen and S. Lüers: "Lotus-Effect and inverse Lotus-Effect in connection with extremely rough titanium surfaces. Lotus- und inverser Lotus-Effekt im Zusammenhang mit extrem rauen Titanoberflächen", *Materialwissenschaft und Werkstofftechnik* 41, 1062-1069 (2010).
- [86] R. F. Taurino, E.; Messori, M.; Pilati, F.; Pospiech, D.; Synytska, A.: "Facile preparation of superhydrophobic coatings by sol-gel processes", *Journal of Colloid and Interface Science* 325, 149-156 (2008).
- [87] Y. Li, L. Li, and J. Sun: "Bioinspired Self-Healing Superhydrophobic Coatings", *Angewandte Chemie International Edition* 49, 6129-6133 (2010).
- [88] G. Perry, Y. Coffinier, V. Thomy, and R. Boukherroub: "Sliding Droplets on Superomniphobic Zinc Oxide Nanostructures", *Langmuir* 28, 389-395 (2012).
- [89] E. L. Foster, A. C. C. De Leon, J. Mangadlao, and R. Advincula: "Electropolymerized and polymer grafted superhydrophobic, superoleophilic, and hemi-wicking coatings", *Journal of Materials Chemistry* 22, 11025-11031 (2012).
- [90] G. Palasantzas and J. T. M. de Hosson: "Wetting on rough surfaces", *Acta Materialia* 49, 3533-3538 (2001).
- [91] Y. B. Gerbig, A. R. Phani, and H. Haefke: "Influence of nanoscale topography on the hydrophobicity of fluoro-based polymer thin films", *Applied Surface Science* 242, 251-255 (2005).
- [92] X. Zhang, M. Järn, J. Peltonen, V. Pore, T. Vuorinen, E. Levänen, and T. Mäntylä: "Analysis of roughness parameters to specify superhydrophobic antireflective boehmite films made by the sol-gel process", *Journal of the European Ceramic Society* 28, 2177-2181 (2008).
- [93] H. Ogihara, J. Okagaki, and T. Saji: "Facile Fabrication of Colored Superhydrophobic Coatings by Spraying a Pigment Nanoparticle Suspension", *Langmuir* 27, 9069-9072 (2011).
- [94] R. G. Karunakaran, C.-H. Lu, Z. Zhang, and S. Yang: "Highly Transparent Superhydrophobic Surfaces from the Coassembly of Nanoparticles ( $\leq 100$  nm)", *Langmuir* 27, 4594-4602 (2011).
- [95] H. Awada, B. Grignard, C. Jérôme, A. Vaillant, J. I. De Coninck, B. Nysten, and A. M. Jonas: "Correlation between Superhydrophobicity and the Power Spectral Density of Randomly Rough Surfaces", *Langmuir* 26, 17798-17803 (2010).
- [96] C. W. Extrand: "Repellency of the Lotus Leaf: Resistance to Water Intrusion under Hydrostatic Pressure", *Langmuir* 27, 6920-6925 (2011).
- [97] T. An, S. J. Cho, W. Choi, J. H. Kim, S. T. Lim, and G. Lim: "Preparation of stable superhydrophobic mesh with a biomimetic hierarchical structure", *Soft Matter* 7, 9867-9870 (2011).

- [98] J.-J. Yuan and R.-H. Jin: "Direct Generation of Silica Nanowire-Based Thin Film on Various Substrates with Tunable Surface Nanostructure and Extreme Repellency toward Complex Liquids", *Langmuir* 27, 9588-9596 (2011).
- [99] I. Saarikoski, F. Joki-Korpela, M. Suvanto, T. T. Pakkanen, and T. A. Pakkanen: "Superhydrophobic elastomer surfaces with nanostructured micronails", *Surface Science* 606, 91-98 (2012).
- [100] Z. Cerman, A. K. Stosch, and W. Barthlott: "Der Lotus-Effekt: Selbstreinigende Oberflächen und ihre Übertragung in die Technik", *Biologie in unserer Zeit* 34, 290-296 (2004).
- [101] W. Barthlott and C. Neinhuis: "Purity of the sacred lotus, or escape from contamination in biological surfaces", *Planta* 202, 1-8 (1997).
- [102] P. Wagner, R. Furstner, W. Barthlott, and C. Neinhuis: "Quantitative assessment to the structural basis of water repellency in natural and technical surfaces", *Journal of Experimental Botany* 54, 1295-1303 (2003).
- [103] Y.-T. Cheng and D. E. Rodak: "Is the lotus leaf superhydrophobic?", *Applied Physics Letters* 86, 144101-3 (2005).
- [104] H. J. Ensikat, P. Ditsche-Kuru, C. Neinhuis, and W. Barthlott: "Superhydrophobicity in perfection: the outstanding properties of the lotus leaf", *Beilstein J. Nanotechnol.* 2, 152-161 (2011).
- [105] J. G. Fan, X. J. Tang, and Y. P. Zhao: "Water contact angles of vertically aligned Si nanorod arrays", *Nanotechnology* 15, 501 (2004).
- [106] J. Bico, U. Thiele, and D. Quere: "Wetting of textured surfaces", *Colloids Surf. A* 206, 41-46 (2002).
- [107] M. Miyauchi and H. Tokudome: "Low-reflective and super-hydrophilic properties of titanate or titania nanotube thin films via layer-by-layer assembly", *Thin Solid Films* 515, 2091-2096 (2006).
- [108] L. Zhai, M. C. Berg, F. á. Cebeci, Y. Kim, J. M. Milwid, M. F. Rubner, and R. E. Cohen: "Patterned Superhydrophobic Surfaces: Toward a Synthetic Mimic of the Namib Desert Beetle", *Nano Letters* 6, 1213-1217 (2006).
- [109] B. Cortese and H. Morgan: "Controlling the Wettability of Hierarchically Structured Thermoplastics", *Langmuir* (2011).
- [110] J. A. Howarter and J. P. Youngblood: "Self-Cleaning and Next Generation Anti-Fog Surfaces and Coatings", *Macromolecular Rapid Communications* 29, 455-466 (2008).
- [111] D. Duvivier, D. Seveno, R. Rioboo, T. D. Blake, and J. De Coninck: "Experimental Evidence of the Role of Viscosity in the Molecular Kinetic Theory of Dynamic Wetting", *Langmuir* 27, 13015-13021 (2011).
- [112] M. Nie, P. Patel, K. Sun, and D. D. Meng: "Superhydrophilic anti-fog polyester film by oxygen plasma treatment", *Proc. IEEE Computer Society*, 1017-1020 (2009).
- [113] P. Patel, C. K. Choi, and D. D. Meng: "Superhydrophilic Surfaces for Antifogging and Antifouling Microfluidic Devices", *Journal of the Association for Laboratory Automation* 15, 114-119 (2010).



- [114] Sample preparation, hydrophobic functionalization by ETC PRODUCTS GmbH, Dr. M. Mitterhuber.
- [115] T. Günther: *Zum Fällungsprozess und Wachstum kugelförmiger SiO<sub>2</sub>-Partikel*, Ph.D. thesis, Otto-von-Guericke-Universität Magdeburg (2008).
- [116] C. J. Brinker, G. C. Frye, A. J. Hurd, and C. S. Ashley: "Fundamentals of sol-gel dip coating", *Thin Solid Films* 201, 97-108 (1991).
- [117] R. Carl: "Sol-Gel und Dip-Coating", Anleitung und Seminar zum Materialkundlichen Praktikum (Glaschemie - FSU Jena) (2006).
- [118] J. T. Gudmundsson, N. Brenning, D. Lundin, and U. Helmersson: "High power impulse magnetron sputtering discharge", *J. Vac. Sci. Technol. A* 30, 030801-1 - 35 (2012).
- [119] Sample preparation by Fraunhofer IST, Oliver Werner.
- [120] W. Brandl and H.-D. Steffens: *Moderne Beschichtungsverfahren* (Informationsgesellschaft Verlag, Dortmund, 1992).
- [121] M. Vergöhl, O. Werner, and S. Bruns: "New developments in magnetron sputter processes for precision optics", *SPIE* 7101, 71010B-17 (2008).
- [122] O. Werner: personal correspondence. Fraunhofer IST (2009).
- [123] G. Bräuer, J. Szczyrbowski, and G. Teschner: "Mid frequency sputtering - a novel tool for large area coating", *Surface and Coatings Technology* 94-95, 658-662 (1997).
- [124] R. Bandorf, M. Vergöhl, O. Werner, V. Sittinger, and G. Bräuer: "HiPIMS - Technologie und Anwendungsfelder", *Vakuum in Forschung und Praxis* 21, 32-38 (2009).
- [125] L.-J. Meng and M. P. d. Santos: "Characterization of ZnO films prepared by dc reactive magnetron sputtering at different oxygen partial pressures", *Vacuum* 46, 1001-1004 (1995).
- [126] Samples provided by University UFRGS Brazil, Dr. K. C. Camargo.
- [127] D. E. Weibel, A. F. Michels, A. F. Feil, L. v. Amaral, S. r. R. Teixeira, and F. v. Horowitz: "Adjustable Hydrophobicity of Al Substrates by Chemical Surface Functionalization of Nano/Microstructures", *The Journal of Physical Chemistry C* 114, 13219-13225 (2010).
- [128] K. Schwirn: *Harte Anodisation von Aluminium mit verdünnter Schwefelsäure*, Ph.D. thesis, Martin-Luther-Universität Halle-Wittenberg (2008).
- [129] Dr. K. C. Camargo: personal correspondence. University UFRGS Brazil (2012).
- [130] T. Nishino, M. Meguro, K. Nakamae, M. Matsushita, and Y. Ueda: "The Lowest Surface Free Energy Based on - CF<sub>3</sub> Alignment", *Langmuir* 15, 4321-4323 (1999).
- [131] Merck KGaA (ed.): "The TOP coat - Water, oil, and dirt won't stick to coatings made with substances WR Patinal - but you will!" (2009).
- [132] Polytec PT (ed.): "Oberflächenvorbehandlung. Oberflächensilikatisierung" (2010).

- [133] SURA Instruments GmbH (ed.): "The Pyrosil - Technique: Technology for improvement of adhesive strength of surfaces" (2004).
- [134] M. Miwa, A. Nakajima, A. Fujishima, K. Hashimoto, and T. Watanabe: "Effects of the Surface Roughness on Sliding Angles of Water Droplets on Superhydrophobic Surfaces", *Langmuir* 16, 5754-5760 (2000).
- [135] R. Blossey: "Self-cleaning surfaces - virtual realities", *Nat Mater* 2, 301-306 (2003).
- [136] A. Marmur: "The Lotus Effect: Superhydrophobicity and Metastability", *Langmuir* 20, 3517-3519 (2004).
- [137] J. Kijlstra, K. Reihls, and A. Klamt: "Roughness and topology of ultra-hydrophobic surfaces", *Colloids and Surfaces A: Physicochemical and Engineering Aspects* 206, 521-529 (2002).
- [138] B. Sobac and D. Brutin: "Triple-Line Behavior and Wettability Controlled by Nanocoated Substrates: Influence on Sessile Drop Evaporation", *Langmuir* 27, 14999-15007 (2011).
- [139] X. Deng, L. Mammen, H.-J. Butt, and D. Vollmer: "Candle Soot as a Template for a Transparent Robust Superamphiphobic Coating", *Science* 335, 67-70 (2012).
- [140] L. Wang, J. Wei, and Z. Su: "Fabrication of Surfaces with Extremely High Contact Angle Hysteresis from Polyelectrolyte Multilayer", *Langmuir* 27, 15299-15304 (2011).
- [141] Z. He, M. Ma, X. Lan, F. Chen, K. Wang, H. Deng, Q. Zhang, and Q. Fu: "Fabrication of a transparent superamphiphobic coating with improved stability", *Soft Matter* 7, 6435-6443 (2011).
- [142] H. Ogihara, J. Xie, J. Okagaki, and T. Saji: "Simple Method for Preparing Superhydrophobic Paper: Spray-Deposited Hydrophobic Silica Nanoparticle Coatings Exhibit High Water-Repellency and Transparency", *Langmuir* 28, 4605-4608 (2012).
- [143] I. S. Bayer, D. Fragouli, P. J. Martorana, L. Martiradonna, R. Cingolani, and A. Athanassiou: "Solvent resistant superhydrophobic films from self-emulsifying carnauba wax-alcohol emulsions", *Soft Matter* 7, 7939-7943 (2011).
- [144] A. F. Feil, D. E. Weibel, R. R. Corsetti, M. D. Pierozan, A. F. Michels, F. Horowitz, L. v. Amaral, and S. r. R. Teixeira: "Micro and Nano-Texturization of Intermetallic Oxide Alloys by a Single Anodization Step: Preparation of Artificial Self-Cleaning Surfaces", *ACS Applied Materials & Interfaces* 3, 3981-3987 (2011).
- [145] K.-C. Park, H. J. Choi, C.-H. Chang, R. E. Cohen, G. H. McKinley, and G. Barbastathis: "Nanotextured Silica Surfaces with Robust Superhydrophobicity and Omnidirectional Broadband Supertransmissivity", *ACS Nano* 6, 3789-3799 (2012).
- [146] W. Chen, A. Y. Fadeev, M. C. Hsieh, D. Öner, J. Youngblood, and T. J. McCarthy: "Ultrahydrophobic and Ultralyophobic Surfaces: Some Comments and Examples", *Langmuir* 15, 3395-3399 (1999).
- [147] D. Quéré: "Non-sticking drops", *Reports on Progress in Physics* 68, 2495 (2005).
- [148] C. Neinhuis and W. Barthlott: "Characterization and Distribution of Water-repellent, Self-cleaning Plant Surfaces", *Annals of Botany* 79, 667-677 (1997).

- [149] K. Koch, B. Bhushan, and W. Barthlott: "Diversity of structure, morphology and wetting of plant surfaces", *Soft Matter* 4, 1943-1963 (2008).
- [150] L. Coriand, E. Forwerk, and A. Duparré: "Applied wetting analysis of hydrophobic surfaces", Annual Report - Fraunhofer IOF 42-45 (2011).
- [151] E. Wolfram and R. Faust: "Liquid drops on a tilted plate, contact angle hysteresis and the young contact angle" in *Wetting, Spreading and Adhesion*, (Academic Press, J. F. Padday, London, 1978), 213-222.
- [152] J. Li, X. Liu, Y. Ye, H. Zhou, and J. Chen: "Fabrication of Superhydrophobic CuO Surfaces with Tunable Water Adhesion", *The Journal of Physical Chemistry C* 115, 4726-4729 (2011).
- [153] Y. Zhang, Y. Chen, L. Shi, J. Li, and Z. Guo: "Recent progress of double-structural and functional materials with special wettability", *Journal of Materials Chemistry* 22, 799-815 (2012).
- [154] Z. Wang, C. Lopez, A. Hirska, and N. Koratkar: "Impact dynamics and rebound of water droplets on superhydrophobic carbon nanotube arrays", *Applied Physics Letters* 91, 023105-3 (2007).
- [155] L. Feng, Y. Zhang, J. Xi, Y. Zhu, N. Wang, F. Xia, and L. Jiang: "Petal Effect: A Superhydrophobic State with High Adhesive Force", *Langmuir* 24, 4114-4119 (2008).
- [156] D. Bartolo, F. Bouamrène, V. É, A. Buguin, P. Silberzan, and S. Moulinet: "Bouncing or sticky droplets: Impalement transitions on superhydrophobic micropatterned surfaces", *EPL (Europhysics Letters)* 74, 299 (2006).
- [157] T. Mao, D. C. S. Kuhn, and H. Tran: "Spread and rebound of liquid droplets upon impact on flat surfaces", *AIChE Journal* 43, 2169-2179 (1997).
- [158] Š. Šikalo, M. Marengo, C. Tropea, and E. N. Ganić: "Analysis of impact of droplets on horizontal surfaces", *Experimental Thermal and Fluid Science* 25, 503-510 (2002).
- [159] R. Crooks, J. Cooper-White, and D. V. Boger: "The role of dynamic surface tension and elasticity on the dynamics of drop impact", *Chemical Engineering Science* 56, 5575-5592 (2001).
- [160] R. Rioboo, M. Marengo, and C. Tropea: "Time evolution of liquid drop impact onto solid, dry surfaces", *Experiments in Fluids* 33, 112-124 (2002).
- [161] C. Rothhardt: *Experimentelle Untersuchungen zur Nanotopografie und Benetzung hydrophober Schichten auf Glas*, Diplomarbeit, Friedrich-Schiller-Universität Jena (2010).
- [162] T. H. Margrain and C. Owen: "The misting characteristics of spectacle lenses", *Ophthalmic and Physiological Optics* 16, 108-114 (1996).
- [163] B. J. Briscoe and K. P. Galvin: "The effect of surface fog on the transmittance of light", *Solar Energy* 46, 191-197 (1991).
- [164] G. Grosu, L. Andrzejewski, G. Veilleux, and G. G. Ross: "Relation between the size of fog droplets and their contact angles with CR39 surfaces", *Journal of Physics D: Applied Physics* 37, 3350 (2004).

- [165] D. Quéré: "Rough ideas on wetting", *Physica A: Statistical Mechanics and its Applications* 313, 32-46 (2002).
- [166] Y. Konosu, H. Matsumoto, K. Tsuboi, M. Minagawa, and A. Tanioka: "Enhancing the Effect of the Nanofiber Network Structure on Thermoresponsive Wettability Switching", *Langmuir* 27, 14716-14720 (2011).
- [167] B. S. Kim, S. Shin, S. J. Shin, K. M. Kim, and H. H. Cho: "Control of Superhydrophilicity/Superhydrophobicity using Silicon Nanowires via Electroless Etching Method and Fluorine Carbon Coatings", *Langmuir* 27, 10148-10156 (2011).
- [168] M. J. de Ruijter, J. De Coninck, T. D. Blake, A. Clarke, and A. Rankin: "Contact Angle Relaxation during the Spreading of Partially Wetting Drops", *Langmuir* 13, 7293-7298 (1997).
- [169] T. D. Blake, A. Clarke, J. De Coninck, and M. J. de Ruijter: "Contact Angle Relaxation during Droplet Spreading: Comparison between Molecular Kinetic Theory and Molecular Dynamics", *Langmuir* 13, 2164-2166 (1997).
- [170] M. Bahr, F. Tiberg, and V. Yaminsky: "Spreading dynamics of liquids and surfactant solutions on partially wettable hydrophobic substrates", *Colloids and Surfaces A* 193, 85-96 (2001).
- [171] L. H. Tanner: "The spreading of silicone oil drops on horizontal surfaces", *J. Phys. D: Appl. Phys* 12, 1473-1484 (1979).
- [172] DataPhysics Instruments GmbH (ed.): "Kontaktwinkelbestimmung durch verschiedene Methoden der Konturauswertung" (2010).
- [173] E. Forwerk: *Untersuchung des Einflusses der Oberflächenstruktur auf das Benetzungsverhalten technischer Oberflächen*, Diplomarbeit, Friedrich-Schiller-Universität Jena (2011).
- [174] S. J. Dain, A. K. Hoskin, C. Winder, and D. P. Dingsdag: "Assessment of fogging resistance of anti-fog personal eye protection", *Ophthalmic and Physiological Optics* 19, 357-361 (1999).
- [175] A. Duparré and L. Coriand: "Schlussbericht - Verbundvorhaben KRONOS: Kratz- und schmutzresistente geformte Glasoberflächen durch steuerbar nano-strukturierte Sputterschichten", Final report of the BMBF joint project KRONOS (2011).
- [176] Y. Nonomura, S. Chida, E. Seino, and H. Mayama: "Anomalous Spreading with Marangoni Flow on Agar Gel Surfaces", *Langmuir* 28, 3799-3806 (2012).

## Danksagung

Hier möchte ich all denen danken, die zur Entstehung dieser Arbeit beigetragen haben:

Mein besonderer Dank gilt meinem betreuenden Hochschullehrer Herrn Prof. Dr. Andreas Tünnermann für die wertvolle fachliche Unterstützung während der Promotionszeit. Seine Hinweise und aufschlussreichen Diskussionen in wohlthuend konstruktiver Atmosphäre waren wesentliche Voraussetzung für das Zustandekommen dieser Arbeit.

Sehr herzlich danke ich Frau Dr. Angela Duparré (Fraunhofer-Institut für Angewandte Optik und Feinmechanik (IOF), Jena). Sie hat mich von der ersten Konzeption, über die Durchführung bis hin zur Realisierung der Arbeit immer umfassend begleitet. Ihre fachliche Kompetenz, stete Bereitschaft zur Fachdiskussion sowie ihre richtungsweisenden Ratschläge trugen maßgeblich zum Gelingen der Arbeit bei.

Ebenso möchte ich mich bei Dr. Marcel Flemming bedanken, weil er mich im Vorfeld der Arbeit an die Problematik der Charakterisierung funktionaler Oberflächen herangeführt und damit bereits während der Studienzeit mein Interesse am Thema geweckt hat.

Christian Wiede (IOF), Carolin Rothhardt (IOF) sowie Markus Schoeler sei für ihre Unterstützung bei der Durchführung einer Vielzahl von Messungen gedankt.

Weiterhin danke ich den Mitarbeitern am Fraunhofer IOF sowie der gesamten Abteilung „Optische Systeme“ unter Leitung von Dr. Gunther Notni für das angenehme Arbeitsklima - insbesondere Dr. Sven Schröder, Marcus Trost und Matthias Hauptvogel (IOF), die gerade in der Endphase bei der Erstellung der Dissertation wichtige Gesprächspartner waren, und Alexander von Finck für die Streulichtuntersuchungen und Diskussionen.

Bedanken möchte ich mich auch bei denjenigen, die durch die Herstellung und Bereitstellung von Proben sowie dem damit verbundenen fruchtbaren Erkenntnisaustausch die vorgestellten Untersuchungen und deren Ergebnisse erst ermöglicht haben: Dr. Monika Mitterhuber und Simone Vogl (ETC PRODUCTS GmbH, Deckendorf) kümmerten sich um die Darstellung von oxidischen Sol-Gel-Schichten. Oliver Werner (Fraunhofer-Institut für Schicht- und Oberflächentechnik, Braunschweig) stellte oxidische Sputterschichten her. Dr. Kelly Cristine Camargo (Universität UFRGS, Brasilien) stellte strukturierte Aluminiumsubstrate zur Verfügung.

Dem Bundesministerium für Bildung und Forschung sowie der Bayerischen Forschungsstiftung danke ich für die finanzielle Unterstützung durch Förderprojekte in den vergangenen Jahren.

Bedanken möchte ich mich auch bei Kiira Radzuweit für Ihre hilfreichen Hinweise in der letzten Phase des Korrekturlesens.

Schließlich bleibt mir noch, mich bei meiner verständnisvollen Familie zu bedanken. Ganz besonders dankbar bin ich meinem Mann Steffen, der mir von Beginn an den nötigen Rückhalt gab und mir hilfreich zur Seite stand, sowie meiner wundervollen Tochter Johanna, die mich auf ihre Weise motivierte.

## Kurzfassung

Funktionale Oberflächen mit einstellbaren Benetzungseigenschaften sind von enormem Interesse für hochwertige optische Komponenten sowie für Massenprodukte mit ästhetischen Anforderungen (z.B. easy-to-clean Brillengläser, Fenster- und Schmuckglas oder beschlagfreie Visiere und Badezimmerspiegel).

Gegenstand der vorliegenden Arbeit war die Entwicklung einer Mess- und Auswertemethodologie zur komplexen Charakterisierung der Struktur-Eigenschaftsbeziehung hydrophober und hydrophiler Funktionsflächen bis hin zur Superhydrophobie und zu Anti-Beschlageffekten. Dazu wurden bestehende Verfahren der Rauheits- und Benetzungsanalyse hinsichtlich ihrer Eignung für Benetzungssysteme mit unterschiedlich stochastisch rauen Oberflächen und intrinsischen Materialeigenschaften ausgewählt, angepasst und um neu erarbeitete Methoden erweitert.

Die Beschreibung der Rauheitscharakteristik der Proben erfolgte über spektrale Leistungsdichtefunktionen (PSD). Aus diesen Funktionen wurde mittels eines bereits vorhandenen Datenreduktionsalgorithmus der Benetzungsparameter  $\kappa_B$  abgeleitet, welcher die Bewertung der Struktureignung getrennt von den intrinsischen Benetzungseigenschaften der Oberflächen ermöglicht. Mit Hilfe dieser  $\kappa_B$ -Methode konnte in der Arbeit gezeigt werden, dass für nanorauere Oberflächen der hochfrequente Ortsfrequenzbereich ( $10 \mu\text{m}^{-1} \leq f \leq 1000 \mu\text{m}^{-1}$ ) zur vollständigen Bestimmung der benetzungsrelevanten Rauheitscharakteristik ausreicht. Die Rauheitsmessungen erfolgten dabei durch Rasterkraftmikroskopie (AFM). Bei mikrostrukturierten Oberflächen war es erforderlich, die Rauheitsinformationen über einen breiteren Spektralbereich zu bestimmen. Dazu wurden die Messverfahren AFM und Weißlichtinterferometrie bzw. Laser-Scanning-Mikroskopie kombiniert.

Die Benetzungsanalyse von hydrophoben Oberflächen mit hohen Fortschreitekontaktwinkeln ( $\theta_{aca} > 140^\circ$ ), bei denen Tropfen bei Probenneigung eher haften oder bestenfalls abgleiten, wurde um Abperlexperimente erweitert. Dabei wird ein Wassertropfen ( $V = 6 \mu\text{l}$ ) aus einer Höhe von 6 mm auf eine um maximal  $40^\circ$  geneigte Oberfläche fallen gelassen und ein Abperlwinkel  $\alpha_{bo}$  definiert. Dieser ist der minimale Neigungswinkel, bei dem Tropfen von der Oberfläche rückstandslos abperlen. Bei Oberflächen mit stark ausgeprägter Hydrophilie (makroskopisch sichtbarer Kontaktwinkel  $\theta_{ap} \lesssim 20^\circ$ ) erfolgte die Beschreibung der Benetzungseigenschaften über  $\theta_{ap}$  eines Tropfens mit konstantem Volumen in Abhängigkeit von der Benetzungszeit und der anschließenden Ermittlung zweier charakteristischer Kontaktwinkel (KW):  $\theta_{ap}$ , der sich beim ersten Kontakt zwischen

Tropfen und Oberflächen einstellt, sowie ein gemittelter  $\theta_{ap}$  zwischen 10 s und 20 s. Zur Quantifizierung der Beschlageigenschaften wurde erstmalig ein neuartiges Beschlagexperiment eingeführt. Während dieses Experimentes wird die Probenoberfläche für 30 s Wasserdampf ausgesetzt und das dokumentierte Beschlagverhalten hinsichtlich der Beschlagzeit und Tröpfchenanzahl ausgewertet.

Basierend auf den vorgestellten Methoden der Benetzungsanalyse erfolgte die Einführung neuer Benetzungskriterien. Neben der strengen theoretischen Definition der Superhydrophobie (SH:  $\theta_{aca} \gtrsim 150^\circ$ , kleine KW-Hysterese, Abrollwinkel  $\alpha \lesssim 20^\circ$ ) wurden praktische Superhydrophobiekriterien (SH<sub>pr</sub>:  $\theta_{aca} \gtrsim 140^\circ$ ,  $\alpha_{bo} \leq 40^\circ$ ) erarbeitet. Als Kriterium für beschlagfreie Oberflächen eignet sich  $\theta_{ap} \lesssim 20^\circ$  in Kombination mit einer vollständigen und sofortigen Benetzung der Oberfläche mit kondensierendem Wasser.

Zur Validierung der vorgestellten Methodologie wurden die einzelnen Verfahren auf optische und technische Oberflächen mit unterschiedlichen strukturellen und chemischen Eigenschaften angewandt. Gleichzeitig erfolgte die Untersuchung der Zusammenhänge zwischen Rauheit, Benetzung und optischen Eigenschaften.

Die im Rahmen dieser Arbeit durchgeführten Rauheits- und Benetzungsanalysen an Proben mit unterschiedlichsten Rauheitscharakteristiken zeigten, dass  $\kappa_B$ -Werte von 0,3 bzw. 0,4 belastbare notwendige Kriterien für SH<sub>pr</sub> bzw. SH darstellen. Ein Beleg dafür ist, dass sich bei keiner der untersuchten Oberflächen mit  $\kappa_B$  unterhalb dieser Schwellwerte SH<sub>pr</sub> oder SH eingestellt hat. Zudem wurde bei den superhydrophoben Oberflächen, unabhängig ob SH<sub>pr</sub> oder SH, der gewünschte Selbstreinigungseffekt beobachtet.

Weiterhin ergab sich, dass Superhydrophobie kombiniert mit geringen Streuverlusten (< 0,1% in Transmission) durch nanorauere Al<sub>2</sub>O<sub>3</sub>-Sol-Gel-Schichten erreichbar ist. Im Falle von gesputterten nanorauen ZnO-Schichten konnte der Herstellungsprozess bis hin zur Realisierung von superhydrophoben Benetzungseigenschaften (Bsp. für SH<sub>pr</sub>:  $\theta_{aca} = 149^\circ$ ,  $\alpha_{bo} = 30^\circ$ ) über die vorgestellte Methodologie essentiell unterstützt werden.

Die Untersuchungen an Al<sub>2</sub>O<sub>3</sub>- und ZnO-Schichten führten außerdem zu der Schlussfolgerung, dass zum Erreichen von superhydrophobem Benetzungsverhalten nanorauere, nicht hierarchische Oberflächenstrukturen geeignet sind. Insbesondere beim Lotus-Blatt wurde nachgewiesen, dass die Superhydrophobie allein durch die Nanostruktur erzeugt wird und, im Gegensatz zur in der Literatur vorherrschenden Meinung, die markante Mikrostruktur eher für die mechanische Stabilität verantwortlich ist.

Weiterhin ließ sich die  $\kappa_B$ -Methode zur Strukturbewertung bei hydrophoben nanorauen Benetzungssystemen auf hydrophobe mikrostrukturierte Oberflächen



sowie auf hydrophile Benetzungssysteme übertragen. Letzteres zeigte sich bei ersten systematischen Untersuchungen an hydrophilen SiO<sub>2</sub>-Sol-Gel-Schichten. Mittels der neu eingeführten Analysemethoden wurde der Einfluss variierender Schichtherstellungsparameter auf die strukturellen und damit auf die Benetzungseigenschaften untersucht. Das beste Benetzungsverhalten und gleichzeitig ein ausgezeichneter Anti-Beschlag-Effekt konnte für die Oberflächencharakteristik mit dem höchsten  $\kappa_B$ -Wert (0,57) beobachtet werden.

# Ehrenwörtliche Erklärung

Ich erkläre hiermit ehrenwörtlich, dass ich die vorliegende Arbeit selbständig, ohne unzulässige Hilfe Dritter und ohne Benutzung anderer als der angegebenen Hilfsmittel und Literatur angefertigt habe. Die aus anderen Quellen direkt oder indirekt übernommenen Daten und Konzepte sind unter Angabe der Quelle gekennzeichnet.

Bei der Auswahl und Auswertung folgenden Materials haben mir die nachstehend aufgeführten Personen in der jeweils beschriebenen Weise entgeltlich/unentgeltlich geholfen:

1. Dr. Monika Mitterhuber (ETC PRODUCTS GmbH, Deggendorf): Herstellung von  $\text{Al}_2\text{O}_3$ - und  $\text{SiO}_2$ -Sol-Gel-Schichten und Hydrophobisierung mit „PolyF1“
2. Oliver Werner (Fraunhofer IST, Braunschweig): Herstellung von ZnO-Sputterschichten und Hydrophobisierung mit „WR4®“
3. Dr. Kelly Cristine Camargo (Universität UFRGS, Brasilien): Bereitstellung von mikrostrukturierten Aluminiumproben
4. Alexander von Finck (Fraunhofer IOF, Jena): Streulichtmessungen
5. Markus Schoeler (Fraunhofer IOF, Jena): Porositäts- und Schichtdickenbestimmungen im Rahmen einer von mir betreuten Diplomarbeit

Weitere Personen waren an der inhaltlich-materiellen Erstellung der vorliegenden Arbeit nicht beteiligt. Insbesondere habe ich hierfür nicht die entgeltliche Hilfe von Vermittlungs- bzw. Beratungsdiensten (Promotionsberater oder andere Personen) in Anspruch genommen. Niemand hat von mir unmittelbar oder mittelbar geldwerte Leistungen für Arbeiten erhalten, die im Zusammenhang mit dem Inhalt der vorgelegten Dissertation stehen.

Die Arbeit wurde bisher weder im In- noch im Ausland in gleicher oder ähnlicher Form einer anderen Prüfungsbehörde vorgelegt.

Die geltende Promotionsordnung der Physikalisch-Astronomischen Fakultät ist mir bekannt.

Ich versichere ehrenwörtlich, dass ich nach bestem Wissen die reine Wahrheit gesagt und nichts verschwiegen habe.

# Lebenslauf

## Persönliche Daten

<i>Vor- und Zuname</i>	Luisa Coriand
<i>Geburtsdatum</i>	22.09.1984
<i>Geburtsort</i>	Jena
<i>Staatsangehörigkeit</i>	Deutsch

## Schulische und akademische Ausbildung

<i>08/1991 - 07/1995</i>	11. Staatliche Grundschule „Am Marienwäldchen“, Jena
<i>08/1995 - 07/1997</i>	4. Staatliches Gymnasium „Caroline Schlegel“, Jena
<i>08/1997 - 07/2003</i>	Carl Zeiss Gymnasium mit math.-naturwiss.-technischen Spezialklassen, Jena Abschluss: Abitur
<i>10/2003 - 10/2008</i>	Studium an der Friedrich-Schiller-Universität Jena Abschluss: Diplom - Ingenieur
<i>seit 12/2008</i>	Doktorandin am Institut für Angewandte Physik an der Friedrich-Schiller-Universität Jena / Fraunhofer IOF Jena

## Berufliche Tätigkeit

<i>11/2003 - 08/2007</i>	Studentische Hilfskraft am Fraunhofer IOF, Jena
<i>09/2007 - 08/2008</i>	Diplomandin am Fraunhofer IOF, Jena Diplomthema: „Experimentelle Untersuchungen zum Benetzungsverhalten mikro- und nanostrukturierter Oberflächen“
<i>09/2008 - 11/2008</i>	Wissenschaftliche Hilfskraft am Fraunhofer IOF, Jena
<i>seit 12/2008</i>	Doktorandin am Institut für Angewandte Physik an der Friedrich-Schiller-Universität Jena / Fraunhofer IOF, Jena

